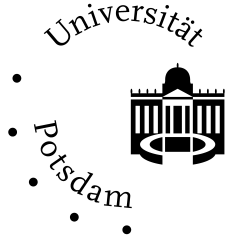

Internal variability of a coupled Arctic regional climate model

Bachelorarbeit im Fach Physik
Institut für Physik und Astronomie, Universität Potsdam

Julius Eberhard
⋆ 25.10.1991, Dresden
Matr.-Nr. 766966
jeberhar@uni-potsdam.de

1. Gutachterin: Dr. Annette Rinke
2. Gutachter: Prof. Dr. Markus Rex

Oktober 2018

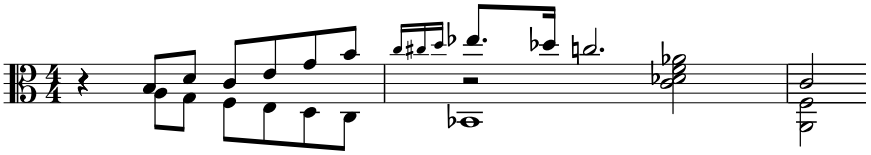

from Chick Corea: Quartet No. 2—Pt. I (Three Quartets, 1981)

Abstract

As high-dimensional nonlinear systems, regional climate models are sensitive to small perturbations of their initial state. This permits such a model, starting from almost identical states, to develop different dynamics which are equally valid solutions under the same given boundary conditions. The range of solutions generated by this internal variability (IV) is examined for the coupled Arctic regional climate model HIRHAM–NAOSIM using three ensembles. Analyzing the variables mean sea level pressure, sea ice extent, and sea ice thickness, annual cycles of IV are found. While boundary conditions significantly affect the interannual dynamics, the choice of the model version has a larger influence on the annual cycle and the magnitude of IV. Considerations of selected cases imply that links of particular IV states to spatial characteristics of the physical fields are detectable sometime but mostly inconsistent. Similarly, effects of the recent atmospheric circulation on IV states of the sea ice variables are diverse and often only weak. An assessment of the relative importance of IV compared with the overall variability shows that the IV is generally dominated by the external forcing but, depending on the season and region, occasionally exceeds the externally forced variability.

Kurzfassung

Als hochdimensionale nichtlineare Systeme reagieren regionale Klimamodelle sensibel auf kleine Störungen ihres Anfangszustands. Daher können sie, ausgehend von fast identischen Zuständen, unterschiedliche dynamische Besonderheiten als gültige Lösungen unter vorgegebenen Randbedingungen entwickeln. Diese interne Variabilität (IV) wird für das gekoppelte arktische regionale Klimamodell HIRHAM–NAOSIM mithilfe dreier Ensembles untersucht. Analysen von drei Variablen zeigen jährliche Zyklen der IV. Während Randbedingungen die interannuelle Dynamik deutlich beeinflussen, hat die Wahl der Modellversion größeren Einfluss auf den Jahresgang und die Stärke der IV. Verknüpfungen bestimmter IV-Zustände mit räumlichen Besonderheiten der physikalischen Felder werden vereinzelt gefunden, sind im Wesentlichen aber uneinheitlich. Ebenso vielfältig und oft schwach ist die Beeinflussung der IV des Meereises durch die unmittelbar vorangegangene atmosphärische Zirkulation. Eine Abschätzung des relativen Einflusses von IV gegenüber der Gesamtvariabilität zeigt eine generelle Dominanz des externen Forcings. Dennoch kann die IV die extern generierte Variabilität je nach Jahreszeit und Region gelegentlich überschreiten.

Contents

List of Figures

List of Tables

Acronyms and Symbols

$\langle\cdot\rangle$, $\langle\cdot\rangle_t$, $\langle\cdot\rangle_{x,y}$	ensemble mean, time mean, domain mean
$\mathrm{AC}^{i,j}$	anomaly ("pattern") correlation of members i and j
BC	boundary condition
i, j	indices of ensemble members
IC	initial condition
IV	internal variability
MEV	mean external variability
MLTF	mean locking time fraction
MSLP	mean sea level pressure
RCM	regional climate model
SD^*	ensemble standard deviation
$\mathrm{SD}^*_{\mathrm{rms}}$	root–mean–square ensemble standard deviation
SDR	standard deviation ratio
SIC	sea ice concentration
SIE	sea ice extent
SIT	sea ice thickness
t	index of time step
x, y	indices of horizontal grid points

1 INTRODUCTION

Computer models are indispensable tools for climate research. Every simulation by means of such a model can be seen as a simplified climate system representation which is considered acceptable within certain limits. These limits depend on the purpose of the model and are identified with uncertainty, which comprises unknowns of the climate system, errors in the system description, and intrinsic non-predictability (Foley, 2010).

One widely used modeling approach involves numerical integration of the discretized governing differential equations, as done globally by coupled general circulation models (GCMs) and for limited areas of the globe by dynamical regional climate models (RCMs). The latter offer a higher resolution and have been used for almost three decades now (Rummukainen, 2010). In contrast to their global counterparts, RCMs require conditions prescribed along the lateral and lower boundary, which affect the intrinsic uncertainty in the following sense. Limited area models can develop significant errors in response to a practically arbitrarily small perturbation of the system's initial state while the boundary conditions (BCs) remain unchanged. As a result of nonlinear terms in the model equations, this sensitivity to initial conditions (ICs) is unavoidable and therefore leads to an internally generated range of results, called internal, intrinsic, or inter-member variability (IV). The same mechanism is present in GCMs, where different initializations may alter the model results throughout a consistently forced simulation period and can be identified with long-term variability in time series. In comparison, IV of RCMs is bounded by the BCs' determining of model solutions through the transfer of dominant information from the boundary to the interior of the model domain (Anthes, 1986).

Following investigations of the predictability of limited area models (e. g. Anthes et al., 1985), the nature of IV in RCMs has been the specific subject of numerous publications in the last 18 years. In summary, IV was found to have different magnitudes in different regions (Rinke and Dethloff, 2000; Giorgi and Bi, 2000); to be essentially independent of the magnitude and source of the initial perturbation (Giorgi and Bi, 2000; Rinke et al., 2004; Lucas-Picher et al., 2008); to show different spatial distributions dependent on the model choice (Christensen et al., 2001); to be higher in larger model domains (Rinke

and Dethloff, 2000; Alexandru et al., 2007; Rapaić et al., 2010); to react to seasonal BC differences (Giorgi and Bi, 2000; Rinke et al., 2004; Caya and Biner, 2004; Alexandru et al., 2007; Dorn et al., 2012); and to vary with different parameterization schemes (Crétat and Pohl, 2012). An effect of IV on long-term statistics has been both confirmed for some variables (Lucas-Picher et al., 2008) and rejected for others (Giorgi and Bi, 2000; Caya and Biner, 2004). Comparing the magnitude of IV to variability induced by the BCs, it has been found that for certain variables in some subareas of RCM domains both can be similar and that a physical model response to an input signal can hence be masked by IV (Rinke and Dethloff, 2000; Christensen et al., 2001; Caya and Biner, 2004; Döscher et al., 2010; O'Brien et al., 2011). The methodology used in all these studies is performing a number of model runs with differing ICs, so-called ensembles. Computing pairwise differences or ensemble spreads gives then a measure of IV. Less emphasis has been attached so far to the influence of the ensemble size on the IV estimation, which can be less robust for small ensembles (Alexandru et al., 2007). One further step was taken by investigating energy conversions that contribute to IV (Diaconescu et al., 2012; Nikiéma and Laprise, 2013; Sommerfeld, 2015).

The Arctic as a region decisive for understanding the global climate (IPCC, 2013) has been characterized as less predictable than other regions (Rinke and Dethloff, 2000) and as involving strong regional processes that generate IV (Döscher et al., 2010; Dorn et al., 2012). In the present work, various aspects concerning the IV of the coupled Arctic RCM HIRHAM–NAOSIM are investigated exemplarily for the variables mean sea level pressure, sea ice extent, and sea ice thickness. Five questions are pursued during the analysis of each variable: How can IV be measured appropriately? How does the ensemble size affect the estimated IV? What temporal structure of IV can be found? Which spatial structures or patterns of the variable correspond to high or low IV? What can be said about the ratio of internal to externally generated variability? Additionally for the sea ice variables, we look at the MSLP fields preceding particular IV cases. All results are compared between three ensembles generated from two different BC data sets and two different model versions of HIRHAM–NAOSIM, which differ in their resolution and partly in their physics and parameterizations. It is therefore possible to distinguish between IV characteristics due to the boundary forcing and those due to the model choice. The common 30-year period 1979–2008 is covered by all these ensembles and receives most attention during the analysis. The work is divided into an overview of the Arctic climatology (Chapter 2), an introduction to the model versions and ensembles (Chapter 3), a discussion of the used statistical methods (Chapter 4), the presentation of results including discussions (Chapter 5), and a summary and conclusion (Chapter 6).

2 CLIMATOLOGY OF THE ARCTIC

2.1 Overview

The Arctic is the northernmost region of the earth. Definitions differ in the position of the southern boundary, identifying it, e. g., with the Arctic Circle, currently at 66°33' N, or the southernmost line where mean surface temperatures do not exceed 10 °C in July. The climate, i. e. multidecadal statistics of weather, of the Arctic is mainly influenced by the Arctic Ocean and its marginal seas, mostly bounded by the Arctic lands following southward (Figure 2.1). While the ocean surface is at least partly covered with annually growing and melting sea ice, therefore strongly fluctuating in exchanging heat, water, aerosols, and momentum between the ocean and the atmosphere and affecting the radiation balance, the land surface plays a role through intense cooling in winter and warming in summer. Some characteristics of the Arctic climatology are the almost ubiquitous snow cover present for at least six months in the year; large intra-annual differences in the surface air temperature associated with strong winterly atmospheric inversions; low air humidity; and annual cycles of precipitation with summer maxima and winter minima over the central Arctic Ocean and the Arctic lands, vice versa over the Atlantic part. The reader is referred to the book of Serreze and Barry (2005) as a comprehensive reference unless other citations are given.

2.2 Mean sea level pressure and atmospheric circulation

Air pressure is a key variable for understanding atmospheric phenomena because it relates to both mechanical and thermodynamical processes. The mean sea level pressure (MSLP), defined as air pressure at the actual or hypothetical mean sea level at, below, or above a certain location on the earth's surface, is derived from surface pressure data. It allows for the detection of horizontal differences manifesting as relative low- and high-pressure areas.

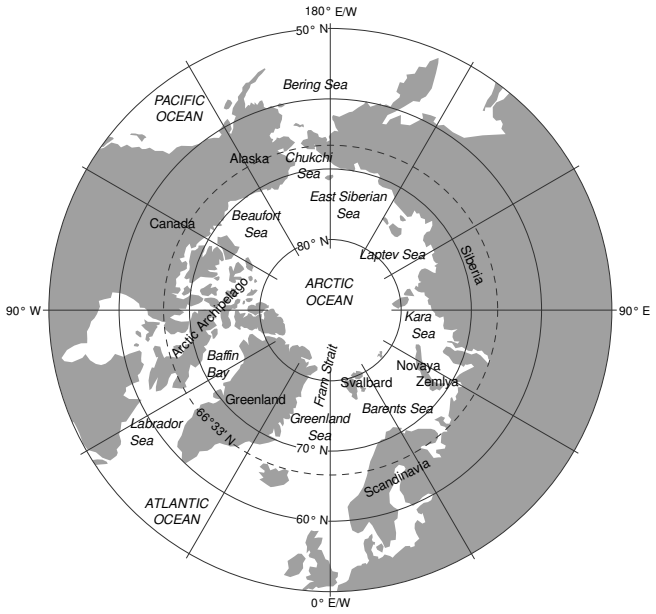

Figure 2.1: Overview map of Arctic waters and lands in equidistant azimuthal projection with the North Pole at the center.

Since the motion of an air parcel is—especially on monthly scales—mainly governed by pressure differences and deflection due to the Coriolis acceleration (e. g. Holton, 2004), the trajectories of the mean horizontal wind field approximately run along contours of constant pressure (isobars), clockwise around high-pressure areas, thereby forming anticyclones, and vice versa for low-pressure areas, forming cyclones. While anticyclones are typically rather static, Arctic cyclones can arise out of instabilities of the tropospheric zonal circulation due to temperature gradients along isobars, called baroclinic instabilities (Holton, 2004).

There exist typical seasonal patterns of MSLP over the Arctic that can be detected as mean features, i. e. climatology, regardless of the method of deriving MSLP. Figure 2.2 schematically summarizes the seasonal evolution of Arctic MSLP fields for the period 1970–1999. In January, important mean features are the low-pressure areas over Iceland and the Aleutian Islands south of the Bering Sea and a high-pressure area over Siberia. Serreze and Barry (2005) name several physical processes that may be decisive for the development of these features. For the Iceland and Aleutian Lows those are large surface temperature gradients across the sea ice boundaries, divergence of midtropospheric winds which lead to air convection off the surface, and baroclinic instability. The Siberian High is attributed to radiative cooling during winter. After a considerable weakening of the winter MSLP fields with a closed high-pressure area over the central Arctic Ocean / Beaufort Sea during spring (represented by April in the figure), summer (July) conditions are characterized by low pressures over wide parts of the Arctic. They

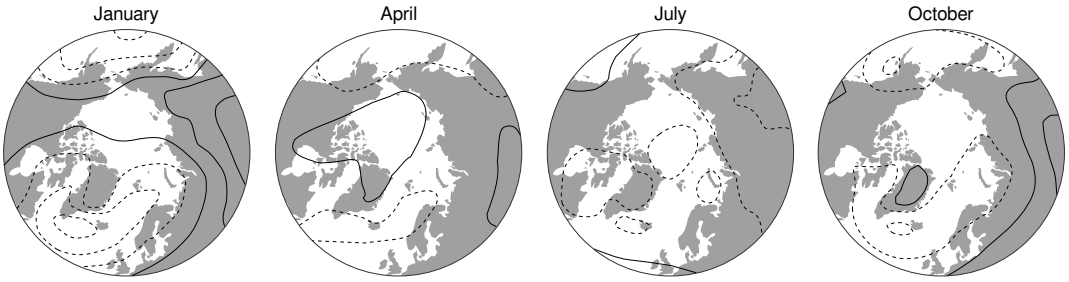

Figure 2.2: Schematics of average MSLP fields for January, April, July, and October obtained from NCEP/NCAR data of the period 1970–1999 displaying low-pressure areas (dashed contours) and high-pressure areas (solid). Contours indicate the approximate positions of isobars in 6-hPa intervals. Modified after Serreze and Barry (2005).

are at least partly consequences of thermal effects induced by the presence of solar radiation and come with increased occurrences of transient cyclones over western Siberia. In autumn (October), the winter situation starts to be restored.

In the analysis of the long-term behavior of MSLP fields, the dimensionality of data sets can be reduced by linear principal component analysis. The results are empirical orthogonal functions (EOFs), spatial patterns which can—in the order of their ability to account for the observed variations—contain information on the substantial modes in which variability in the atmospheric circulation happens. For the Arctic, these modes are the North Atlantic Oscillation, the Arctic Oscillation (AO), and the Dipole Anomaly (DA). Mainly the AO and the DA are considered to contribute to the variations in sea ice movement, with the DA probably attributed to ice melting events and consequent ice anomalies during the last decades (Wang et al., 2009).

2.3 Sea ice and ocean circulation

The Arctic Ocean receives water input from different sources. Atlantic inflow from the Greenland and Barents Seas is comparably warm and saline and forms the main lower body of the Arctic Ocean. On the other hand, fresher Pacific inflow from Bering Sea, together with river discharge and precipitation, creates an upper layer. This stratification is found to be very stable due to the difference in salinity and thus density, preventing vertical mixing over large depths all year and allowing for rapid sea ice formation in autumn. When cooling of the ocean surface starts, ice begins to form as soon as the fresh upper layer has reached a homogeneous profile of temperature at the water freezing point. Ice growth increases the upper-layer salinity through brine rejection and

weakens the stratification. Melting in summer is accompanied by an enhancement of the stratification.

In the climatology of the last three and many more decades, the central Arctic Ocean is a zone of perennially existing sea ice. Around 10–15 % of the ice surface in this zone is occupied by firstyear ice, which has formed in the last winter, the rest is multiyear ice. The seasonal ice zone, where sea ice exists dependent on the season, extends over almost the whole Arctic Ocean and is bounded mostly by coastlines except for the Atlantic part, where the boundary roughly spans the Greenland–Svalbard–Novaya Zemlya chain and the northern Labrador Sea.

Most of the sea ice is permanently drifting, driven by shear equally arising from both wind and ocean currents. The mean annual ice circulation (not shown) exhibits a pattern of two major features. First, the Beaufort Gyre is an area of anticyclonic ice motion in the Beaufort Sea. Secondly, the Transpolar Drift Stream transports ice from the Siberian coast towards the Atlantic Ocean through Fram Strait. Comparing this pattern to mean annual atmospheric features, a high-pressure area over Beaufort Sea and strong gradients between Greenland and Greenland Sea / Bering Sea (not shown), the direct influence of wind shear becomes apparent. Features of the mean ocean surface circulation, although less investigated, allow a similar conclusion with a probably anticyclonic water circulation below the Beaufort Gyre and the Pacific waters—entering from the Bering Sea and exiting through Fram Strait—supporting the Transpolar Drift Stream (Woodgate, 2013).

The seasonal variability of sea ice motion involves a bigger Beaufort Gyre and stronger Transpolar Drift Stream during winter and a weakening of these features and a slightly cyclonic motion north of the Kara / Laptev Seas during summer. Mechanisms governing the occurrence of anomalously little ice are discussed by Serreze and Barry (2005). They include single atmospheric events that favor melting through enhanced thermodynamic effects; the property that sea ice drifts at some angle to the right relative to the geostrophic wind shear, leading to ice convergence under anticyclones and divergence under cyclones; preconditioning through thin ice resulting from special conditions in previous years; and long-term reactions to modes of MSLP variability, which may affect the age of sea ice.

The extent, horizontal and vertical, of Arctic sea ice can be characterized through the variables sea ice concentration (SIC) and sea ice thickness (SIT). The SIC is defined as the fraction of sea ice area covering a certain ocean surface area. Derived therefrom, the sea ice extent (SIE) is defined as the total ocean surface area where the SIC is greater than or equal to 15 %. Climatologies of SIC and SIE quantify the seasonal ice growing and melting already indicated. Based on 1979–2015 data, derived by the National Snow

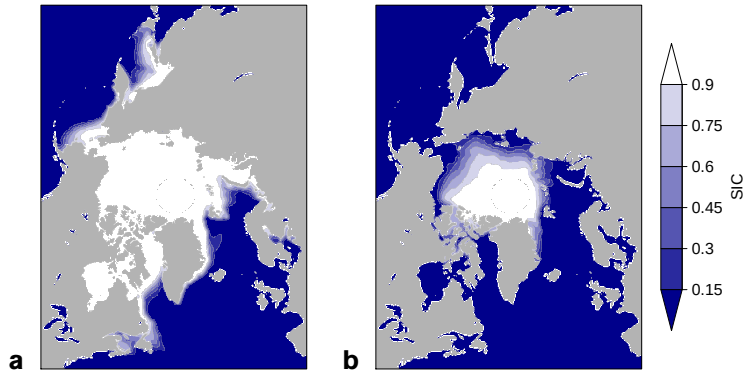

Figure 2.3: 1979–2015 mean climatology of Arctic SIC fields; **a**: March, **b**: September. Calculation was based on data supplied by the NSIDC.

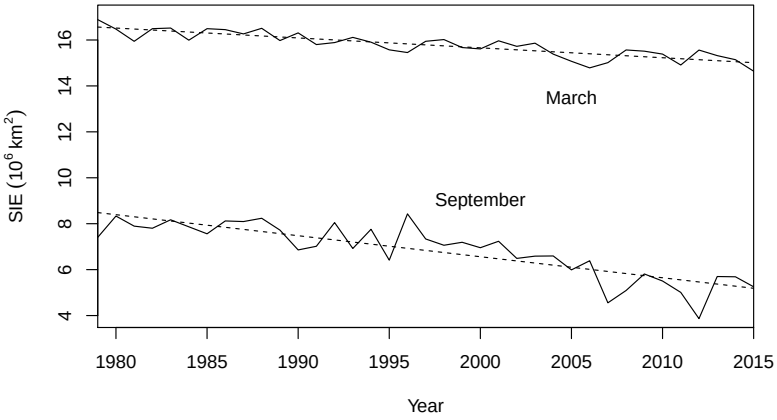

Figure 2.4: Yearly SIE of March and September, calculated from the SIC data of NSIDC, with trend lines obtained through linear regression.

and Ice Data Center (NSIDC) from satellite microwave data using a bootstrap algorithm, the maximum SIE is usually reached in March (Figure 2.3a) and takes values of 15–$17 \cdot 10^6\,\mathrm{km}^2$; the SIE is reduced to its minimum in September (Figure 2.3b) with values of 4–$8.5 \cdot 10^6\,\mathrm{km}^2$. Due to the global warming trend of the last decades, the SIE described a downward trend of about $-0.43 \cdot 10^6\,\mathrm{km}^2$ per decade in March and $-0.92 \cdot 10^6\,\mathrm{km}^2$ per decade in September (Figure 2.4). Values of SIT across the Arctic are sparsely verified but generally observed to be maximal along the coasts of Alaska, the Arctic Archipelago, and Greenland. The shear zone located there is characterized by strong ice deformation due to the movement of drifting ice against and past the fast ice fixed to the coastline. SIT is usually minimal in the Siberian and Atlantic parts of the Arctic waters.

3 MODELS AND ENSEMBLES

The present work analyzes simulation results of the coupled Arctic regional climate model (RCM) HIRHAM–NAOSIM. It contains models of the atmosphere (HIRHAM), the ocean, and the sea ice (both NAOSIM). Two versions of the coupled model have been used. The older version, as described by Dorn et al. (2007) with improved sea ice parameterizations (Dorn et al., 2009), will be referred to as HIRHAM–NAOSIM 1.2. The newer version, using better resolutions as well as changed dynamics, i. e. physical processes resolved and integrated on a numerical grid, and parameterizations, i. e. descriptions of physical processes happening on smaller scales than the model resolution, as HIRHAM–NAOSIM 2.0. HIRHAM and NAOSIM are composite models themselves and combine dynamics and parameterizations from different sources. Figure 3.1 gives a brief overview of the model components and first or comprehensive references. Note that the sea ice model is further composed of different dynamics and parameterizations and not developed as a standalone model compared to the other components.

The next sections introduce HIRHAM and NAOSIM in both versions, describe the coupling, and conclude with the design of the ensemble simulations and the data used here.

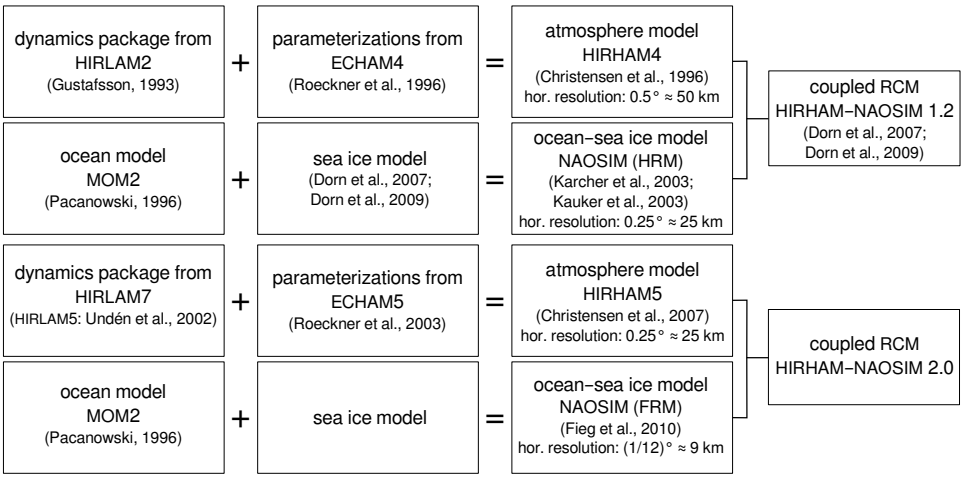

Figure 3.1: Model components consituting both versions of HIRHAM–NAOSIM.

3.1 Model components

Atmosphere model

Part of the coupled model, the standalone RCM HIRHAM is utilized to simulate the Arctic atmosphere. It was introduced in its first version by Christensen and van Meijgaard (1992) and combines the dynamical part of HIRLAM (the High Resolution Limited Area Model; first described by Källberg, 1990), which is used for short-range numerical weather prediction, and parameterization schemes of the GCM ECHAM (Hamburg version of the European Centre for Medium-Range Weather Forecasts Model; Roeckner et al., 1989).

HIRHAM is applied to a region covering the Arctic (Figure 3.2). The horizontal model grid lies on a rotated longitude–latitude grid with the 90° latitude (the model "north pole") lying at 0° N, 180° E of the usual longitude–latitude grid. In HIRHAM–NAOSIM 1.2, the horizontal resolution of HIRHAM is 0.5°, which corresponds to about 50–56 km within the model domain. The horizontal resolution used in HIRHAM–NAOSIM 2.0 is 0.25° (about 25–28 km). Vertical coordinates are specified as hybrid sigma–pressure coordinates, i. e. surface-pressure-scaled pressure coordinates (sigma coordinates) at the bottom and absolute pressure coordinates at the top. 19 unevenly spaced vertical layers in HIRHAM–NAOSIM 1.2 and 40 in HIRHAM–NAOSIM 2.0 constitute the atmosphere. The time step used for integration is 240 s in HIRHAM–NAOSIM 1.2 and 600 s in HIRHAM–NAOSIM 2.0, where the longer time step is made possible through a new semi-Lagrangian integration scheme.

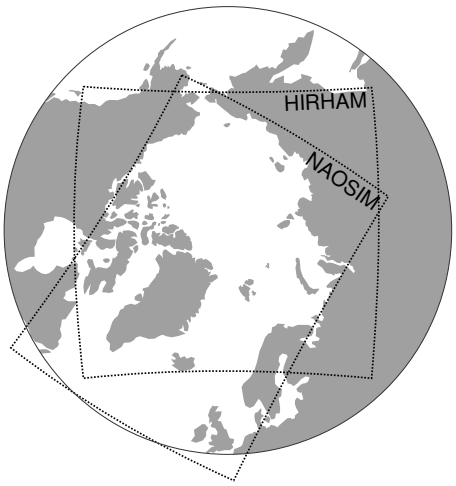

Figure 3.2: Approximate positions of the HIRHAM and NAOSIM grid boundaries (lands shown only north of 50° N).

HIRHAM solves equations for horizontal wind components, temperature, surface pressure, specific humidity, and cloud water (prognostic variables); in HIRHAM–NAOSIM 2.0, cloud ice is additionally taken into account as a prognostic variable. Parameterizations describe processes involving radiation, clouds, the planetary boundary layer, and gravity wave drag through orography. Additional land or ocean / sea ice surface effects are considered through heat balance equations. Differences in the parameterizations between the old and the new version relate, inter alia, to land surface and orographic effects, clouds, and sea ice melting.

For the assimilation of boundary conditions, a relaxation zone of 10 grid points width along the lateral boundary is included in both versions, in which internal variability is damped. The areas corresponding to the relaxation zone of the HIRHAM–NAOSIM-1.2 grid are therefore left out in the analysis of the present work where relevant.

Ocean and sea ice model

Ocean and sea ice processes are simulated with versions of NAOSIM (the North Atlantic/Arctic Ocean–Sea Ice Model), the High Resolution Model (HRM; Karcher et al., 2003; Kauker et al., 2003) and the Fine Resolution Model (FRM; Fieg et al., 2010). NAOSIM covers the central Arctic Ocean, the great majority of Arctic marginal seas, and the northern North Atlantic Ocean bounded at about 50° N (Figure 3.2). Like HIRHAM, its grid lies on a rotated spherical grid but with the model equator lying on the usual 30° W / 150° E meridian. The horizontal resolution of 0.25° (about 25–28 km) in HIRHAM–NAOSIM 1.2 has been reduced to 1/12° (around 9 km) in HIRHAM–NAOSIM 2.0. In the vertical, depth coordinates determine 30 uneven layers in HIRHAM–NAOSIM 1.2, 50 in HIRHAM–NAOSIM 2.0. Integration was carried out with a time step of 900 s in HIRHAM–NAOSIM 1.2 and 360 s in HIRHAM–NAOSIM 2.0.

Horizontal velocity components, potential temperature, and salinity are the prognostic variables of the ocean model, which is based on MOM 2 (the modular ocean model of the Geophysical Fluid Dynamics Laboratory; Pacanowski, 1996). The sea ice model consists of (i) elastic–viscous–plastic dynamics of the drifting sea ice; (ii) zero-layer thermodynamics; (iii) prognostic equations for sea ice concentration (SIC) and sea ice thickness (SIT), distinguishing thin ice / open water and thick ice conditions; and (iv) a prognostic equation for snow thickness on sea ice. Compared to HIRHAM–NAOSIM 1.2, the new version allows for sublimation of ice and features minor numerical improvements. For a comprehensive comparison between the model versions see Fieg et al. (2010).

NAOSIM features a relaxation zone of 1-grid-point width. As for the HIRHAM grids, all analyses herein involving spatial integration are conducted on the common grid area which excludes all relaxation zones.

Coupling

The coupling of HIRHAM and NAOSIM at the ocean surface requires the exchange of variables, which include fluxes of momentum, heat, and water; temperatures; sea surface salinity; and snow/ice variables. Additional coupling happens between the ocean and sea ice models. In HIRHAM–NAOSIM 1.2, the ocean–sea ice coupling is conducted at every time step, while the coupling between HIRHAM and NAOSIM occurs on an interpolated grid at every hour. HIRHAM–NAOSIM 2.0 employs the YAC software (Hanke et al., 2016) for the coupling procedure, which is carried out every hour.

3.2 Ensemble simulations and data

Possible results of a model run under slightly varied ICs are investigated using ensembles, i. e. sets of model runs ("members") starting from different initial states of the system. Statistical analysis (Chapter 4) of the ensembles can infer properties of the model's state space resulting from internal variability (IV).

Three ensembles, differing in the model architecture and the BCs, are subject to the analysis. Ensemble 1 (E1) contains six members and employs HIRHAM–NAOSIM 1.2 from 1 January 1949 to 31 December 2008 with boundary conditions taken from reanalysis data of the National Centers for Environmental Prediction (NCEP) and National Center for Atmospheric Research (NCAR) described in Kalnay et al. (1996) and referred to as NCEP data. A reanalysis is a set of climate system data spatially and temporally assimiliated to observational data of a past period by means of a single tool, usually a GCM. Ensemble 2 (E2), 10 members, uses the same model but boundary conditions from the European Centre for Medium-Range Weather Forecasts (ECMWF) reanalysis product ERA-Interim (Dee et al., 2011) for the period 1 January 1979 through 31 December 2014. Ensemble 3 (E3), also 10 members, contains results from HIRHAM–NAOSIM 2.0 with ERA-Interim boundary conditions, also for 1 January 1979 through 31 December 2014. In all ensembles, varying ICs were realized as different sea ice and ocean fields which were taken from at 1 January of different years from other model runs. For E1, these fields match those of a coupled spinup run which was initialized with the sea ice and ocean state from a standalone NAOSIM run at 25 February 1949 and run through 1 January 1960. E2 was

initialized with sea ice and ocean fields from E1. Similarly to E1, the initial conditions for sea ice and ocean of E3 were taken from January states of a coupled spinup run for 1979–2000. The initial conditions for this spinup run were obtained from a standalone 20-year NAOSIM run. See Table 3.1 for details on the ICs of all ensembles.

Boundary conditions were applied laterally throughout the model domain as well as at the lower HIRHAM domain boundary and at the upper NAOSIM boundary where both domains do not overlap at the ocean surface.

The analysis of IV is applied to monthly means of MSLP fields, SIE, and SIT fields of every ensemble.

Table 3.1: Initializations of the member runs in each ensemble.

Member	Initial ocean & sea ice state
HIRHAM–NAOSIM 1.2 with NCEP BCs (Ensemble 1)	
E1-A	1 Jan 1955 from coupled spinup run using NCEP BCs
E1-B	1 Jan 1956 from coupled spinup run using NCEP BCs
E1-C	1 Jan 1957 from coupled spinup run using NCEP BCs
E1-D	1 Jan 1958 from coupled spinup run using NCEP BCs
E1-E	1 Jan 1959 from coupled spinup run using NCEP BCs
E1-F	1 Jan 1960 from coupled spinup run using NCEP BCs
HIRHAM–NAOSIM 1.2 with ERA-Interim BCs (Ensemble 2)	
E2-A	1 Jan 1975 from E1-A
E2-B	1 Jan 1976 from E1-A
E2-C	1 Jan 1977 from E1-A
E2-D	1 Jan 1978 from E1-A
E2-E	1 Jan 1979 from E1-A
E2-F	1 Jan 1975 from E1-F
E2-G	1 Jan 1976 from E1-F
E2-H	1 Jan 1977 from E1-F
E2-I	1 Jan 1978 from E1-F
E2-J	1 Jan 1979 from E1-F
HIRHAM–NAOSIM 2.0 with ERA-Interim BCs (Ensemble 3)	
E3-A	1 Jan 1991 from coupled spinup run using ERA-Interim BCs
E3-B	1 Jan 1992 from coupled spinup run using ERA-Interim BCs
E3-C	1 Jan 1993 from coupled spinup run using ERA-Interim BCs
E3-D	1 Jan 1994 from coupled spinup run using ERA-Interim BCs
E3-E	1 Jan 1995 from coupled spinup run using ERA-Interim BCs
E3-F	1 Jan 1996 from coupled spinup run using ERA-Interim BCs
E3-G	1 Jan 1997 from coupled spinup run using ERA-Interim BCs
E3-H	1 Jan 1998 from coupled spinup run using ERA-Interim BCs
E3-I	1 Jan 1999 from coupled spinup run using ERA-Interim BCs
E3-J	1 Jan 2000 from coupled spinup run using ERA-Interim BCs

4 STATISTICAL METHODS

Internal variability (IV) as a result of nonlinear model dynamics inducing sensitivity to initial conditions (ICs) is a very general feature in physical models. Unlike some low-dimensional systems of nonlinear ordinary differential equations, which may allow for a general analysis of their time-dependent behavior and IV to some extent, climate models are complex, high-dimensional, forced systems and are thus difficult to treat universally. Instead, the most common method for investigating IV of a climate model is the ensemble method, i. e. analyzing the outputs of multiple experiments under consistent boundary conditions but slightly varied ICs. Assuming the exact differences of these varied conditions to be small enough or irrelevant to the results, one may formulate the method as a random experiment in which climate variables take values with associated probabilities. Estimating the IV of a climate model under a given distribution of ICs therefore requires to measure properties of the probability distributions underlying the random variables.

4.1 Measures of internal variability

Simple ensemble measures

Experiments in the form of model realizations of a random variable X, such as $\mathrm{MSLP}(\boldsymbol{x}, t)$ or $\mathrm{SIT}(\boldsymbol{x}, t)$ at a fixed model grid point $\boldsymbol{x} = (x, y)$ and model time t, sample discrete values X_1, $X_2, \ldots$ from a probability distribution. Any sample $\boldsymbol{X} = (X_1, X_2, \ldots, X_N)$, which is large enough to model the underlying distribution ($N \gg 1$), can be characterized by its expectation

$$\mathrm{E}\,\boldsymbol{X} = \frac{1}{N} \sum_{i=1}^{N} X_i,$$

which is a measure for the magnitude of X, and its standard deviation

$$\mathrm{SD}\,\boldsymbol{X} = \sqrt{\mathrm{E}(\boldsymbol{X} - \mathrm{E}\,\boldsymbol{X})^2} = \sqrt{\frac{1}{N}\sum_{i=1}^{N}(X_i - \mathrm{E}\,\boldsymbol{X})^2}, \tag{4.1}$$

which is a measure of the scattering magnitude around the expectation of $\boldsymbol{X}$. The standard deviation is usually preferred over other measures of scattering, e. g. $\mathrm{E}(|\boldsymbol{X} - \mathrm{E}\,\boldsymbol{X}|)$, because it allows wide application in probability theory and appears as a parameter in the normal distribution.

Ensemble climate simulations are small samples, typically with a few to some tens of members, from the hypothetical infinite population and can only provide estimations of the underlying distribution. The expectation is hence estimated by the ensemble mean

$$\langle \boldsymbol{X} \rangle = \frac{1}{N}\sum_{i=1}^{N} X_i$$

and the standard deviation by the ensemble standard deviation

$$\mathrm{SD}^*\,\boldsymbol{X} = \sqrt{\frac{1}{N-1}\sum_{i=1}^{N}(X_i - \langle \boldsymbol{X} \rangle)^2}. \tag{4.2}$$

Both estimators are preferred in statistical practice because they are unbiased, i. e.

$$\mathrm{E}\langle \boldsymbol{X} \rangle = \mathrm{E}\,\boldsymbol{X}, \quad \mathrm{E}(\mathrm{SD}^*\,\boldsymbol{X})^2 = (\mathrm{SD}\,\boldsymbol{X})^2.$$

Both (4.1) and (4.2) are convenient and commonly used for measuring the IV of all kinds of climate variables. For simplicity, henceforth samples will be identified with their variable symbol ($\boldsymbol{X} = X$) where the meaning is unambiguous.

Spatially integrated measures

IV of a RCM is a spatio–temporal phenomenon; for the analysis of its temporal evolution it is therefore useful to find measures which can condense the domain-wide variability of spatially extended variables into single values. We consider two cases of such measures for two-dimensional fields, the rms ensemble standard deviation and the anomaly correlation.

The first approach is defined as the square root of the domain mean of the squared ensemble standard deviation, hence called the root–mean–square (rms) ensemble standard deviation:

$$\mathrm{SD}^*_{\mathrm{rms}}\, X = \sqrt{\langle (\mathrm{SD}^*\, X)^2 \rangle_{x,y}}. \tag{4.3}$$

The domain mean of a field $X(x, y)$ is

$$\langle X \rangle_{x,y} = \frac{1}{A} \sum_x \sum_y X(x, y)\, A_{xy}, \tag{4.4}$$

where A_{xy} is the area of a grid cell represented by the grid point (x, y) and A is the total domain area. The rms ensemble standard deviation is comparable to the domain mean of (4.2) in its magnitude and temporal behavior. As a second-order generalized mean of the IV field, however, it weighs large local variability more heavily than small local variability. The reason for using the rms ensemble standard deviation instead of the domain-mean ensemble standard deviation is that it generalizes the rms difference commonly used to compare two time series (e. g. Rinke and Dethloff, 2000; Giorgi and Bi, 2000; Caya and Biner, 2004). Referred to as the square root of the domain-averaged variance, the rms ensemble standard deviation was also used, e. g., in the studies of Caya and Biner (2004), Alexandru et al. (2007), and Lucas-Picher et al. (2008), whereof the former two employed the biased estimator (4.1) of the standard deviation.

When analyzing intra-ensemble variability of data with a temporal resolution larger than hours or days, some variables can exhibit differences that manifest as large-scale patterns. Short-term variations of only local extent can be masked by these patterns. In this case, IV can be quantified as the anomaly correlation

$$\mathrm{AC}^{i,j} X(t) = \frac{\sum_{x,y} \left(X'_i - \langle X'_i \rangle_{x,y}\right) \left(X'_j - \langle X'_j \rangle_{x,y}\right)}{\left[\sum_{x,y} \left(X'_i - \langle X'_i \rangle_{x,y}\right)^2 \cdot \sum_{x,y} \left(X'_j - \langle X'_j \rangle_{x,y}\right)^2\right]^{1/2}}, \tag{4.5}$$

sometimes called centered anomaly correlation (coefficient) or pattern correlation (coefficient), where $X'_i = X_i - \langle X_i \rangle_t = X'_i(x, y, t)$ is the local climatological anomaly of variable X in the results of ensemble member i.

4.2 Influence of the ensemble size

The effect of the number of member simulations on estimating IV is twofold. One issue is the robustness of the estimation; smaller ensembles may generate a larger range of possible IV due to insufficient sampling of the model's phase space. The other question concerns the validity of the mean variability estimated by a variety of different ensembles of the same size. That is, the estimated IV of a small ensemble might not only be subject to random deviations from the true value but also be—on average—systematically too high or too low due to the ensemble size.

Here, both the robustness and systematic errors are examined using all possible sub-ensembles with six to nine members of the original 10-member Ensembles 2 and 3. Since this method involves intersecting ensembles, the results cannot be regarded as independent, identically distributed random variables. Alexandru et al. (2007) chose the same approach but used independent ensembles. However, the inclusion of all possibilities is expected to increase the validity of the conclusions drawn from those experiments herein.

4.3 Ratios of external and internal variability

The concept of predictability (Anthes, 1986) aims on a comparison between model errors due to IV and the expected difference between two arbitrary climate states. According to the theory, a steadily forced climate model has reached its predictability limit as soon as the IV has generated a variance among the solutions that corresponds to twice the error variance of a climatological time series. In a RCM, where the IV is limited by the boundary forcing, predictability is less affected by the time passed since the intializiation. Instead, the IV may never, occasionally, or permanently exceed the climatological, or "external" variability without growing continuously.

Based on these notions, several ratios of external and internal variability have been used in the literature. For pairs of six-hourly resolved simulations, Caya and Biner (2004) took the ratio of the instantaneous rms difference (internal) and the rms standard deviations of the monthly time series of a control run (external variability, Equation 2 there) for quantifying the predictability on a monthly basis. Adapting a concept used by Mikolajewicz et al. (2005), Döscher et al. (2010) quantified the external variability as standard deviation of the ensemble mean time series and compared it to the mean IV measured as the time mean of the biased ensemble standard deviation. Thus they ensured to separate the influence of the BCs from the internal processes. The ratio of

external to mean internal variability, called signal-to-noise ratio, gives an estimation of the relative dominance of the boundary forcing over the IV.

Dorn et al. (2012) applied a slightly different definition of the external-to-internal-variability ratio and defined the "mean external variability" as

$$\begin{aligned}\mathrm{MEV}\, X(x,y) &= \left\langle \sqrt{\frac{1}{N_t - 1}\sum_{t=1}^{N_t}(X_i(t) - \langle X_i\rangle_t)^2} \right\rangle \\ &= \langle \mathrm{SD}^*(X_i(t_1), X_i(t_2), \ldots, X_i(t_{N_t}))\rangle\,,\end{aligned}$$

i. e. the intra-ensemble mean of the sample standard deviations of the member time series, which takes into account all variations that occur within a single model run. Compared to the external variability of Döscher et al. (2010), the MEV therefore estimates the climatological statistics more realistically. Together with the domain mean of the mean IV (MIV), equal to the one of Döscher et al. (2010),

$$\mathrm{MIV}\, X(x,y) = \langle \mathrm{SD}^*\, X\rangle_t,$$

the domain mean of the MEV forms one definition of the "standard deviation ratio" used by Dorn et al. (2012):

$$\mathrm{SDR}\, X = \frac{\langle \mathrm{MEV}\, X\rangle_{x,y}}{\langle \mathrm{MIV}\, X\rangle_{x,y}}.$$

The SDR measures the domain-wide influence of the climatological variability—the climatological signal—compared to the domain-wide effect of IV.

Knopf (2006) derived another quantity, which discards the exact ratio in favor of information on the probability that the external variability dominates over internal variability. Here, the mean locking time fraction ("mean locking time" in Knopf, 2006) of a variable X is defined as

$$\mathrm{MLTF}\, X(x,y) = \langle \mathrm{LTF}\, X\rangle_t \quad \text{with} \quad \mathrm{LTF}\, X(x,y,t) = \begin{cases} 0, & \text{if } \mathrm{MIV}X/\mathrm{MEV}\, X \geq \epsilon \\ 1, & \text{else} \end{cases}$$

and is equal to the share of time steps (here: months) in which the ϵ-fold of MEV exceeds the MIV, a situation described as locking among the members. For a direct comparison of the variability measures, $\epsilon = 1$ is chosen in the analyses shown in the next chapter. Large values close to 1 indicate that predictability is generally high, whereas smaller values correspond to a larger probability of IV dominating the model output.

4.4 Correlation between variables

A pair of real-valued random variables (X, Y) for which their exists an affine relationship of the form $X = aY + b$ $(a \neq 0)$ are said to be linearly correlated; any change in one of the variables will cause a predictable change in the other. Random samples of two climate model variables related to each other may exhibit relationships that appear as affine with additional error terms, $X_i = aY_i + b + \epsilon_i$. The goodness of an error-free affine description of a very large sample $(\boldsymbol{X}, \boldsymbol{Y})$, i. e. the smallness and uniformity of $(\epsilon_1, \ldots, \epsilon_N)$, is measured by the Pearson correlation

$$\mathrm{R}(\boldsymbol{X}, \boldsymbol{Y}) = \frac{\mathrm{E}(\boldsymbol{X} \cdot \boldsymbol{Y}) - \mathrm{E}\,\boldsymbol{X}\ \mathrm{E}\,\boldsymbol{Y}}{\mathrm{SD}\,\boldsymbol{X}\ \mathrm{SD}\,\boldsymbol{Y}},$$

which takes values near ± 1 for a nearly linear correlation and values near 0 for almost no linear correlation. It is estimated for samples by the sample Pearson correlation

$$\mathrm{R}^*(\boldsymbol{X}, \boldsymbol{Y}) = \frac{\sum_i X_i Y_i - N\langle \boldsymbol{X} \rangle \langle \boldsymbol{Y} \rangle}{(N-1)\,\mathrm{SD}^*\,\boldsymbol{X}\ \mathrm{SD}^*\,\boldsymbol{Y}},$$

which is used henceforth for estimating the correlations between variables.

5 RESULTS AND DISCUSSION

The methods described in the last chapter are part of the analysis of internal variability (IV) regarding mean sea level pressure (MSLP, Section 5.1), sea ice extent (SIE, Section 5.2), and sea ice thickness (SIT, Section 5.3). The IV analysis of each variable is organized according to the following strategy. First, we select an appropriate spatially integrated measure of IV and compute 1979–2008 means of the respective measure using smaller sub-ensembles of E2 and E3 in order to evaluate the influence of the ensemble size on the estimation of IV (subsections *Ensemble size experiments*). Secondly, the temporal evolution and statistics of the spatially integrated IV (*Seasonal and interannual structure*) as well as spatial features associated with certain high or low IV cases are investigated and illustrated by means of representative example months (*Spatial structure*). Finally, we apply two different methods for quantifying the ratio of externally generated to internal variability deduced from the notion of climate predictability (*Ratios of external and internal variability*).

5.1 Mean sea level pressure

As outlined in Section 2.2, MSLP fields are especially useful for surveying atmospheric circulation patterns in the form of cyclones and anticylones which dominate the mean surface wind field. Therefore, measuring the domain-wide IV of the MSLP as anomaly correlation is expected to be more meaningful than measuring local ensemble standard deviations and integrating them over the domain, as done for the rms standard deviation. Furthermore, it will be shown that the rms standard deviation is sensitive to small inter-member shifts of gradient zones between pronounced low- and high-pressure areas. Such situations can, however, even occur in cases when the overall circulation is consistent among the members and the IV should be regarded as being low. The following analysis therefore draws upon the anomaly correlation as spatially integrated IV measure.

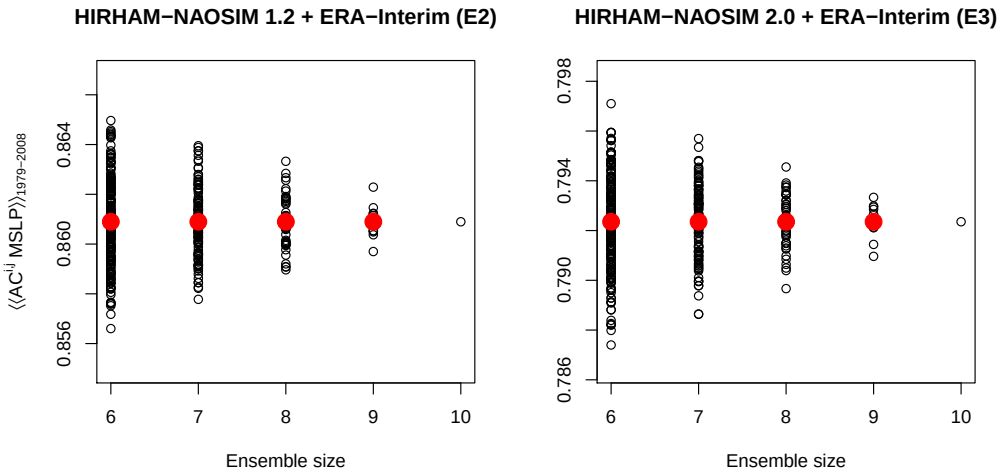

Figure 5.1: Time mean (1979–2008) of the annually averaged ensemble mean anomaly correlation of MSLP for different ensemble sizes. Ensemble sizes of 6–9 use all possible sub-ensembles generated from the respective full ensemble E2 (left) or E3 (right). Red dots denote the mean of all estimates obtained for each ensemble size.

Ensemble size experiments

Since Ensemble 1 (E1) contains only six members compared to ten members of E2 and E3, the first question concerns the robustness of the present IV estimation. The time mean taken over the period 1979–2008, which is common in all ensembles, of the ensemble mean anomaly correlation, calculated for all possible sub-ensembles of a certain size (Figure 5.1), shows scattering of the results between 0.857 and 0.865 for six-member sub-ensembles of E2 (left panel in the figure) and scattering between 0.787 and 0.797 for those of E3 (right panel). The variation, which is a measure of uncertainty in the IV estimation due to the ensemble size, decreases for larger ensembles. Nine-member sub-ensembles vary in their estimated IV within the ranges 0.860–0.862 for E2 and 0.791–0.793 for E3. The fact that the estimations of sub-ensembles converge toward the observed means of the 10-member ensembles is, however, no clear indication that the estimation using 10 members is especially robuts but primarily stems from the experimental design. That is, using different 10-member ensembles of the same configuration of model and boundary conditions (BCs) might further increase the scatter of the IV estimated by sub-ensembles. A robust estimation would be recognizable from practically no variation among the results of a smaller sub-ensemble. Apart from considerably differing in their mean magnitudes, the estimations behave very similar in both ensembles. Additionally

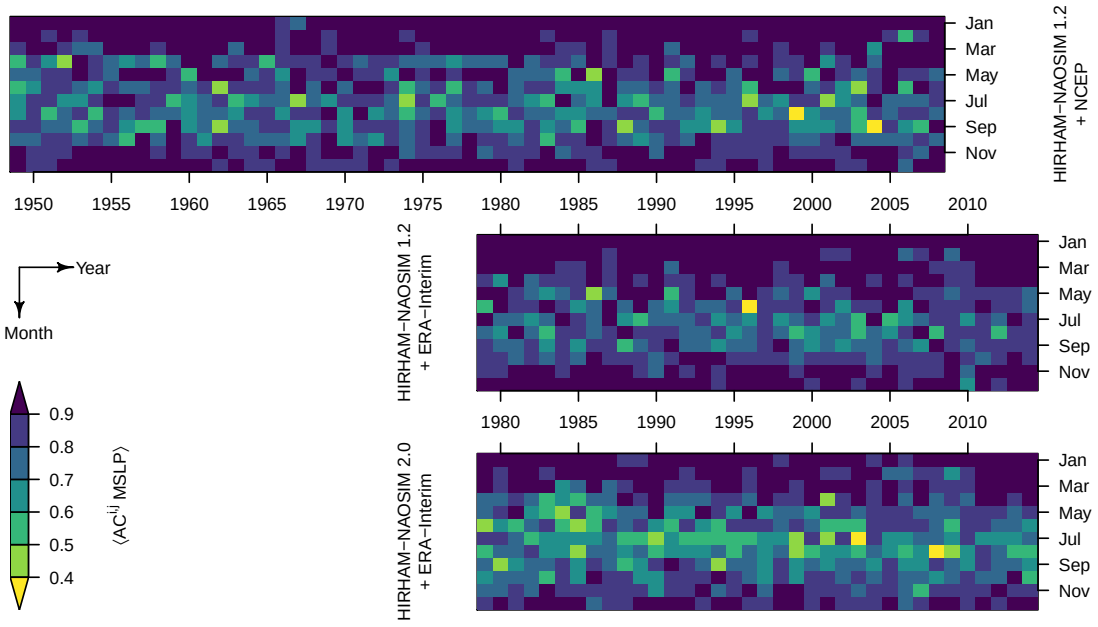

Figure 5.2: Ensemble mean anomaly correlation of monthly mean MSLP fields in E1 (top), E2 (middle), and E3 (bottom).

it can be stated that the means of the results of all sub-ensembles of fixed ensemble size (red dots in Figure 5.1) do not depend on the ensemble size.

The application of 10-member ensembles for estimating the IV of MSLP fields cannot be characterized as robust or non-robust. The possibility that differences in the IV magnitude between E2 and E3 are mainly due to the sampling is therefore recognized here but not further pursued in the analysis. Since Alexandru et al. (2007) found reasonably well estimations for 10- to 20-member ensembles for a RCM covering part of the North American domain, it is assumed that a sampling size effect is small. Using six members in E1 may cause stochastic deviations from hypothetical 10-member estimations though these deviations are not expected to exceed magnitudes of about 1 % of the mean anomaly correlations.

Seasonal and interannual structure

Looking at the time series of spatially integrated IV of the MSLP (Figure 5.2), a seasonal cycle of high IV in April–October and low IV in November–March is apparent. Particularly high IV, with an ensemble mean anomaly correlation less than 0.5, can be observed in all ensembles and primarily in summer. Extreme cases thereof are August 1999 ($\langle \mathrm{AC}^{i,j}\mathrm{MSLP} \rangle = 0.339$) in E1, June 1996 (0.317) in E2, and July 2003 (0.314)

in E3. Low IV cases can be attributed to values greater than 0.9 and are present in all seasons. Still, they are most prominent during winter months and take extreme values of 0.997 in January 1974 of E1, 0.997 in January 1994 of E2, and 0.982 in February 1989 of E3.

The described annual cycle with seasonal differences is consistent among the ensembles but experiences modulations on the interannual scale. Clear common interannual features in all ensembles are rare—one example being August 1999 with a local maximum of IV. Generally, periods and single months of relatively low or high IV are more similar in E1/E2 than E2/E3. Examples of such similarities in E1/E2 are high IV in May 1986, September 1988, and May 1991; anomalously low IV in August 1981, August 1988, and July 2004; and the year 1987 without pronounced seasonality.

Appreciable multidecadal trends are not present in any ensemble, except for slightly decreased IV during the last five years of E2 and E3. Comparing the time means of the common period 1979–2008, E1 shows a higher overall IV with a mean anomaly correlation of 0.841 as compared to E2 with 0.861. Since this value lies far outside the range determined for six-member sub-ensembles of E2 (Figure 5.1, left), the difference cannot be attributed solely to the ensemble size but can only result from the different BCs, which are the only difference between both ensembles. E3 shows significantly larger IV than E2 with a mean anomaly correlation of 0.792. Here, the choice of model is the only possible source of this difference.

To summarize these first ensemble comparisons, both BCs and the choice of model have a significant effect on both the magnitude and the interannual evolution of the MSLP fields' IV. The difference due to a change in the model version is larger than the difference due to other BCs. Since the newer model version features a better resolution, it is likely that the integration process allows for more degrees of freedom due to the increased number of grid points and thus higher IV. In this sense, switching to the new version is similar to running the RCM on a larger domain. Publications of such experiments (e. g. Rinke and Dethloff, 2000; Alexandru et al., 2007; Rapaić et al., 2010) exclusively report that IV increases with the domain size.

The question how BCs and model choice can affect the seasonality of IV can be answered by an investigation of the details in the annual cycle. Figure 5.3 displays the intra-annual positions, i. e. months, of minimum and maximum IV for each year. Time series thereof are plotted in the left panels, histograms with absolute frequencies of these time series in the right panels. The distribution widths observed in the histograms demonstrate that the annual cycle has a pronounced seasonality but shows variability from year to year. Some months feature both cases of minimum and maximum IV, namely April–July in

E1; February in E2; and November, April, and May in E3. While E1 and E2 have very similar seasonalities concluding from their histograms, E3 has slightly postponed minima and preponed maxima of IV, which will be substantiated in the following subsection. This implies that the properties of the new model version do not only foster IV but also marginally shift its extreme occurrences within the year.

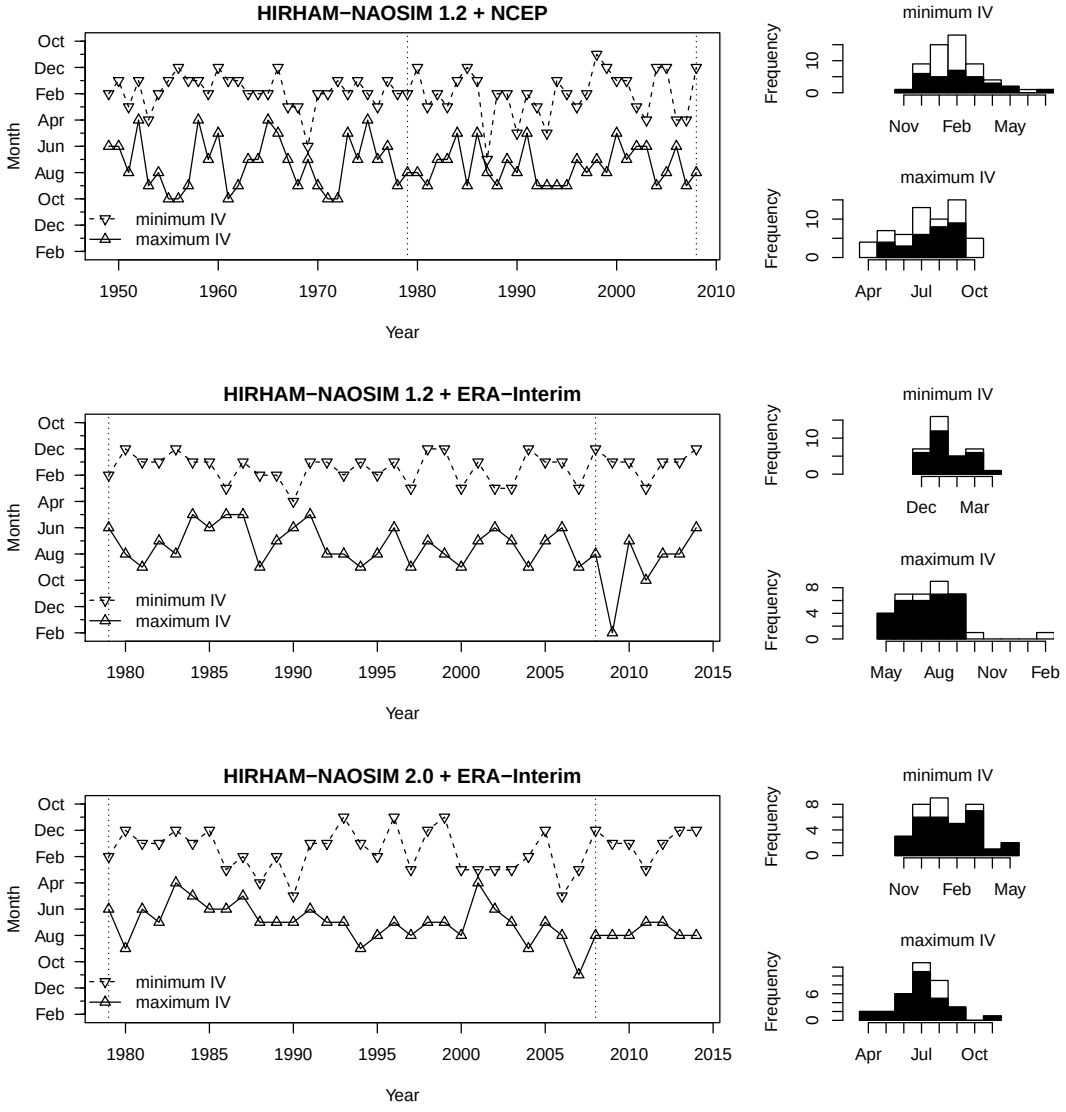

Figure 5.3: Months of minimum and maximum IV of MSLP for each year (left) and the distributions of minimum/maximum IV among the months (right). The period delimited by dotted lines is the 1979–2008 period common in all ensembles. Black histogram bars denote absolute frequencies within the common period, white bars these within the total period of each ensemble.

The detected annual cycle of IV coincides with the annually varying presence of solar radiation over the Arctic and the strength or weakness of the atmospheric surface circulation. Winter conditions with little irradiation and pronounced low-/high-pressure areas are stable since small-scale convection is reduced and the mid-troposphere circulation is characterized by strong cyclonic winds. Rinke et al. (2004) found a regime of higher IV during winter than summer, measured on a sub-daily scale during the SHEBA year in 1997/1998. They argued that under such circumstances, disturbances in atmospheric fields can more rapidly grow, be transported across, and stay within the Arctic domain. For monthly mean fields, used in this thesis, these disturbances are likely to be of less importance than inter-member differences in convection and the increased occurrence of cyclones over the Arctic Ocean, which are features of the summer season. The presence of solar radiation and its favoring the IV is stressed in the discussion of Dorn et al. (2012), whose results were also obtained for monthly mean fields and are consistent with the seasonality found here.

Spatial structure

For an investigation of the spatial features of the MSLP, i. e. patterns of low- and high-pressure areas, associated with anomalous low or high IV, exemplary months for every ensemble are selected. In order to select systematically, we first capture the annual extrema of the typical annual cycle seen in Figure 5.2 by choosing one three-month season of frequent maximum IV and one three-month season of frequent minimum IV for every ensemble. The reason for considering three months as representative for the minima or maxima of IV is that, on the one hand, they allow for covering large parts of the distributions shown in Figure 5.3 and, on the other hand, still ensure that one can actually speak of seasons, i. e. periods within which the typical atmospheric circulation can be regarded as somehow uniform. For each of these seasons we then select occurrences of especially low or especially high IV based on individual thresholds for each ensemble.

According to the distributions of minimum and maximum IV months in the common 30-year period (1979–2008, black-filled histograms in Figure 5.13), the three-month period with most total occurrences of minimum IV, hence called "typical minimum-IV season", is December–February (DJF) for E1 (18 occurrences out of 30 years), also DJF for E2 (23 occurrences), and January–March (JFM) for E3 (18 occurrences); typical maximum-IV seasons are July–September (JAS) for E1 (23 occurrences) and E2 (20 occurrences) and June–August (JJA) for E3 (22 occurrences). Where the choice of typical seasons would have been ambiguous based on 1979–2008 data only, we also took into account

Table 5.1: Three-month periods characterized as typical seasons for the occurrence of minimum or maximum IV of MSLP fields and thresholds used to define "low" ($\geq$ 90-% quantile) and "high" ($\leq$ 10 %) IV for the respective three-month seasons, rounded to the third decimal. Quantiles were taken from 1979–2008 IV data of the respective three-month season, e. g. all DJF data of E1 for representing typical minimum-IV months.

	E1	E2	E3
typical min-IV months	DJF	DJF	JFM
10-% quantile	0.884	0.900	0.827
90-% quantile	0.984	0.984	0.969
typical max-IV months	JAS	JAS	JJA
10-% quantile	0.561	0.635	0.505
90-% quantile	0.868	0.902	0.849

the distributions for the total periods (white-filled histograms in Figure 5.3). The IV values of these typical three-month periods for 1979–2008, collected for each ensemble, form the statistical populations for determining IV thresholds: "Low" IV in a typical minimum- or maximum-IV month is thus defined as being greater than or equal to the 90-% quantile, "high" IV as less than or equal to the 10-% quantile of the monthly ensemble mean anomaly correlations in the respective ensemble-specific population. See Table 5.1 for the threshold values.

In a second step, all months having low or high IV according to these thresholds were selected and combined as composites by computing the mean MSLP fields of all members and months for each situation (Figure 5.4). It comes to no surprise that features over the central model domain are less expressed in high-IV cases since differences in the members are most likely far off the boundaries and are averaged out by computing the composites. The relevant differences which are possibly related to the magnitude of IV are therefore to be found along the boundaries.

Particularly for E1, pressures are lower over the Barents Sea in high-IV cases of the minimum-IV season. Common features in the minimum-IV seasons of E1 and E2 are the Aleutian Low reaching further north and a slightly weakened Iceland Low in the cases of high IV. The latter characteristic is also present and more prominent in E3, together with anomalously high pressures over eastern Europe. During high-IV conditions in the minimum-IV season of E3, pressures over Alaska are lower, similar to the observation of a higher-reaching Aleutian Low in E1 and E2. All ensembles show weaker highs over Siberia and Canada when IV is high in the minimum-IV seasons. Part of these findings, the lower pressures over Siberia, Alaska, and Canada, might indicate a more frequent presence of cyclonic activity in these regions, which favors higher IV.

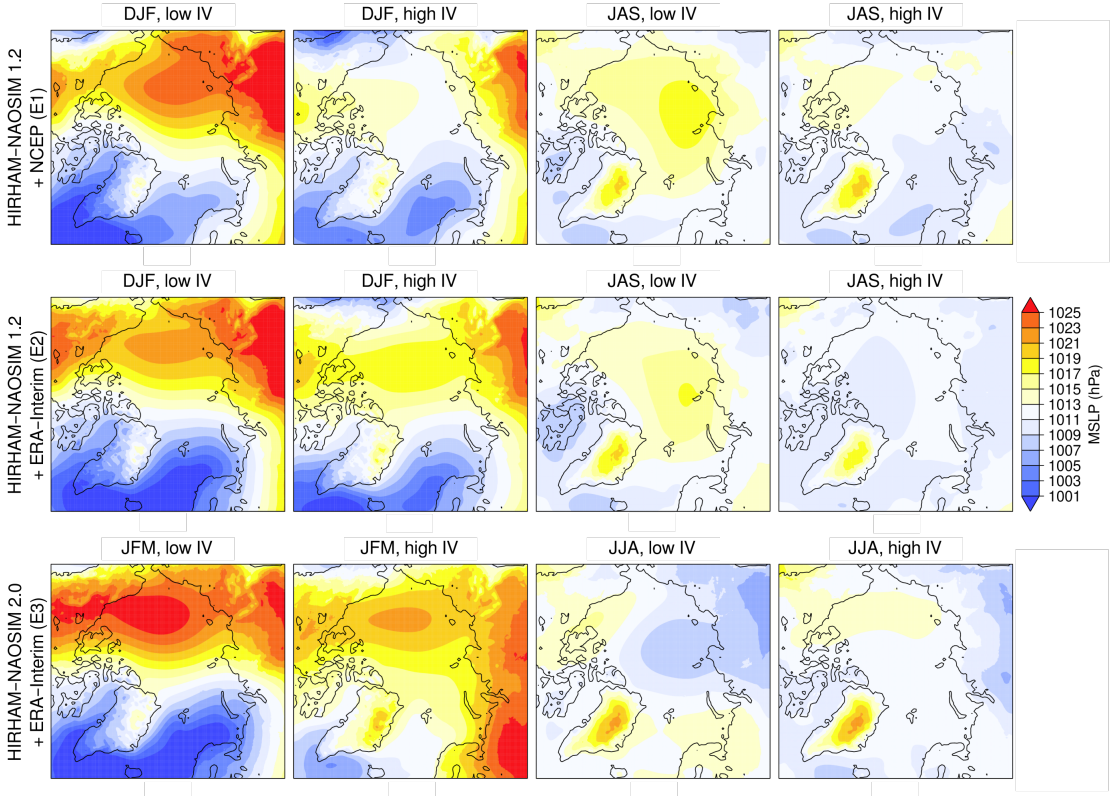

Figure 5.4: Average MSLP field composites of all members of all cases in typical minimum- or maximum-IV seasons showing low or high IV.

Pressures along the boundary show consistently small differences in the maximum-IV seasons. Over the Barents Sea, pressures are slightly lower for high IV in all ensembles. In E1 and E2, a weak mean anticyclone lies over the central Arctic Ocean when IV is low, which is replaced by a cyclonic structure in E3. The lower pressures in the central domain associated with higher IV in E1 and E2 suggest that cyclones are more frequent there. However, the different situation in E3 indicates that this cannot be a mechanism valid for all ensembles.

Exemplarily for the cases contained in the composites, we now look at the minimum-IV season of E1 and the maximum-IV season of E3. These were selected arbitrarily and should be regarded as illustrations of the composite analysis. For each of the seasons, the case of lowest IV (representing the low-IV cases) and the case of highest IV (representing high-IV cases) are selected from the period 1979–2008. Additionally to the MSLP fields of all ensemble members, the ensemble standard deviation fields and excerpts from the time series of anomaly correlation and rms ensemble standard deviation are shown in each figure.

The low-IV case of the minimum-IV season of E1, January 1984 (Figure 5.5a), displays a typical winter picture as described in Section 2.2. All members are in almost perfect accordance. In February 2006 (Figure 5.5b), the corresponding high-IV case, all boundary features seen in the composite analysis are especially strong: The Aleutian Low reaches far into the Chukchi Sea, the Iceland Low is retreated, and the Siberian High weak. The region of main variability, easily to spot in the ensemble standard deviation fields in the upper left panels of each subfigure, is north of the Kara Sea and results from mostly pronounced anticyclones or cyclones in the different members. In both of these cases, the time series of anomaly correlation and rms standard deviation (bottom left panels of each subfigure) are in good agreement. Note that the anomaly correlation was plotted with lower values at the top of the vertical axis in order to facilitate the comparison.

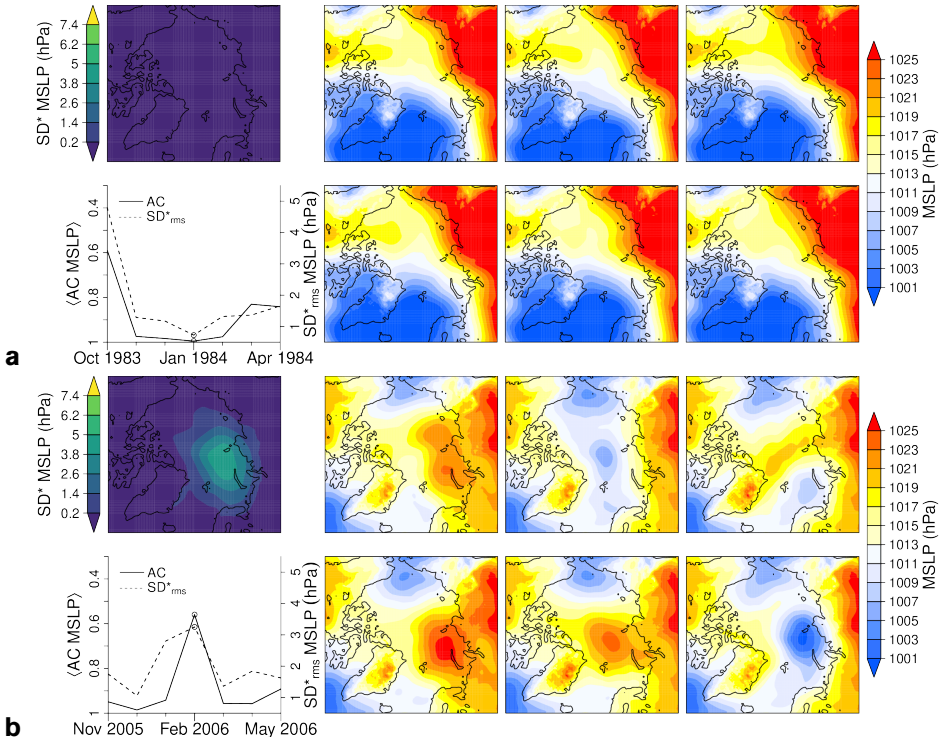

Figure 5.5: Members of MSLP fields (all panels except left column of each subfigure), ensemble standard deviation field (top left of each subfigure), anomaly correlation, and rms ensemble standard deviation (both bottom left of each subfigure) for the typically minimum-IV cases January 1984 (**a**, representing low IV) and February 2006 (**b**, representing high IV) of E1.

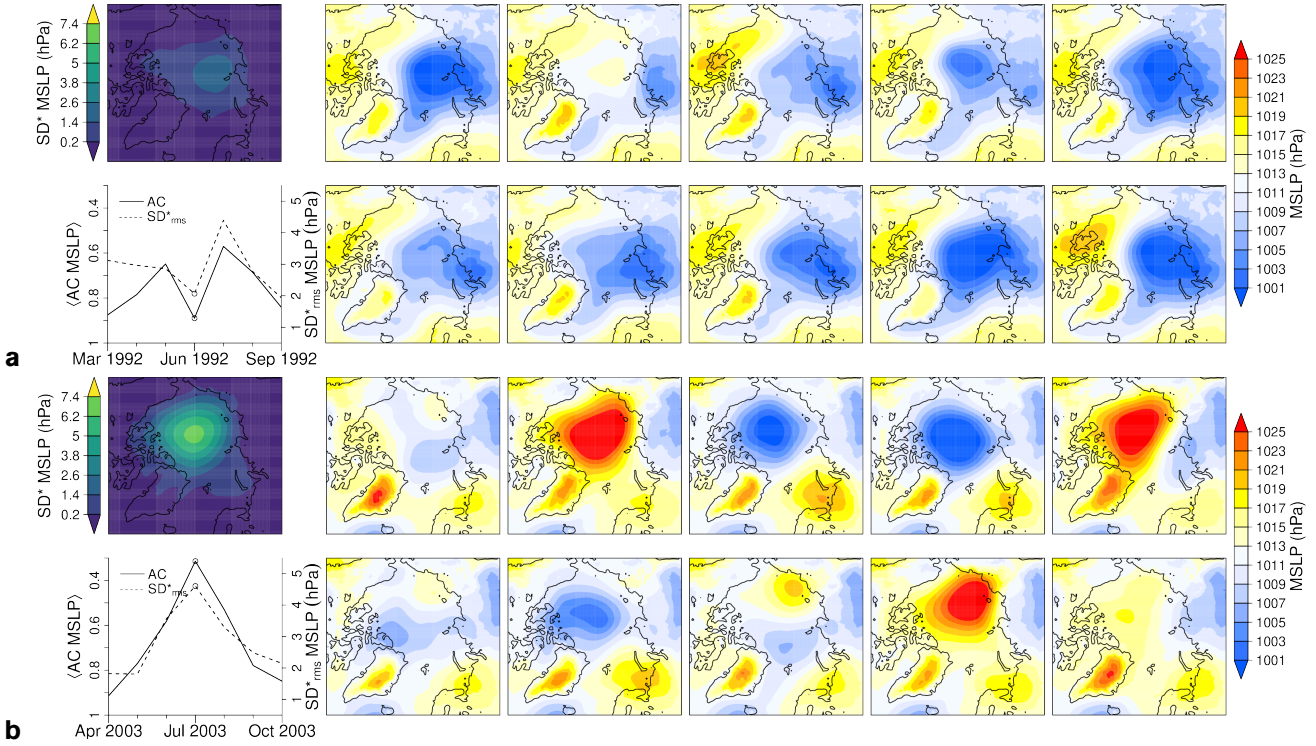

Figure 5.6: As in Figure 5.5 but for the typical maximum-IV cases June 1992 (**a**, low IV) and July 2003 (**b**, high IV) of E3.

In the maximum-IV season of E3, June 1992 (Figure 5.6a) exhibits the lowest IV of the period 1979–2008. With a central cyclone in most members, lower pressures over Siberia, and higher pressures over Canada, it can be regarded as a quite typical summer circulation. The high-IV case of July 2003 (Figure 5.6b) has similar BCs but shows an anomalous high-pressure area over northeastern Scandinavia / Barents Sea. Leading to the high IV, the central Arctic Ocean is overlaid by strong anticyclones in three members, pronounced cyclones in three members, and inexplicit conditions in four members. All in all, the boundary forcing seems to have little influence on the central Arctic conditions. Time series of anomaly correlation and rms standard deviation show a similar behavior in both cases.

Other example cases shown in the Appendix (Figures A.1, A.2, A.3, A.4) depict partly different situations than the ones just discussed. Yet, most of the typical features found in the composite analysis for minimum-IV seasons are also present there.

Before continuing with the analysis regarding predictability, the case of November 1982 of E2 is shown in Figure 5.7 to illustrate that measuring the IV of the MSLP as rms ensemble standard deviation can deviate considerably from the estimation using the anomaly

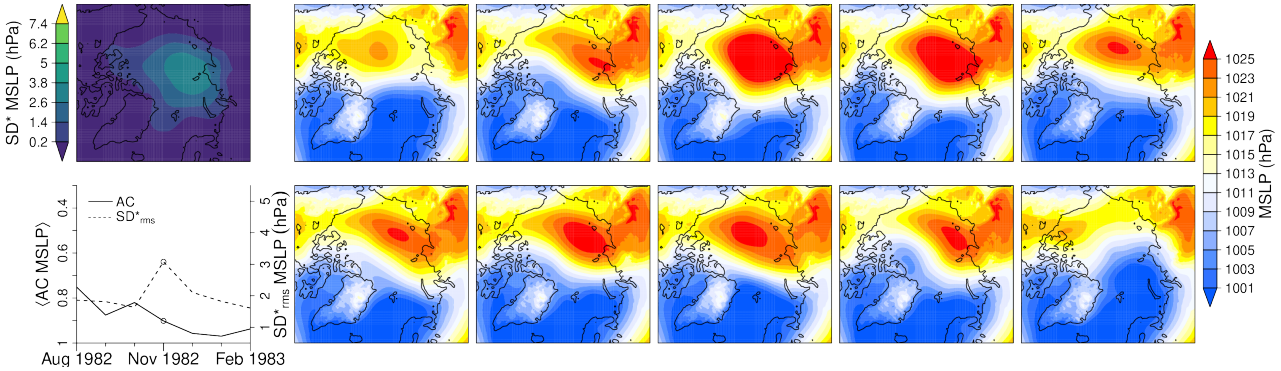

Figure 5.7: November 1982 of E2, a case of relatively low IV measured as anomaly correlation but relatively high IV measured as rms ensemble standard deviation.

correlation. The general pattern is that of a dipole with very high pressures north of and over Siberia, extending toward the Canadian mainland, and very low pressures from Baffin Bay over Greenland Sea to Barents Sea. Main variability, measured by the ensemble standard deviation (top left panel), takes place over the Kara and Laptev Seas, where the boundary between high and low pressure, featuring large gradients, is roughly located in all members but is shifted among them. The time series of the anomaly correlation and the rms ensemble standard deviation (bottom left panel), which are mostly consistent in the other discussed cases, deviate strongly in this particular case; $\mathrm{SD}^*_{\mathrm{rms}}\,\mathrm{MSLP} > 3\,\mathrm{hPa}$ indicates a comparably high IV—all values for E2 range between 0.7 and 4.0 hPa—, while $\mathrm{AC}^{i.j}\mathrm{MSLP} = 0.9$ rather marks consistency among the ensemble members.

Ratios of external and internal variability

Figure 5.8 shows the monthly standard deviation ratio (SDR), as defined in Section 4.3, of the MSLP fields in each ensemble (dashed line) along with the domain-averaged mean external variability (MEV) and the time mean of the domain-averaged ensemble standard deviation of MSLP (solid lines) covering the period 1979–2008. Dorn et al. (2012) analyzed the annual cycle of SDR for several variables, including MSLP, for the period 1948–2008, simulated with an ensemble using the same model, BCs, and initializations as in E1 here (Figure 4 there). The SDR cycle of E1 shown here (top left panel) resembles theirs except for some details due to the different choice of averaging period. E. g., the maximum in January found by Dorn et al. (2012) is lowered and surpassed by a maximum in March here, which is not as pronounced in the 1948–2008 averaging. The general course of the annual SDR cycle is the same in all ensembles but the time of minimum is preponed from September in E1 to July in E2 and E3. Maxima in E2 and E3 are found in January.

These results suggest a generally larger influence of IV during summer / early autumn than during winter / early spring on the model behavior. Still, the variability induced by the boundary forcing is dominant on average, as can be seen in more when looking on the solid curves whose ratio is the SDR. The mean external variability shows consistent maxima in January and minima in July, which illustrates the fact that boundary forcing of the Arctic climate system is weaker during the summer. In E3, the MEV has constantly larger values than in E1 and E2. Whether this is due to the computation of MEV, which does not explicitly exclude the IV compared to the "external variability" of Döscher et al. (2010), or the model's different reaction to the BCs, cannot be determined from the present analysis.

In order to see the contributions of different areas within the domain, the MLTF for each minimum- and maximum-IV season is mapped in Figure 5.9. The minimum-IV seasons exclusively demonstrate that IV rarely—if at all—dominates over the forced signal due to BCs during these months. The geographical distribution shows an almost symmetrical picture in the maximum-IV seasons of E1 and E2, which is probably merely due to the diminishing influence of BCs toward the central domain. The picture is similar but shows a shifted extremum over the Laptev Sea in E3. It is conspicious that, within the central

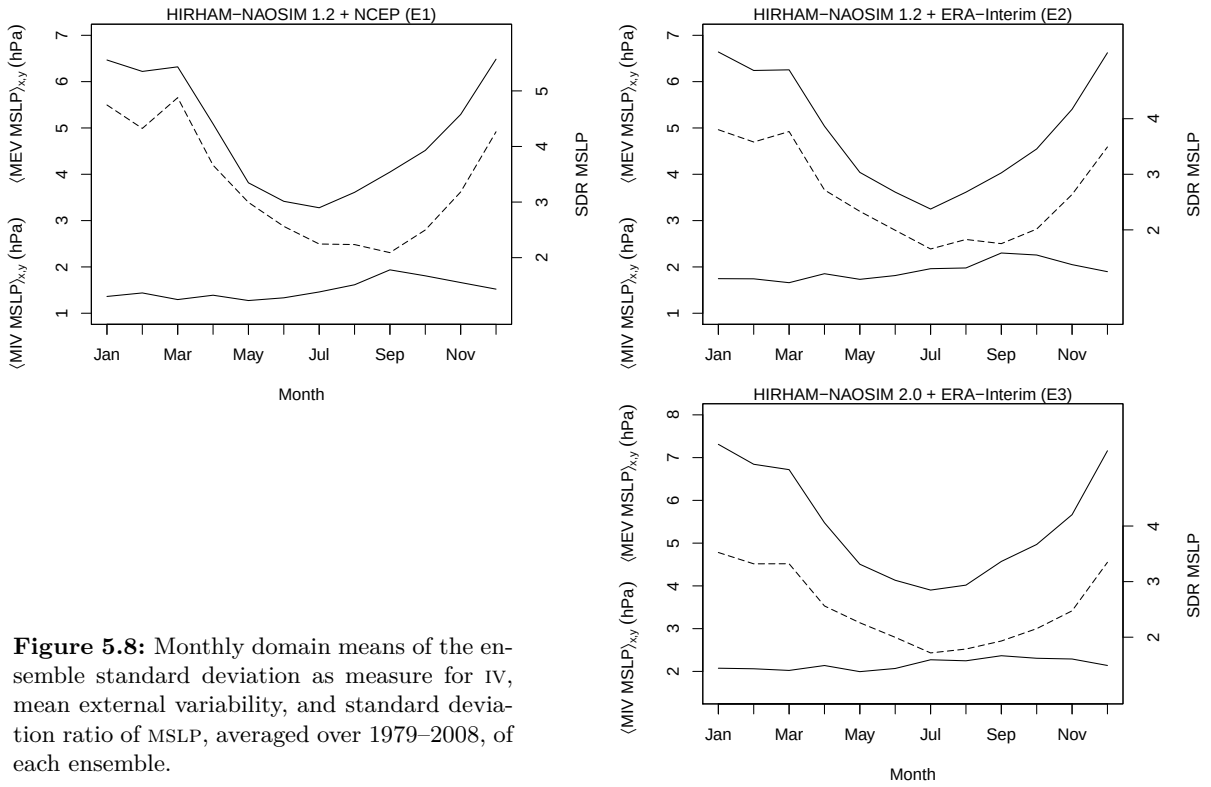

Figure 5.8: Monthly domain means of the ensemble standard deviation as measure for IV, mean external variability, and standard deviation ratio of MSLP, averaged over 1979–2008, of each ensemble.

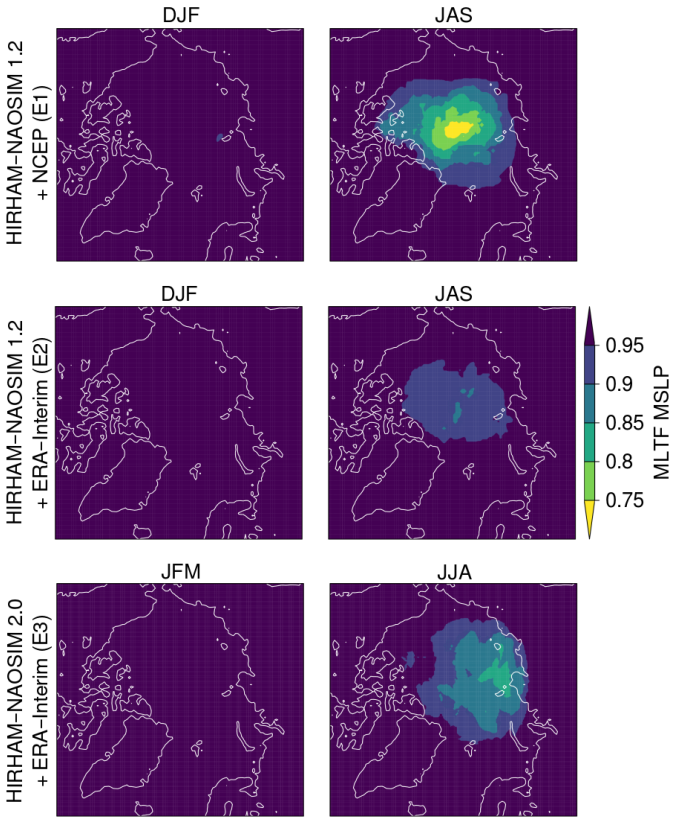

Figure 5.9: Mean locking time fraction with locking defined as the IV being smaller than the MEV ($\epsilon = 1$) of MSLP fields of the typical minimum-IV (left) and typical maximum-IV seasons (right), averaged over 1979–2008.

domain, E1 has much lower MLTF values, indicating a larger portion of months in which IV exceeds the MEV, than E2 and E3. This property is not evident from the domain-averaged measures shown in Figure 5.8 and might be due to differences in the frequencies of especially high IV occurring in the central domain of E1.

5.2 Sea ice extent

As a single variable characterizing the state of a particular sea ice concentration (SIC) field, the SIE shows domain-wide IV that is simply measured as the ensemble standard deviation.

Ensemble size experiments

A comparison of the 1979–2008 mean ensemble standard deviations computed from all possible sub-ensembles of E2 and E3 with sizes six to nine (Figure 5.10) shows considerable variation of the results for six members merely due to sampling. They span a range of $0.154–0.189 \cdot 10^6\,\mathrm{km}^2$ for sub-ensembles of E2 and $0.147–0.178 \cdot 10^6\,\mathrm{km}^2$ for sub-ensembles of E3. These ranges cover about 20 % or more of the absolute values. The variation reduces with larger ensembles but does not converge to a robust estimation below 10 members. Further, the mean estimated variability of all sub-ensembles (red dots in Figure 5.10) is not independent of the ensemble size but increases with the number of members. The 10-member mean for E2 and E3 is consistent with this observation.

These results suggest that the overall magnitude of IV of the SIE in E1 might deviate to a large extent (about some $10^4\,\mathrm{km}^2$) from the IV estimated by 10-member ensembles as a result of sparse sampling. As discussed before, whether E2 and E3 provide robust estimates cannot be concluded and will be ignored in the further analysis.

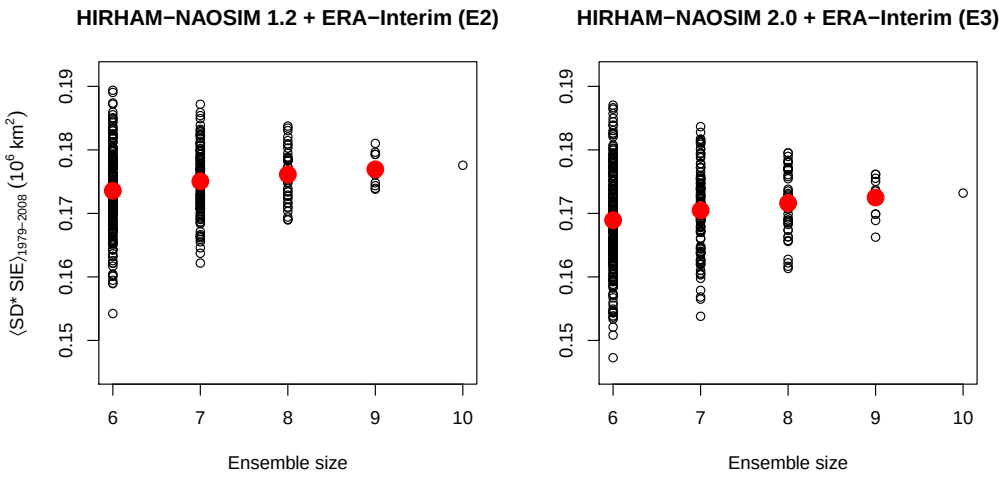

Figure 5.10: Time means (1979–2008) of the annually averaged ensemble standard deviation of the SIE for different ensemble sizes. Ensemble sizes of 6–9 use all possible sub-ensembles generated from the respective full ensemble E2 (left) or E3 (right). Red dots denote the mean of all estimates obtained for each ensemble size.

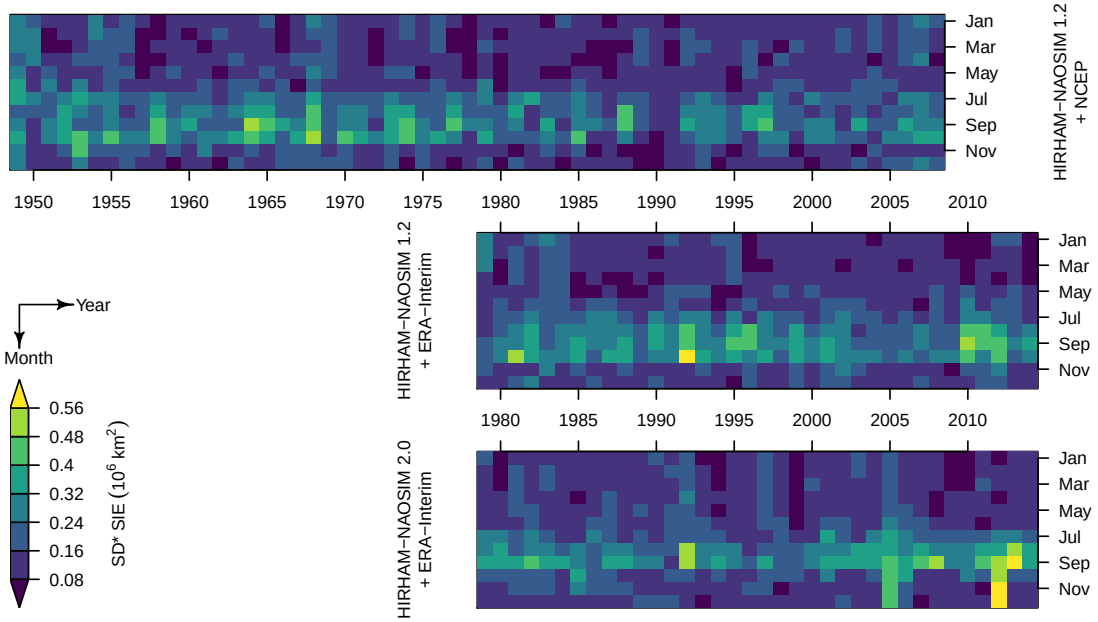

Figure 5.11: Ensemble standard deviation of monthly mean SIE in E1 (top), E2 (middle), and E3 (bottom).

Seasonal and interannual structure

The monthly mean IV (Figure 5.11) clearly shows a generally consistent seasonal structure with higher variability of more than $0.4 \cdot 10^6\,\mathrm{km}^2$ around late summer / autumn. Maximum IV of each ensemble takes values of $0.520 \cdot 10^6\,\mathrm{km}^2$ in September 1964 of E1, $0.602 \cdot 10^6\,\mathrm{km}^2$ in October 1992 of E2, and $0.790 \cdot 10^6\,\mathrm{km}^2$ in December 2012 of E3. Relatively low IV of less than $0.08 \cdot 10^6\,\mathrm{km}^2$ occurs more widely distributed in autumn through spring.

Overlaying this seasonal cycle, interannual features modulate the magnitudes of IV. Apart from the observation that IV may fluctuate considerably from year to year, the ensembles' time series show very few similarities. Perhaps the most striking one is the high summer/autumn IV in 1992 of E2 and E3, which corresponds to a small relative maximum in September 1992 of E1. A peculiarity of E3 are the occurrences of constantly high IV in September through December 2005 and 2012. As will be shown for December 2005 exemplarily, these cases feature a large additional field of sea ice south of Greenland in one member of the ensemble.

There are no notable overall trends regarding the magnitude of IV for the common period of 1979–2008 in any ensemble. Yet, E1 shows higher maximum summer/autumn IV in the years before 1979 than the remaining period, especially during the 1960s. Com-

paring only the common period, E1 has a noticeably lower mean IV ($\langle \mathrm{SD}^* \mathrm{SIE} \rangle_{1979\text{–}2008} = 0.160 \cdot 10^6\,\mathrm{km}^2$) than E2 and E3 (0.178 and $0.173 \cdot 10^6\,\mathrm{km}^2$, respectively). This might be due to the sampling size since the value lies near the lower margin of, but inside the 6-member range of E2 sub-ensembles shown in Figure 5.10, left. An effect of BCs on the mean IV is possible and could additionally explain the comparably strong deviation of E1 from E2 and E3.

The comparison of E1 and E2 indicates—exemplarily for the SIE—that a different choice of BCs data can result in a different interannual behavior of IV, as could be expected from the mechanism of BCs limiting internally generated variability. Moreover, both the seasonal and interannual development of the IV are also subjected to differences in the model itself, as shown by the comparison of E2 and E3. This fact shall be investigated further and discussed in the following paragraphs.

The seasonal cycle of IV of the SIE, especially the late summer / early autumn maximum, exhibits a relationship with the SIE, which itself has a reliable cycle of maxima in late winter and minima in late summer (arbitrarily chosen equidistant example years in Figure 5.12) in all ensembles. In fact, while maximum SIE is distributed over February–April in all ensembles, minimum SIE occurs primarily in September (E1), only in September (E2), or equally August and September (E3). The slight shift of minimum SIE between E2 and E3 (not shown) concurs with a shift of maximum IV from September/October in E2 to mainly September in E3 (Figure 5.13). That is, highest variability prevails when the ice cover starts growing again.

Figure 5.13 allows for a more detailed investigation of the seasonal evolution based on the distributions of maximum/minimum IV among the months. Maximum IV, especially

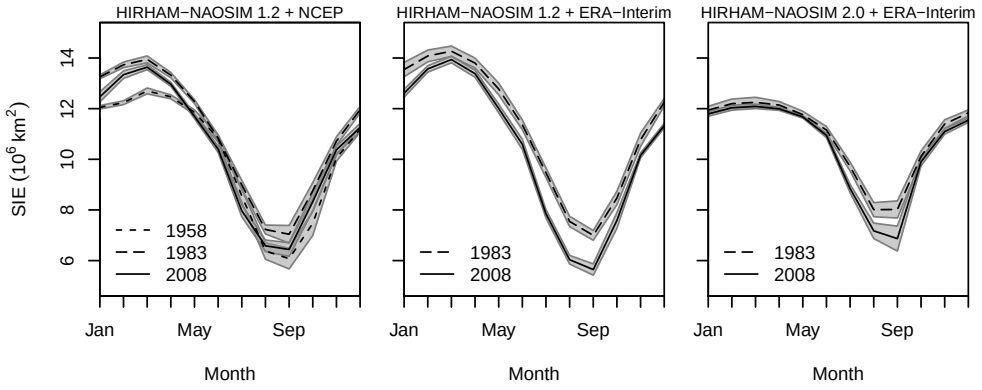

Figure 5.12: Ensemble mean of monthly mean SIE with 2-SD* range ($\langle \mathrm{SIE} \rangle \pm \mathrm{SD}^* \mathrm{SIE}$) indicated as gray buffers for the years 1958, 1983, and 2008. These years in equidistant 25-y intervals have been selected arbitrarily but in order to cover as much of the simulated periods as possible.

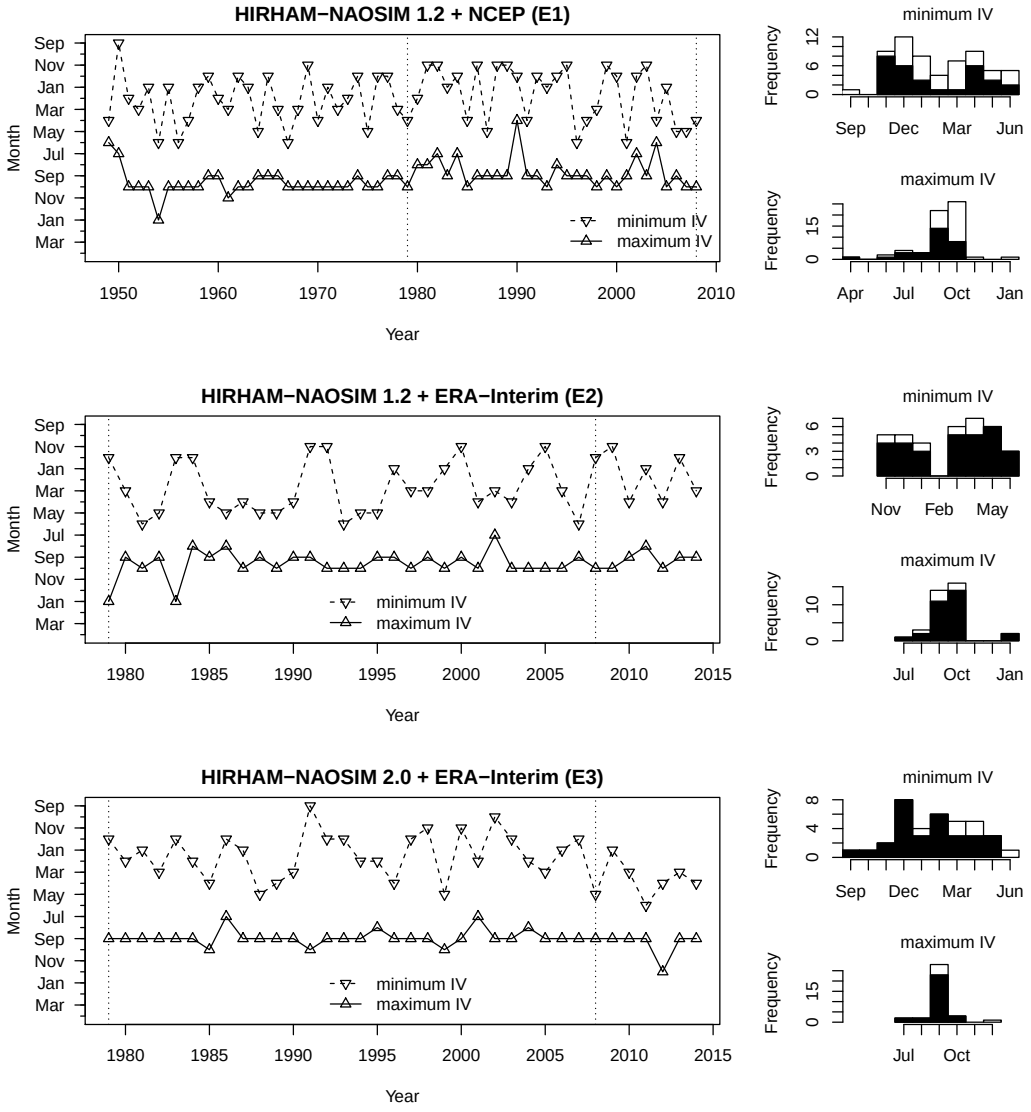

Figure 5.13: As in Figure 5.3 but for SIE.

in E2 and E3, has narrow distributions and accumulates around September/October, whereas minimum IV extends over all months from September to June, all of which cover the half-year of larger SIE (December–May). Occasionally the minimum- and maximum-IV seasons overlap in their distributions, namely in January, April, June, September, and November of E1; in January of E2; and in September, October, and December of E3.

The large influence of the atmospheric circulation on the sea ice drift is likely to be a reason for the high IV of the SIE in late summer / early autumn, since qualitative differences in the MSLP fields, which are more frequent in summer, can lead to variations in the sea ice export from or import onto the central Arctic Ocean as well as favor divergent or convergent motion (cf. Sections 2.2, 2.3). Higher cyclone frequencies over Siberia during summer can also have an impact on the SIC, and hence on the SIE, along the Siberian coast. That the annual IV maxima of the SIE are delayed compared to those of the MSLP could be explained by the observation that the effects of atmospheric variations on sea ice during summer can accumulate over the melting period (Serreze and Barry, 2005). These effects could then be overridden as soon as the atmosphere returns to a stronger larger-scale circulation in October and ice starts growing again. Additionally to the direct influence of the MSLP, the presence of stronger solar irradiation comes with variable thermodynamic effects on the ice retreat, which can also accumulate over the summer season. During late autumn and winter, polar night conditions in the central Arctic and the strong BC forcing probably dampen disturbances in the sea ice conditions and reduce the IV. The low IV at maximum SIE and beyond can further be explained by the geographic boundaries, i. e. coastlines, that coincide with large parts of the sea ice boundary and thereby limit the spatial opportunities for a varying SIE.

Spatial structure

Having found a relation between the annual cycles of SIE and its IV, it shall be investigated whether any characteristics in the position of the sea ice boundary are associated with anomalous low or high IV. As done for MSLP, we therefore determine typical minimum- and maximum-IV seasons characterizing the annual cycle, and distinguish between especially low and especially high IV cases for each of these seasons.

The typical minimum-IV seasons, i. e. these with most occurrences of minimum IV in 1979–2008, are November–January (NDJ) for E1 (17 occurrences), March–May (MAM) for E2 (16 occurrences), and December–February (DJF) for E3 (17 occurrences) (typical minimum-IV months). Typical maximum-IV seasons (also for the common period 1979–2008) are August–October (ASO) for all ensembles (E1: 25, E2: 27, E3: 28 occurrences). For representing low-IV cases in each of these periods for each ensemble, we select all months in which the IV does not exceed the 10-% percentile of all IV data obtained in the three-month period for 1979–2008. Similarly, high-IV cases are defined as having SD^* SIE at or above the 90-% percentile. Table 5.2 summarizes the thresholds for each ensemble.

In a second step, all months having low or high IV according to these thresholds are selected and combined as composites by computing the mean SIC fields of all members and months (Figure A.5). While this strategy seems to work reasonably well for MSLP fields, as seen in Section 5.1, its use is questionable in the case of SIE for the following reason. The potential presence of a composite SIE or SIC signal due to certain IV conditions could only be interpretable if the variability of SIE due to the selection of different cases is small enough. That is, the composite analysis is faced with the question whether the "external" variability of the SIE among the selected cases is larger or smaller than the IV which the analysis aims at. Measuring the ratio in question as intra-composite sample

Table 5.2: Typical seasons for the occurrence of minimum or maximum IV of SIE and thresholds used to define "low" ($\leq$ 10-% quantile) and "high" ($\geq$ 90 %) IV for the respective three-month season, rounded to the third decimal. Quantiles were taken from 1979–2008 IV data of the respective season.

	E1	E2	E3
typical min-IV months	NDJ	MAM	DJF
10-% quantile (in 10^6 km^2)	0.073	0.068	0.080
90-% quantile (in 10^6 km^2)	0.177	0.189	0.173
typical max-IV months	ASO	ASO	ASO
10-% quantile (in 10^6 km^2)	0.138	0.181	0.140
90-% quantile (in 10^6 km^2)	0.347	0.369	0.371

standard deviation (computationally equal to the ensemble standard deviation) of the ensemble mean SIE (external) divided by the composite mean of the ensemble standard deviations of the SIE (internal variability), we obtain values between 1.4 (E1, high IV in ASO) and 10.7 (E2, low IV in MAM). In other words, the prospected member-to-member differences in the sea ice boundary position are essentially overridden by the SIE differences between the various years and months in all composites. Since this measure corresponds to the signal-to-noise ratio used by Döscher et al. (2010), the role of IV even tends to be overestimated as compared to the standard deviation ratio by Dorn et al. (2012) (cf. Section 4.3).

In the light of these findings it is difficult to interpret any difference found between the composite SIC fields of Figure A.5 as a clear mark of IV. It should, however, still be mentioned that for E1 and E2 those differences are very small and only rarely exceed an absolute value of 30 % in the marginal ice zone during the minimum-IV seasons. In contrast, E3 exhibits less SIC all over the Arctic Ocean when IV is especially high as compared to low-IV cases in the maximum-IV season (ASO).

To evade the problems of the composite analysis, we now look at examples, namely the two cases of lowest and highest IV within the minimum-IV season of 1979–2008 and the two extremes within the maximum-IV season of each ensemble, also chosen for the common period 1979–2008. In addition to the sea ice boundaries (contours where the SIC equals 15 %) of all members, MSLP composites of the three preceding months are plotted. As stated in Section 2.3, MSLP is one of the factors governing sea ice motion and thereby the SIE but the understanding of a certain sea ice condition often requires additional knowledge about the system history, e. g. special atmospheric events, intra-annual preconditioning, and long-term modes of MSLP variability. A somehow comprehensive discussion of the physical interactions therefore falls out of the scope of this thesis.

Figure 5.14 contrasts the ensemble sea ice boundaries and preceding MSLP fields of November 1999 with those of January 2007, both of which are cases of extreme IV within the minimum-IV season of E1, the first having lowest and the latter highest IV. In the high-IV case, variability is present along most parts of the Atlantic sea ice boundary, i. e. the Labrador, Greenland, and Barents Seas. The mean patterns of MSLP show high-reaching (i. e. extending far north) low-pressure areas in some members. These areas cover the whole of the Arctic sea ice boundary and might be connected with frequent occurrences of synoptic cyclones, which come with increased baroclinic instability. Over the central Arctic Ocean, the MSLP member solutions discordantly show cyclonic and

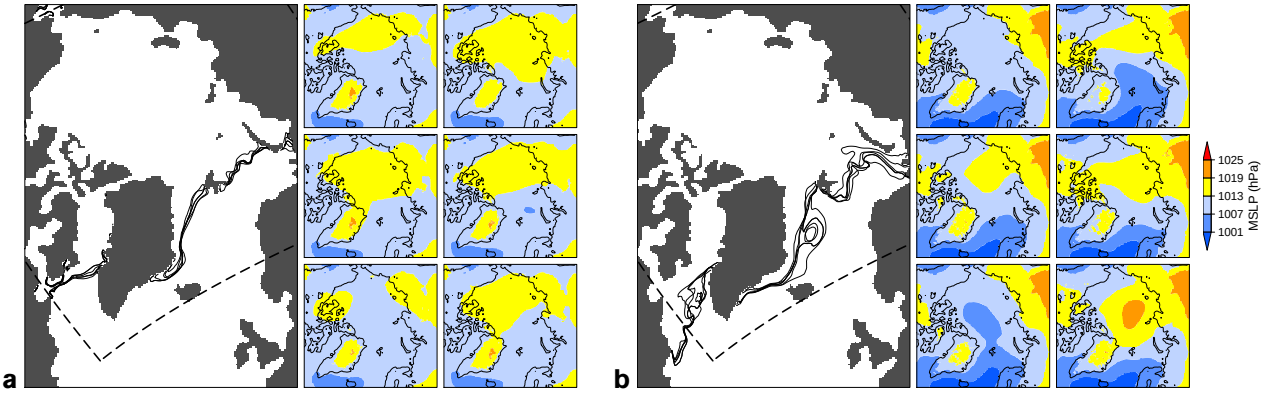

Figure 5.14: E1 member results of sea ice boundaries in November 1999 (**a**) and January 2007 (**b**) with corresponding ensembles of MSLP fields, averaged over the preceding three months. Both cases are examples of typical minimum-IV months with the November 1999 case representing low and the January 2007 case high IV. Dashed lines in the left panels denote the boundary of the HIRHAM grid.

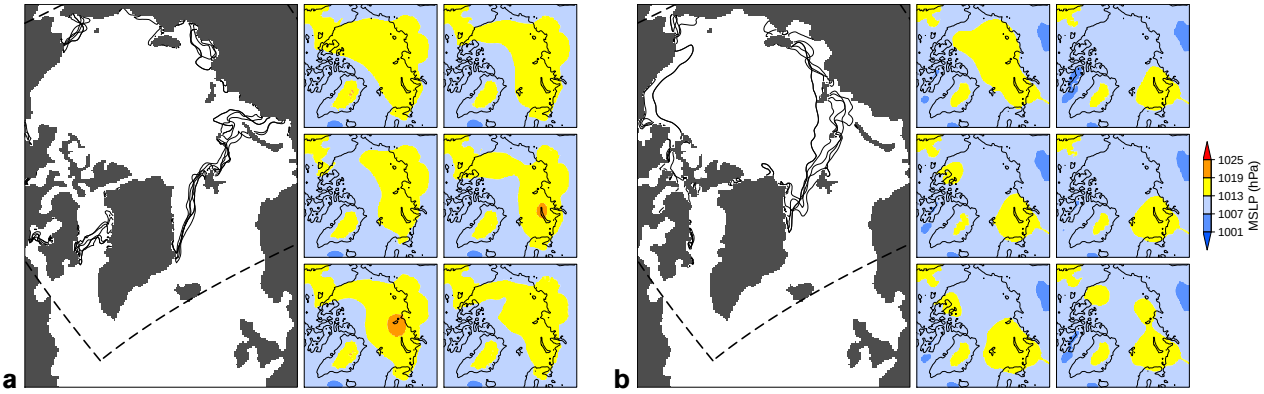

Figure 5.15: As in Figure 5.14 but for the typical maximum-IV cases October 1990 (**a**, low IV) and September 1988 (**b**, high IV) of E1.

anticyclonic structures, which cause divergence and convergence, respectively, of the sea ice and thus can lead to variations in the SIE.

The comparison of October 1990 as low-IV case and September 1988 as high-IV case of the maximum-IV season of E1 (Figure 5.15) demonstrates that larger parts of the Arctic coastlines can be practically ice-free during minimum SIE. Consequently, the regions of main variability in the sea ice boundary are more widespread than in winter/spring. In October 1990, they include the Barents/Kara Sea and Laptev Sea. In the high-IV case, main variability originates north of the Barents/Kara Sea and the Beaufort Sea. The MSLP conditions in both cases have weak regional differences. Nevertheless it appears that higher IV of the SIE comes with more variable MSLP conditions over the central Arctic Ocean, again possibly affecting the sea ice divergence. A low pressure center over

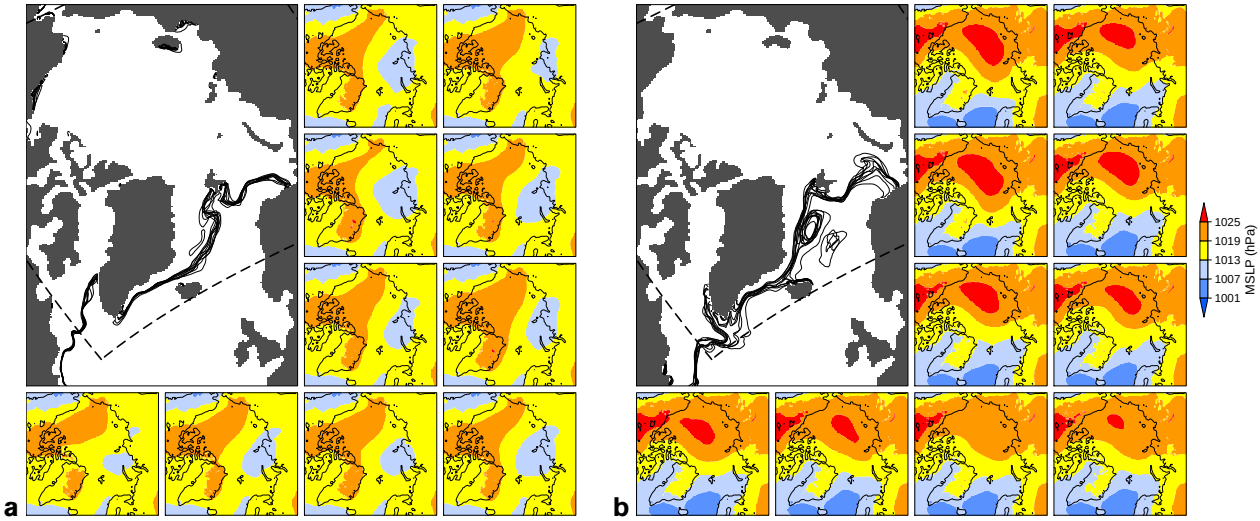

Figure 5.16: As in Figure 5.14 but for the typical minimum-IV cases May 1988 (**a**, low IV) and March 1979 (**b**, high IV) of E2. Note that MSLP composites in **b** were calculated for JF instead of DJF since December 1978 is not covered by the model output.

Siberia before September 1988 is present in all members and connects to the generally low-pressure conditions over the Arctic Ocean in some members, which might indicate cyclones migrating from Siberia northward. This is not the case in October 1990, where higher pressures dominate most of the Siberian coast and prevent cyclone migration.

For the minimum-IV season of E2, May 1988 has the lowest and March 1979 the highest IV in 1979–2008, both shown in Figure 5.16. Largest contributions to the IV of the SIE in March 1979 are found south of Greenland, the Greenland Sea, and the Barents Sea. As seen in the E1 cases, lower pressure prevails along the sea ice boundary and brings cyclonic activity before the SIE has its maximum IV. In contrast to E1, the overall atmospheric circulation shows no appreciable IV in both cases.

The maximum-IV cases of E2, August 1979 with low and October 1992 with high IV (Figure 5.17), show sea ice boundaries off the coasts with main variability north of Svalbard and northeast of Greenland (August 1979) and Barents through Laptev Seas as well as the Chukchi Sea (October 1992). Preceding MSLP fields are weak and have variable conditions over the Arctic Ocean.

February 1994 and December 2005, both examples of the minimum-IV season of E3, are very similar in the position of the main sea ice boundary and show large consistency among the members (Figure 5.18). What makes December 2005 still an anomalous high-IV case is the presence of an additional area of sea ice south of Greenland in member E3-C, which starts to form in late summer and vanishes by early 2006. The high IV

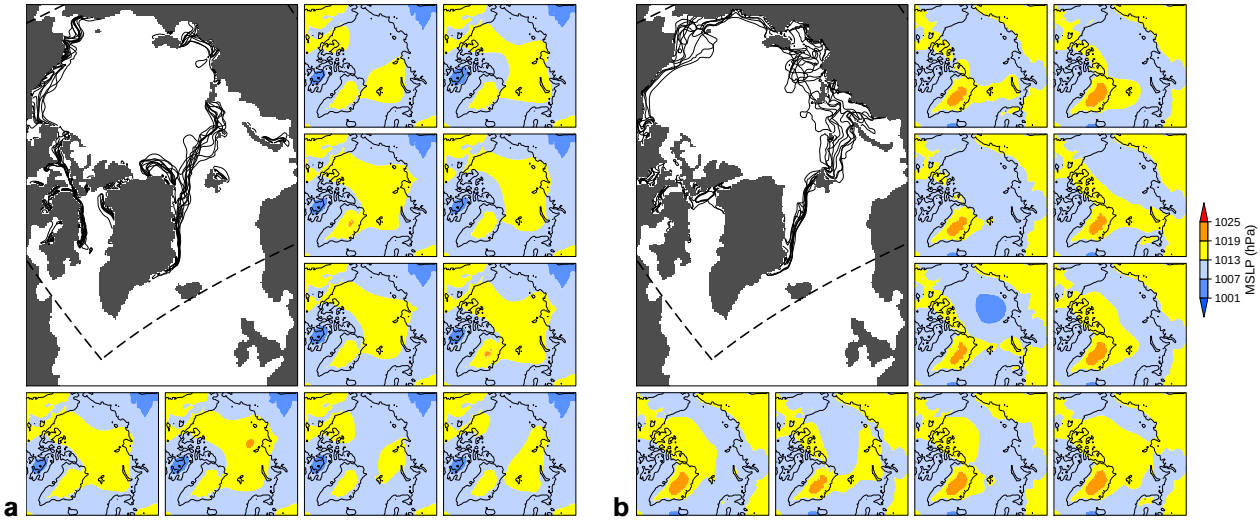

Figure 5.17: As in Figure 5.14 but for the typical maximum-IV cases August 1979 (**a**, low IV) and October 1992 (**b**, high IV) of E2.

therefore needs to be attributed to late summer conditions of ice. Note that apart from this particularity and despite the strong Iceland Low in February 1994 and high-reaching low pressure over the Greenland, Barents, and Kara Seas—perhaps resulting from cyclone paths—in December 2005, the members agree well in their location of the sea ice boundary.

October 1995, a low-IV case of the maximum-IV season of E3, and September 1992, high IV, differ largely in their variability. While all members agree well regarding their sea ice boundary in October 1995, the high-IV case is characterized by variability especially in the northern Barents Sea and the Kara and Laptev Seas. Relatively low pressure is dominant over Siberia in both cases but it extends widely over the Arctic Ocean in all members in October 1995. The sea ice field of September 1992 has experienced very different MSLP conditions over the Arctic Ocean depending on the member. Thus, sea ice divergence and convergence may be a mechanism for enhancing IV.

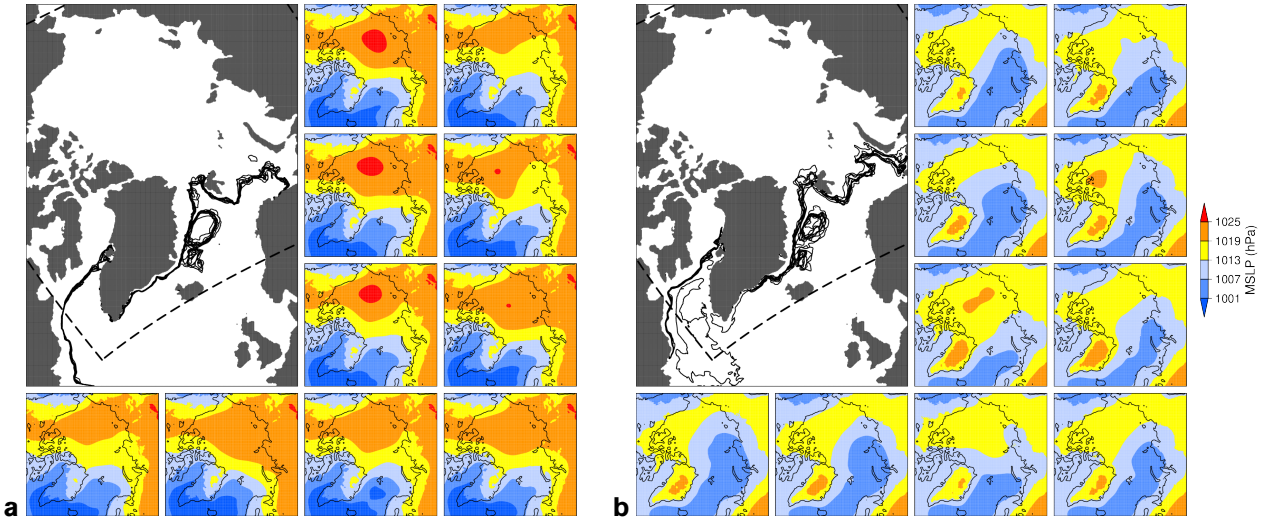

Figure 5.18: As in Figure 5.14 but for the typical minimum-IV cases February 1994 (**a**, low IV) and December 2005 (**b**, high IV) of E3.

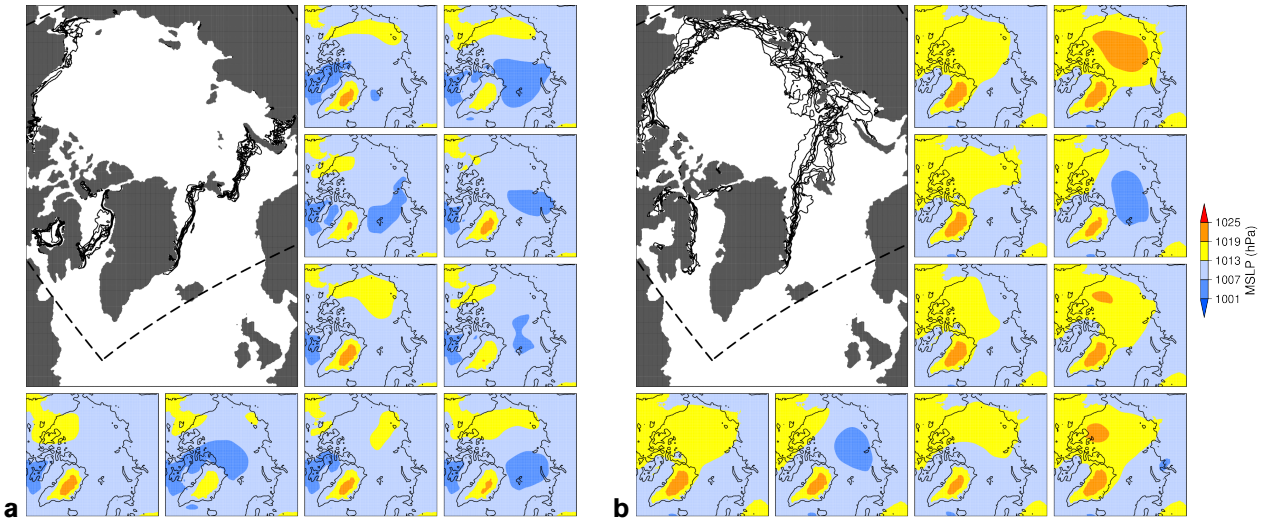

Figure 5.19: As in Figure 5.14 but for the typical maximum-IV cases October 1995 (**a**, low IV) and September 1992 (**b**, high IV) of E3.

Correlation with mean sea level pressure

The previous discussions of MSLP conditions affecting the internal SIE variability were either too rough or too selective for drawing general conclusions about typical spatial features. One possibility for assessing the overall effect of the atmospheric spring/summer circulation on the IV of the minimum-SIE months is presented by Döscher et al. (2010). They took—for every ensemble member of a coupled pan-Arctic RCM—the time-mean sea level pressure fields of May–September for each year of the period 1980–2000, concatenated the time series of all members, and correlated the resulting time series at every grid cell with the time series containing the SIE ensemble standard deviations of the annually minimum SIE, which was copied and concatenated to match the length of the MSLP time series. Their resulting map (Figure 10 there) shows a region of negative correlation coefficients less than -0.3 surrounding Greenland and extending from Baffin Island to Iceland, weaker negative correlations southward, toward Scandinavia, and across the Arctic Archipelago and the central Arctic Ocean toward central/eastern Siberia. Strong positive correlations greater than 0.3 were found over central/western Europe and the southern Barents and Kara Seas. This pattern corresponds to low pressure anomalies over Greenland, high pressure anomalies over Europe, and thus surface winds causing sea ice import through Fram Strait and the Barents Sea during high IV of the SIE in August/September.

Here, the same kind of analysis is conducted on the ensemble data over the 1979–2008 period, using the Pearson correlation (Figure 5.20). All ensembles associate a high-pressure anomaly over Scandinavia / northeast Europe with high IV of the SIE. Apart from that, the ensembles widely disagree. E1 shows the most similarities with the result of Döscher et al. (2010) as it features negative correlations over Iceland, Greenland, and the Arctic Ocean. However, other areas of negative correlations are shifted toward Canada/Alaska. Correlations do not exceed 0.44 or undercut -0.28. The main feature of sea ice import from the Greenland and Barents Seas during high IV is therefore present but weak. In E2, negative correlations prevail over Scandinavia and eastern Siberia while the conditions over the central Arctic Ocean are essentially unstructured. Statements about certain features in the ice drift are difficult to derive. Finally, E3 shows a quite clear structure; it is composed of a band of negative correlations extending from Iceland to central Siberia and a band of positive correlations extending from Labrador Sea to Chukchi Sea. Strongest correlations of -0.4 and 0.6 are found in central Siberia and the Labrador Sea. In the case of a highly variable SIE, this pattern represents surface

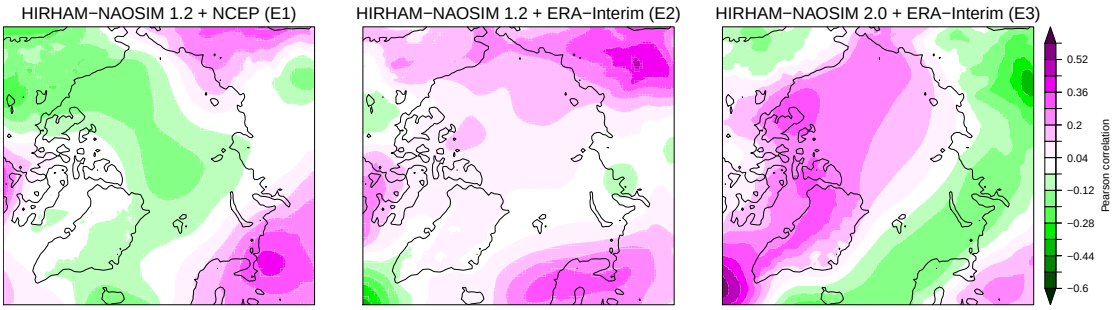

Figure 5.20: Correlation of 1979–2008 spring/summer (MJJAS mean) MSLP fields and time series of IV of minimum-SIE months.

winds enhancing the Transpolar Drift Stream and ice export through Fram Strait, both of which are generally weaker during summer (cf. Section 2.3).

To test the robustness of the correlation pattern in E1, we additionally compare the results for the 30-year periods 1949–1978, 1959–1988, and 1969–1998 (Figure 5.21) with the 1979–2008 result. In fact, the pattern undergoes a complete conversion between 1949–1978 and 1979–2008. The former climatology (Figure 5.21a) is characterized by positive correlations over Greenland, the Baffin Bay, Alaska, and eastern Siberia and negative correlations over the Barents Sea, the Kara Sea, and central Siberia. After weakening during the following decades (Figure 5.21b), the pattern shifts with the negative correlations mainly migrating toward the central part of the domain and Greenland, which oust the positive correlations. The conversion starts in the 1969–1998 (Figure 5.21c) climatology until it reaches the conditions already described for 1979–2008.

These results suggest that the contributions of MSLP fields to the SIE variability in late summer are diverse and not consistent among different ensembles and periods. Rather, individual assessments of selected situations are necessary to gain a meaningful insight into the mechanisms of IV observed in the model-generated SIE.

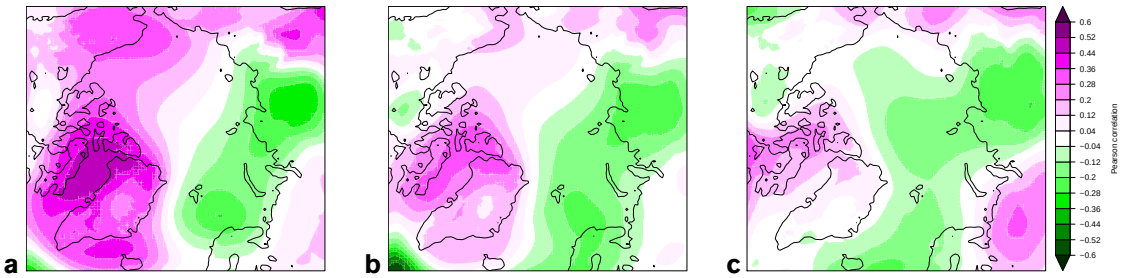

Figure 5.21: Correlation of MJJAS mean MSLP fields and time series of IV in minimum-SIE seasons of E1 for the 30-year periods of 1949–1978 (**a**), 1959–1988 (**b**), and 1969–1998 (**c**).

Ratios of external and internal variability

For the SIE, the monthly standard deviation ratio (SDR), calculated here as ratio of the 1979–2008 mean monthly external variability (MEV) and the 1979–2008 mean monthly ensemble standard deviation (MIV; all shown in Figure 5.22), shows a rather different annual structure than for the MSLP. An annual cycle with maxima in February and minima in August is seen for E1, and a similar but less distinct one with maxima in March and minima in October for E2. This cycle is not present for E3, which has lower SDR magnitudes than the other ensembles due to a very specific annual cycle of MEV. While the mean IV cycle is similar throughout, the MEV displays a somewhat semi-annual dynamic in E1 and E2 but evolves in a cycle similar to the IV in E3. MEV magnitudes are lower in E3 than those in E2 over most of the year and similar to them only in September, when the mean IV in E3 reaches its maximum. Hence, the mean external variability of E3 appears to be affected by IV to a large extent, which results in a SDR permanently below 2, but still above 1.

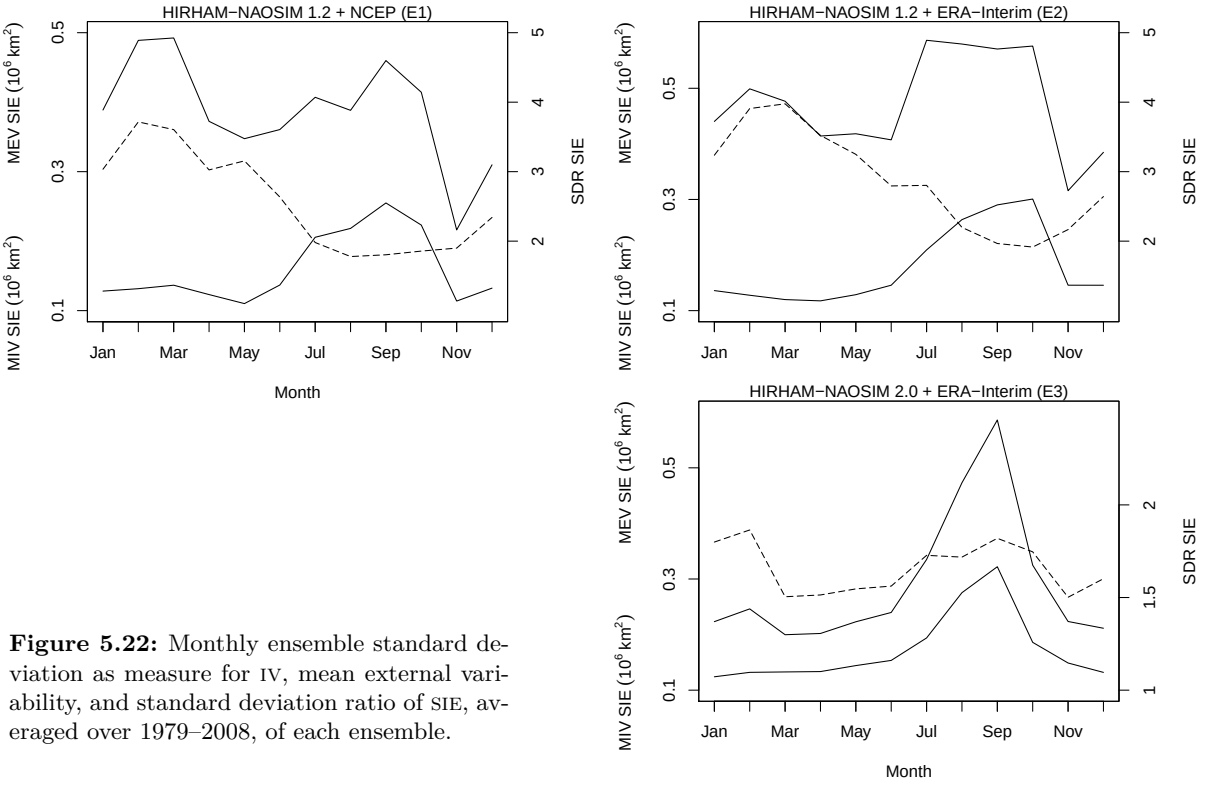

Figure 5.22: Monthly ensemble standard deviation as measure for IV, mean external variability, and standard deviation ratio of SIE, averaged over 1979–2008, of each ensemble.

5.3 Sea ice thickness

Spatially integrated IV of the SIT was measured as rms standard deviation. Since typical distributions of SIT involve maxima near the coasts of Greenland and the Arctic Archipelago as well as minima toward the Atlantic sector (cf. Section 2.3), measuring the anomaly correlation would probably result in only marginal differences even for high-IV cases.

Ensemble size experiments

The 1979–2008 mean rms ensemble standard deviation of six-member ensembles varies within a range of 0.141–0.151 m for sub-ensembles of E2 and within 0.199–0.212 m for sub-ensembles of E3 (Figure 5.23), i. e. at a scale of less than 10 %. The range converges with increasing ensemble sizes. The mean estimated IV of all sub-ensembles of a certain size (red dots) does not depend on the ensemble size.

All these findings match those for MSLP fields (Section 5.1). They differ from those for the SIE (Section 5.2) because they do not exhibit a systematic dependence of IV magnitude on the ensemble size. Consequently, it cannot be decided whether the 10-member ensembles permit a robust estimation.

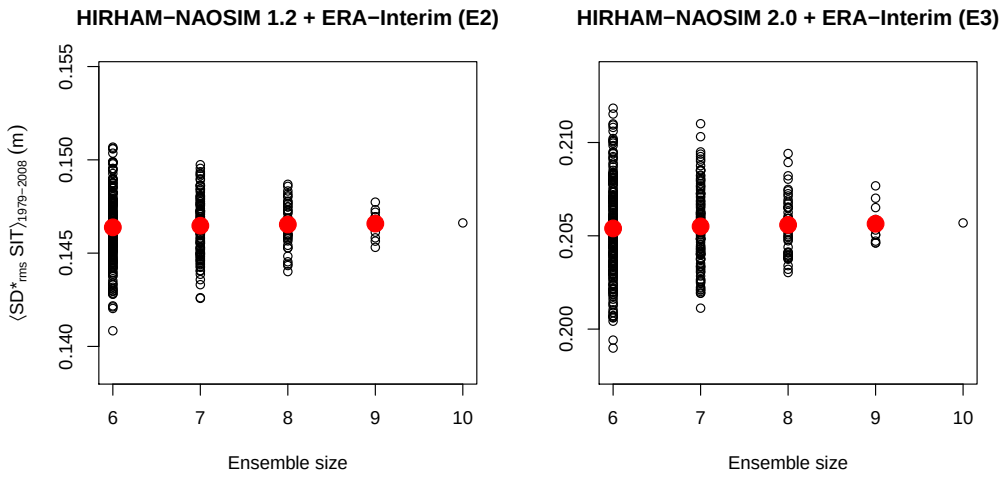

Figure 5.23: Time mean (1979–2008) of the annually averaged rms ensemble standard deviation of SIT for different ensemble sizes. Ensemble sizes of 6–9 use all possible sub-ensembles generated from the respective full ensemble E2 (left) or E3 (right). Red dots denote the mean of all estimates obtained for each ensemble size.

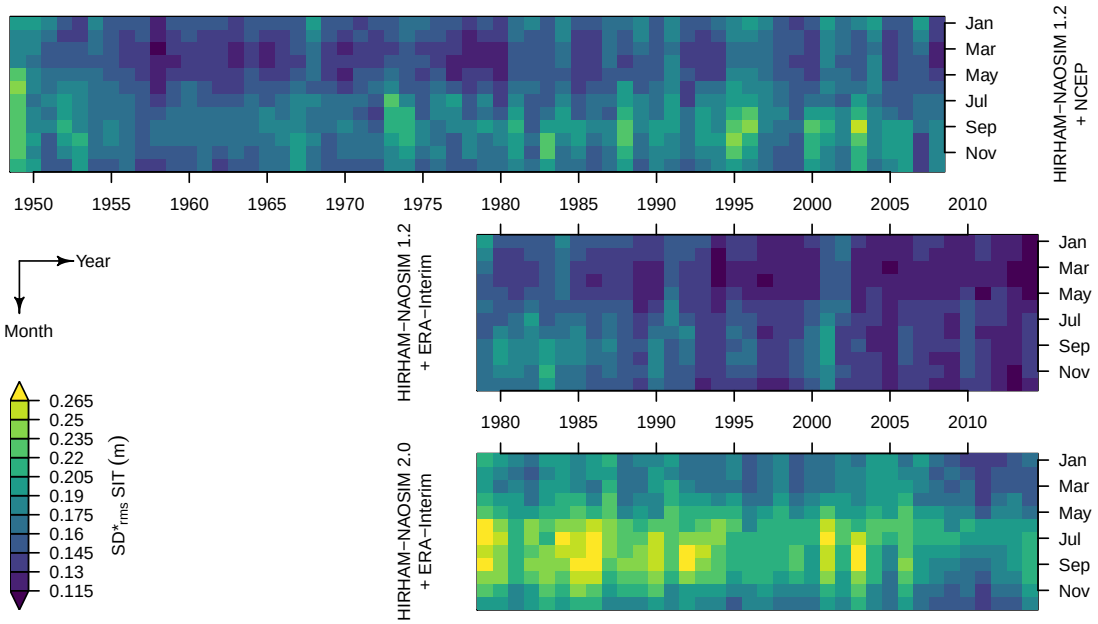

Figure 5.24: Rms ensemble standard deviation of monthly mean sea ice thickness in E1 (top), E2 (middle), and E3 (bottom).

Seasonal and interannual structure

Similar to the SIE, the spatially integrated IV of the monthly mean SIT fields (Figure 5.24) exhibits a seasonal cycle with higher magnitudes in summer/autumn and lower magnitudes in winter/spring. It takes values of 0.114–0.260 m (minimum: March 1958, maximum: September 2003) in E1, 0.101–0.212 m (min.: April 2014, max.: November 1983) in E2, and 0.134–0.279 m (min.: March 2011, max.: August 1992) in E3.

While the seasonal pattern is present throughout the periods of all ensembles, its magnitude undergoes variation from year to year. Common features of this interannual variability can be found mainly in E2 and E3. Both ensembles exhibit roughly simultaneous phases, i. e. high IV in 1979 through the early 1990's, followed by lower IV until 2000, high IV in 2001, and a phase of low IV in 2006–2013. E1, mostly differing from E2 in its interannual structure, involves a noticeably lower mean IV during the period 1954–1972 than in the previous few and the following 36 years.

There are striking differences in domain-wide IV magnitudes between the ensembles, as can be seen from the figure and the ranges given above. Comparing E1 and E2, which differ only in their BCs, the somewhat higher IV in E1 cannot be attributed to the sampling size since the 1979–2008 mean of E1 ($\langle \mathrm{SD}^*_{\mathrm{rms}}\,\mathrm{SIT}\rangle_{1979-2008} = 0.169\,\mathrm{m}$) lies far outside the six-member ranges from the ensemble size experiments of E2 (cf. Figure 5.23,

left). The generally lower IV of E2 must therefore be attributed to the BCs. The E2/E3 comparison, assessing the effect of exchanging the model under the same BCs, shows even larger differences (see 10-member time means in Figure 5.23). As for MSLP (Section 5.1), this effect may be due to the different resolutions, with HIRHAM–NAOSIM 2.0 allowing the solutions to evolve more freely.

Taking into account all these observations, the BCs appears to affect both the interannual variability and magnitudes of IV. The choice of model is an important factor, probably even more important than BCs, determining the overall magnitude of IV. Whether and to what extent BCs or model choice affect the seasonality of IV shall be investigated further.

The distributions of annual minimum- and maximum-IV cases among the months on the one hand (Figure 5.25, right) and the temporal evolution of their positions within the year on the other hand (Figure 5.25, left) show that the seasonal cycle is pronounced and stable for E1 and E2. Minimum IV is found mainly in spring and maximum IV around September. Some months in late autumn / winter (November/December in E1; January in E2) and summer (June/July in E1; June/August/September in E2) appear as cases of both minimum and maximum IV. E3 displays an even stronger seasonality. Minimum- (covering all winter) and maximum-IV months (all summer) are completely separated and distributed narrowly. Compared to E1 and E2, minima and maxima appear earlier in the course of the year.

In summary, the mere change of BCs between E1 and E2—although, as seen, affecting the interannual structure considerably—has virtually no effect on the seasonal cycle. By contrast, changing to the new model version in E3 does not only alter the magnitude of IV but is accompanied by a sharpened and preponed seasonal cycle, as compared to E2.

The seasonality of IV in the SIT fields is likely to be linked to variability of the MSLP fields because the grow of ice thickness due to deformation has one of its causes in the shear forces exercised by the wind field (Serreze and Barry, 2005). The delayed response of maximum IV of SIT compared to the MSLP variability in E1 and E2 could be explained by the accumulation of SIT variations resulting from this effect over the summer. E3, however, has earlier IV maxima in the SIT field, which are closer to the maxima of internal MSLP variability. The higher resolution, enabling more local effects in the simulations, might give rise to stronger thermal feedbacks, which are particularly present during the more radiation-intensive summer months and lead to ice melting.

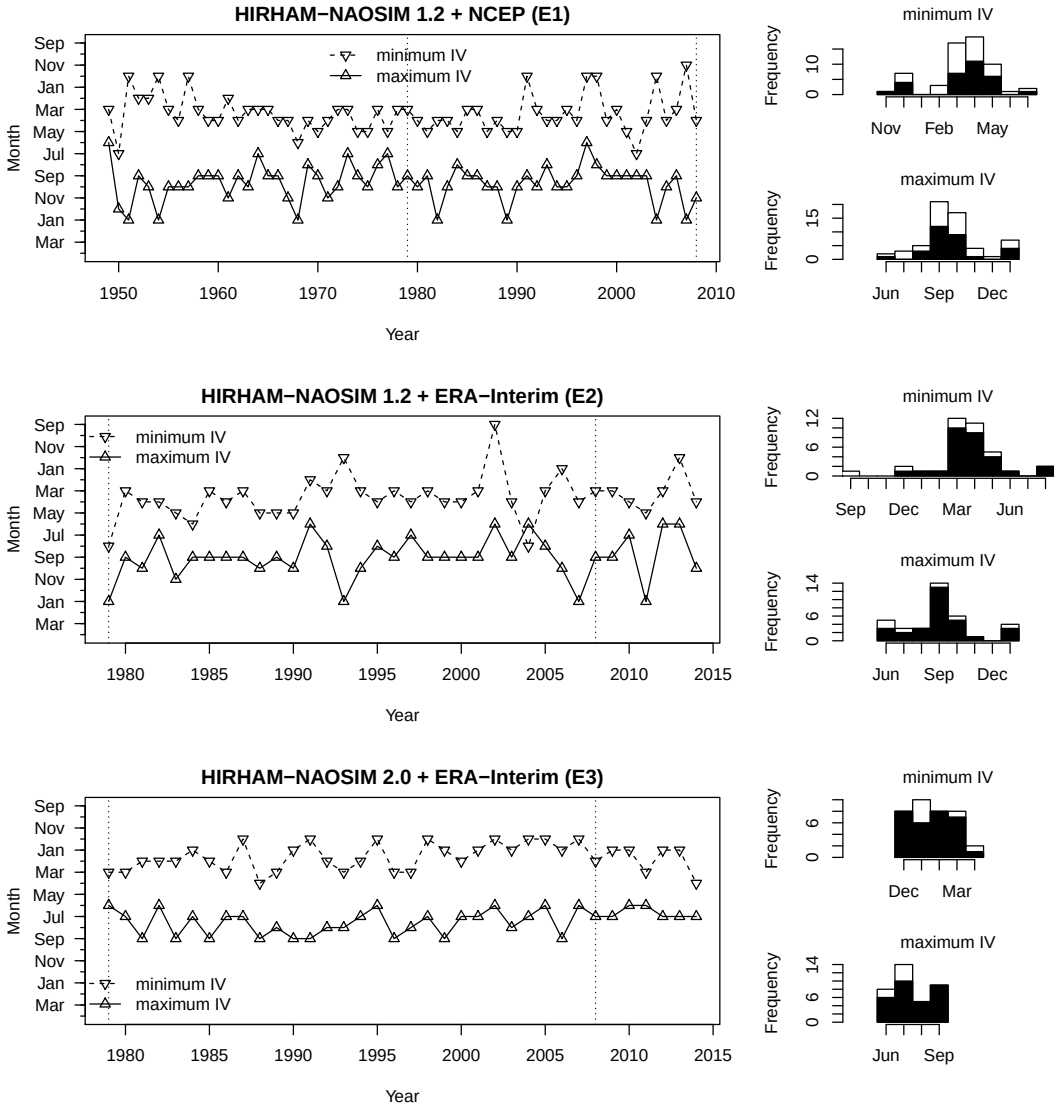

Figure 5.25: As in Figure 5.13 but for SIT.

Spatial structure

To identify typical spatial distributions of IV of the SIT field, example cases are selected. These cases are supposed to firstly represent typical seasons of minimum or maximum IV in each ensemble and secondly distinguish between particularly low or high IV within these seasons.

We follow the same strategy as for MSLP (Section 5.1) and SIE (Section 5.2) for choosing three-month seasons which can be characterized as typical for the occurrence of mini-

Table 5.3: Typical seasons for the occurrence of minimum or maximum IV of SIT and thresholds used to define "low" ($\leq$ 10-% quantile) and "high" ($\geq$ 90 %) IV for the respective three-month season, rounded to the third decimal. Quantiles were taken from 1979–2008 IV data of the respective season.

	E1	E2	E3
typical min-IV months	MAM	MAM	DJF
10-% quantile (in m)	0.132	0.120	0.166
90-% quantile (in m)	0.174	0.157	0.198
typical max-IV months	ASO	ASO	JAS
10-% quantile (in m)	0.160	0.132	0.207
90-% quantile (in m)	0.222	0.188	0.266

mum or maximum IV. Typical minimum-IV months are MAM for E1 (24 occurrences), MAM for E2 (24 occurrences), and DJF for E3 (22 occurrences). Typical maximum-IV months are ASO for E1 (24 occurrences), ASO for E2 (21 occurrences), and JAS for E3 (24 occurrences). Thresholds defining the upper limits for "low" and lower limits for "high" IV are given in Table 5.3. As before, they equal the 10-% and 90-% quantiles and therefore separate 18 cases—nine for high IV, nine for low—from the total of 1979–2008 minimum- / maximum-IV seasons per ensemble.

The example cases, i. e. cases selected based on these thresholds, are now examined as composites: Of all nine cases complying low or high IV conditions in minimum- or maximum-IV seasons, all member SIT fields are averaged (Figure 5.26). Calling to mind the previous sections, the composite analysis of MSLP could credibly be used for identifying comparably strong high- or low-pressure features associated with certain IV conditions, while the SIC/SIE composites suffered from a domination of external variability, resulting from the case selection, over IV. Here, taking the ratio of the domain-averaged sample standard deviation of the ensemble-mean SIT fields (as external) and the composite mean of the domain-averaged ensemble standard deviation fields of SIT (as mean internal variability)—as for SIC/SIE essentially a domain-averaged signal-to-noise ratio (cf. Döscher et al., 2010)—results in values between 0.765 (for high IV in ASO of E1) and 1.604 (for low IV in MAM of E1) for all ensembles. This indicates that domain-wide external and internal variability are of similar magnitudes throughout, a conjecture that will be further pursued in the next subsection. For the present composite analysis, similar contributions of both types of variability allow for, at least, a vague discussion of spatial features.

It is apparent that high-IV cases feature thicker sea ice north of Greenland and the Arctic Archipelago in all composites although not very pronouncedly for the minimum-IV season (DJF) of E3. In fact, these composites exhibit mostly matching SIT fields for

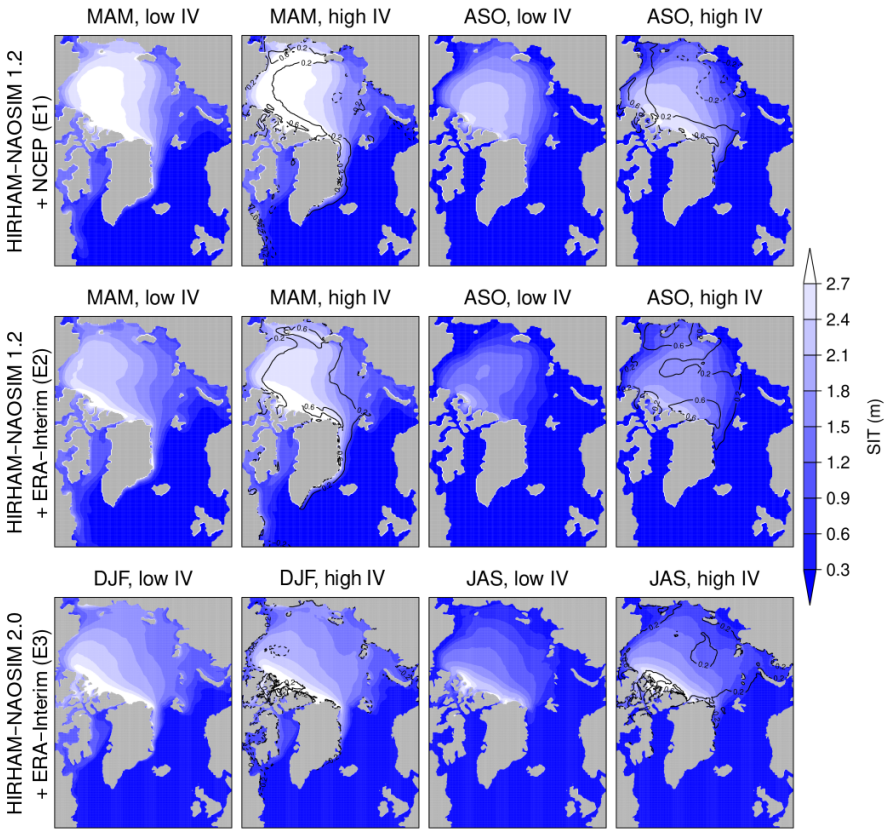

Figure 5.26: SIT composites of low or high IV in the respective minimum- (two left columns) and maximum-IV seasons (two right columns) of E1 (top), E2 (middle), and E3 (bottom). Each composite averages all ensemble members of the nine cases which comply the thresholds given in Table 5.3. Black lines denote contours of difference fields, i. e. high- minus low-IV composite, with solid lines for positive and dashed lines for negative differences.

both low and high IV, but with thinner marginal ice in the high-IV cases. All other comparisons yield mostly thicker ice over large parts of the Arctic Ocean during high IV, with differences of up to 0.7 m as compared to low IV. Exceptions are negative differences spanning the Laptev Sea in the maximum-IV season (ASO) of E1 and practically negligible negative differences in the central Arctic Ocean and marginal zones in the minimum-IV season (MAM) of E1.

We continue with the consideration of single cases, namely the cases of lowest or highest IV in each season of each ensemble, together with the corresponding MSLP fields averaged over the three preceding months. For the minimum-IV season of E1, these cases are April 1980, representing low-IV, and May 2004, representing high-IV (Figure 5.27). SIT fields in April 1980 are characterized by thick ice (thicker than 2.7 m) in an area centered in the Arctic Ocean between the North Pole and the East Siberian / Chukchi / Beaufort Seas. Highest variability between the members can be found along the edges of this area: near the North Pole as well as at the coasts of Eastern Siberia, Canada, and north and east of Greenland. The May 2004 case involves different areas of thick ice, which either span one half of the Arctic Ocean—similar to those in April 1980—, are centered

north of the Arctic Archipelago, or feature a trough of thinner ice, spanning along the line between Svalbard and Alaska. Consequently, IV shows high values in larger areas of north of Greenland and in the Laptev and Barents Seas, additionally to high IV east of Greenland. The preceding MSLP fields show a high-pressure ridge ranging from Siberia toward Canada in April 1980 and a more isolated anticyclonic structure over the Arctic Ocean in May 2004. Qualitatively, they are more variable in May 2004 and unequally allow low pressures to extend from Iceland into the Barents/Kara Seas. Two members featuring very thin ice north of the Barents, Kara, and Laptev Seas show these high-reaching cyclones, which might favor the melting process after March. In April 1980, the mean winds tend to blow from the Greenland and Barents Seas, then in clockwise trajectories over the Arctic Ocean, and could thereby increase the ice thickness in the described area. However, the influence of the preceding MSLP field cannot be too decisive for the SIT, as two members in May 2004 (top right and bottom middle in the figure) with very similar MSLP conditions differ considerably in their SIT distributions.

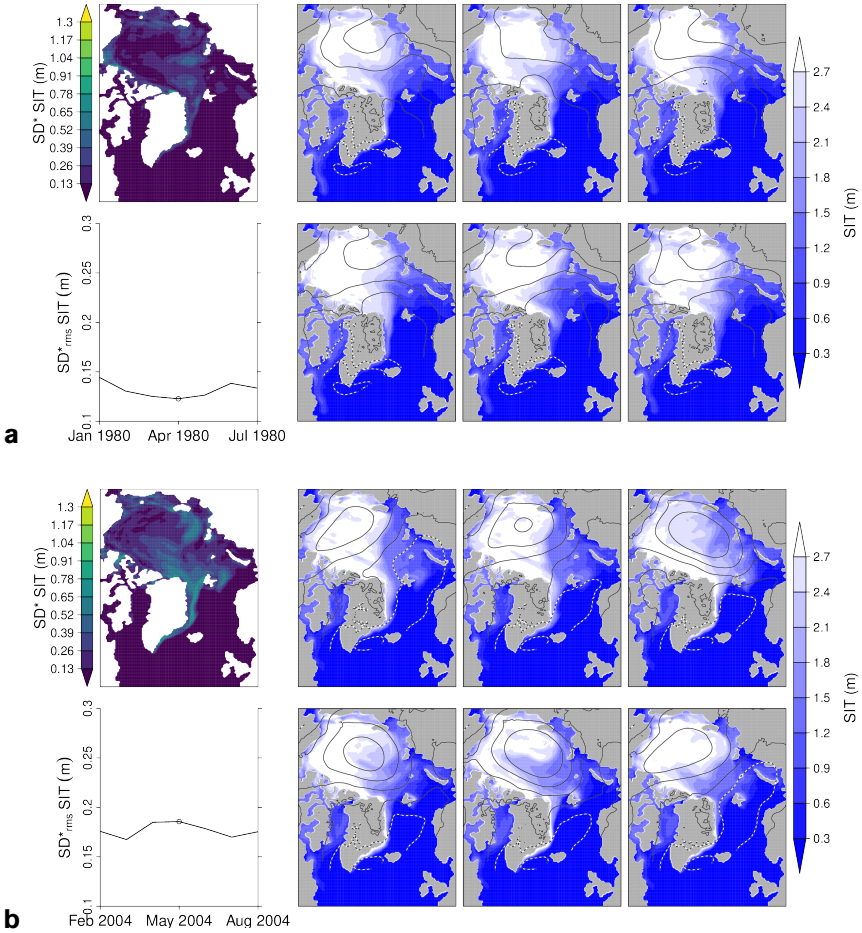

Figure 5.27: SIT fields of all members (all panels except left column of each subfigure), ensemble standard deviation field (top left of each subfigure), and rms ensemble standard deviation (bottom left of each subfigure) for the typically minimum-IV cases April 1980 (**a**, representing low IV) and May 2004 (**b**, representing high IV) of E1.

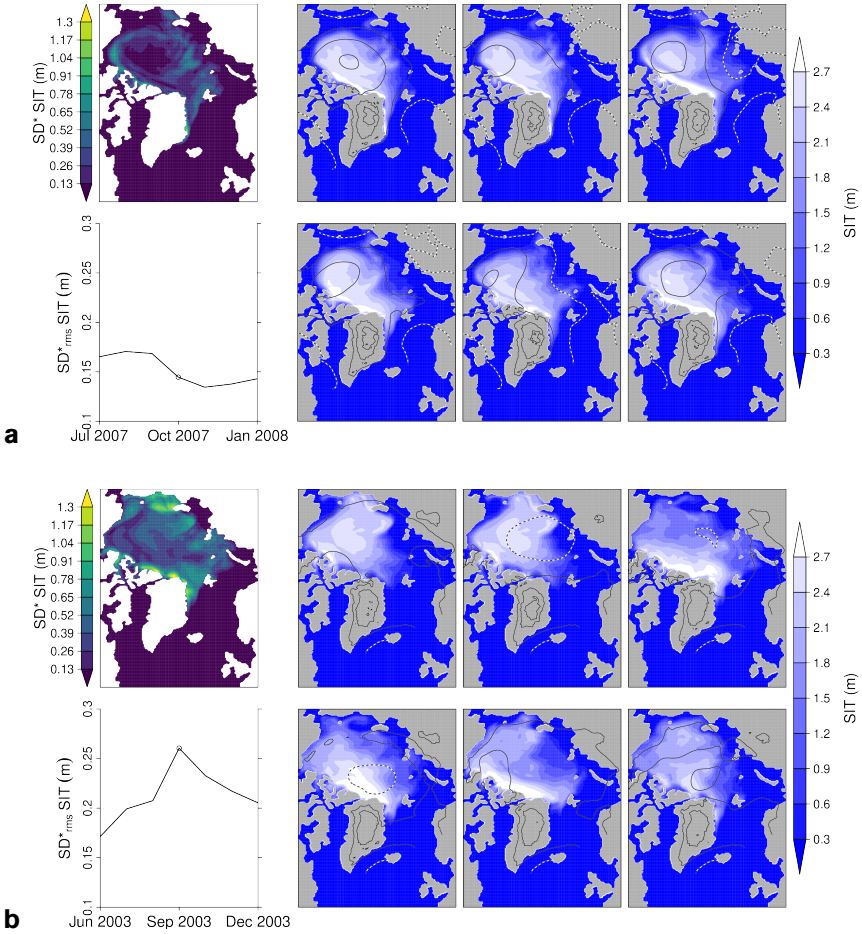

Figure 5.28: As in Figure 5.27 but for the typical maximum-IV cases October 2007 (**a**, low IV) and September 2003 (**b**, high IV) of E1.

The general pattern of larger IV in the marginal areas of the perennial ice zone is also present in the maximum-IV season of E1 (Figure 5.28). The low-IV case of October 2007 shows distributions of thickest sea ice north of Greenland and the Arctic Archipelago and second SIT maxima in the central Arctic Ocean toward the Beaufort Sea. The general MSLP pattern is that of an anticyclone centered roughly over the second SIT maximum. Hence, sea ice convergence due to anticyclonic winds might be a mechanism responsible for the observed distribution. The situation is more complex for the high-IV case of September 2003. Internal variability manifests as two fundamentally different SIT patterns; one with maxima at the coast of the western Arctic Archipelago, reaching toward Eastern Siberia; one with maxima north of Greenland and the Arctic Archipelago. One additional pattern is observed (bottom right panel in the figure), which has two small areas of maxima north of the Arctic Archipelago and shows more evenly distributed SIT over the central Arctic Ocean. The IV is highest in the areas that are virtually ice-free in some member simulations and contain maxima of SIT in others, in particular the northern

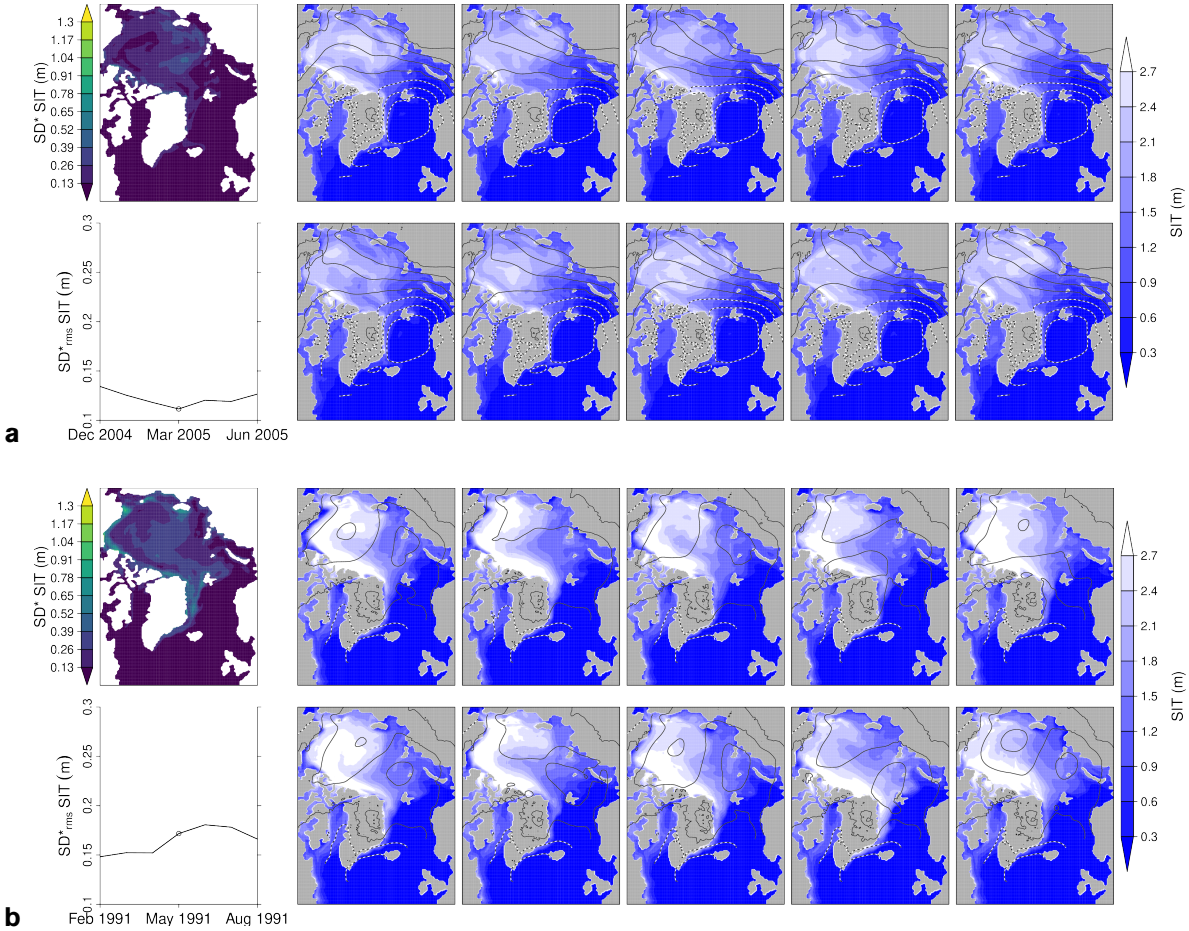

Figure 5.29: As in Figure 5.27 but for the typical minimum-IV cases March 2005 (**a**, low IV) and May 1991 (**b**, high IV) of E2.

Greenland coast and the East Siberian Sea. Averaged preceding MSLP fields have a more or less pronounced cyclonic structure over the Arctic Ocean in three members and rather inexplicit conditions with higher pressures in the other three members. Their direct connection to the SIT fields is not apparent, which might point to the greater influence of short-term and spatially variable phenomenons such as transient cyclones. Merely the location of the small maximum in the last member (bottom right) could be a result of convergence due to the anticyclonic structure centered north of Greenland.

For the minimum-IV season of E2, March 2005 represents low-IV conditions (Figure 5.29a). Maximum SIT is found north of the Arctic Archipelago and a second, mostly isolated area of thick ice lies in the central Arctic Ocean. North of this larger area, near the North Pole, IV has the highest magnitudes apart from some spots of larger IV in the Arctic Archipelago. MSLP fields are quite consistent among the ensemble members

and come with geostrophic winds from the Barents and Kara Seas to Alaska, diverging over the Arctic Ocean. This divergence might be causal for the separation of the two thick-ice areas observed in most members simulations. In the high-IV case of May 1991 (Figure 5.29b), the sea ice is thicker than in March 2005 except for some marginal zones. SIT maxima lie north of Greenland and the Arctic Archipelago, and in the Beaufort, Chukchi, and East Siberian Seas. Maximum IV results from differences in the SIT along the northern Alaskian coast. The contrast between thicker ice in the East Siberian Sea and thinner ice in the Laptev, Kara, and Barents Seas coincides with a pressure ridge, in some members developed into an anticyclonic structure, over the East Siberian Sea or East Siberian and Laptev Seas on the one hand and with another relatively low-pressure, cyclonic structure over the Kara / Barents Seas on the other hand. Both mechanisms, ice divergence due to a cyclone and ice convergence due to an anticyclone, may be reasons for the distribution. However, it is not possible to clearly associate features of the intra-ensemble SIT variability, including the IV maxima north of Alaska, to the MSLP.

August 2004 as a low-IV case in the maximum-IV season of E2 (Figure 5.30a) involves thickest ice north of the Arctic Archipelago and further smaller maxima in the central Arctic Ocean and the East Siberian / Laptev Seas, depending on the member. IV is highest along the sea ice margins but has a low overall magnitude. MSLP conditions are variable but all members show a weak anticyclonic structure over the Arctic Ocean. The high-IV case of September 2001 (Figure 5.30b) features very variable SIT patterns with maxima north of Greenland and the Arctic Archipelago as well as the East Siberian / Laptev Seas. These are also areas of maximum IV, which is again generally high near the sea ice margins and low in the central Arctic Ocean. No clear connection exists between the highly variable atmospheric circulation and the SIT fields except for a tendency toward more radially symmetric SIT patterns following pronounced cyclonic conditions (panels 1, 3, and 5, in the upper row of Subfigure b).

For E3, January 1996 and December 1983 represent low- and high-IV cases in the minimum-IV season (Figure 5.31). The former case features large SIT north of Greenland through the Beaufort Sea. IV is distributed very evenly over the domain but is comparably high in a narrow area along the northern coast of Greenland and the northeastern coast of the Arctic Archipelago. Conditions are similar in December 1983 but with thinner ice in the Beaufort Sea, thicker ice in the East Siberian and Chukchi Seas, and higher IV in the marginal areas of the SIT field. The MSLP fields in both cases are characterized by pressure ridges or anticyclones over the Beaufort and East Siberian Seas, sometimes extending toward the central Arctic Ocean and sometimes narrowed by pronounced low-pressure systems with their centers located over the Barents / Kara Seas.

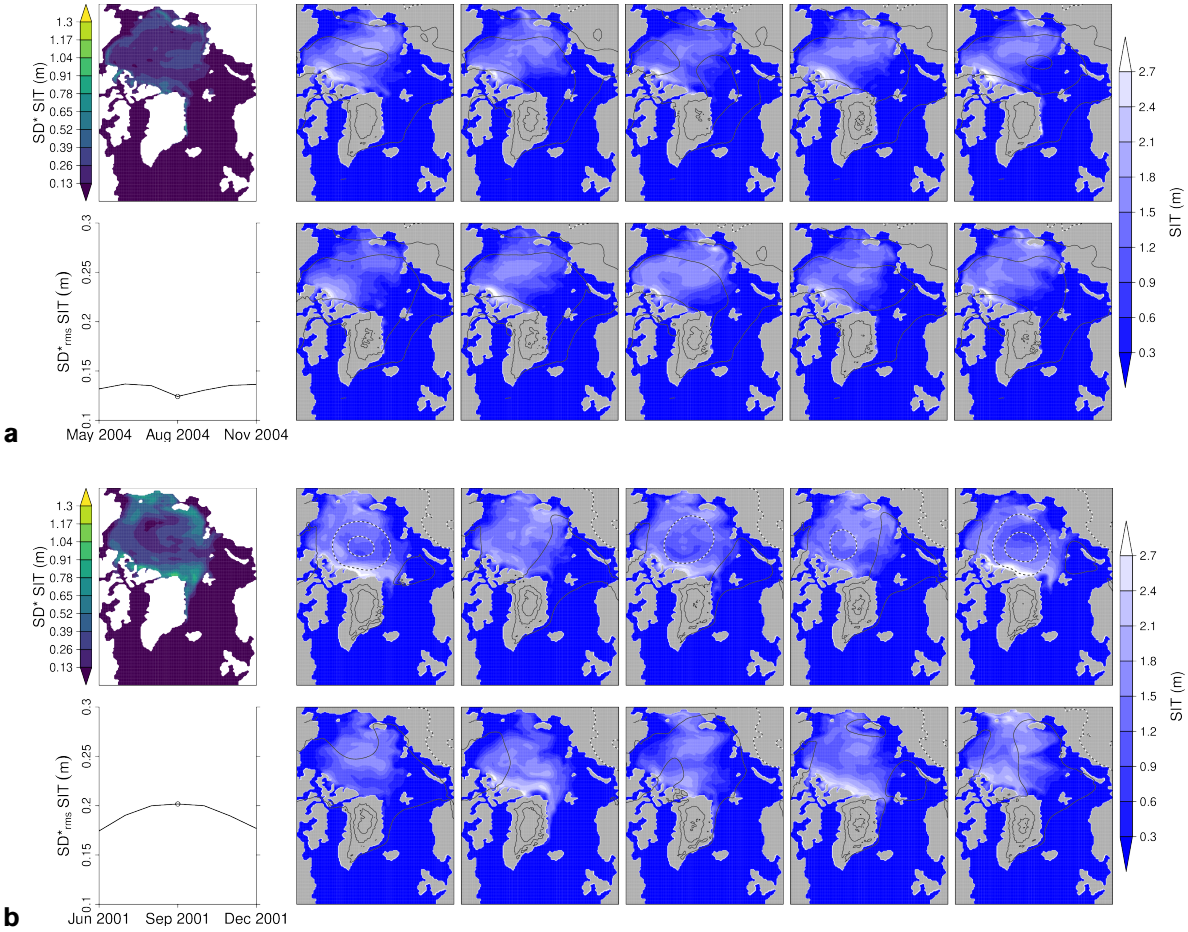

Figure 5.30: As in Figure 5.27 but for the typical maximum-IV cases August 2004 (**a**, low IV) and September 2001 (**b**, high IV) of E2.

This pattern probably comes with a strong Transpolar Drift Stream due to geostrophic winds and could be a reason for reduced SIT north of the Laptev Sea in some members. Yet again, however, attributions of specific intra-ensemble differences in the SIT fields to variability in the MSLP fields are not found.

In September 2005, the example case of low IV conditions in the maximum-IV season of E3 (Figure 5.32a), SIT shows the typical maxima north of Greenland and the Arctic Archipelago. These are the same areas where the IV is maximal. Medium magnitudes of IV are located in the marginal areas of sea ice, opposed to low IV in the more central parts. MSLP has weak but variable structures without a clear connection to the SIT fields. In the corresponding high-IV case of August 1992 (Figure 5.32b), the maxima north of Greenland and the Arctic Archipelago are present but with variable locations, leaving large parts of the coastal areas almost ice-free in some members. The IV consequently

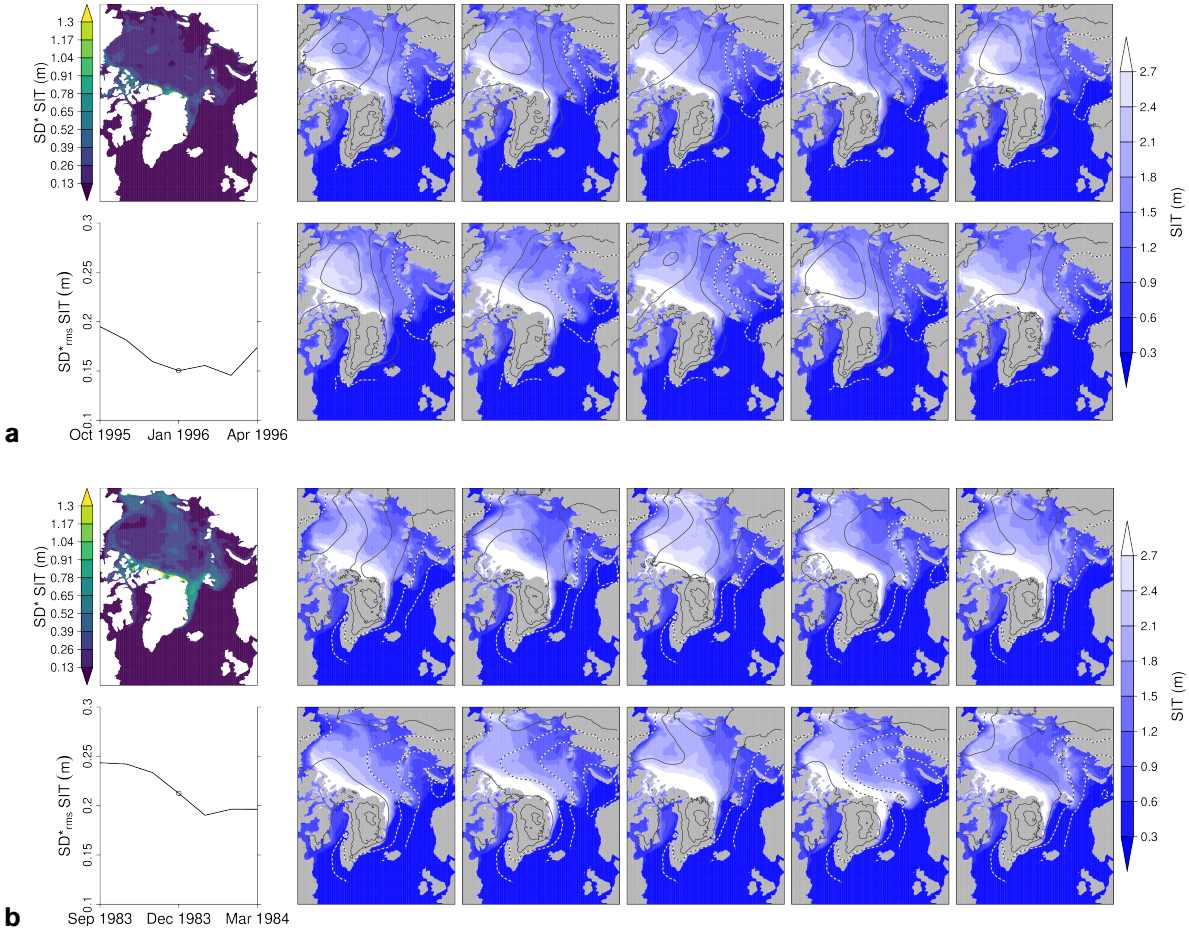

Figure 5.31: As in Figure 5.27 but for the typical minimum-IV cases January 1996 (**a**, low IV) and December 1983 (**b**, high IV) of E3.

reaches particularly high magnitudes there but is also comparably high in most parts of the Arctic Ocean. Most members develop an additional local maximum of SIT north of the Beaufort and Chukchi Seas, which is centered dependent on the location of the cyclone as part of a dipole structure present in all MSLP fields of this case. Higher-reaching cyclones tend to shift the center of this maximum toward the Alaskian coast.

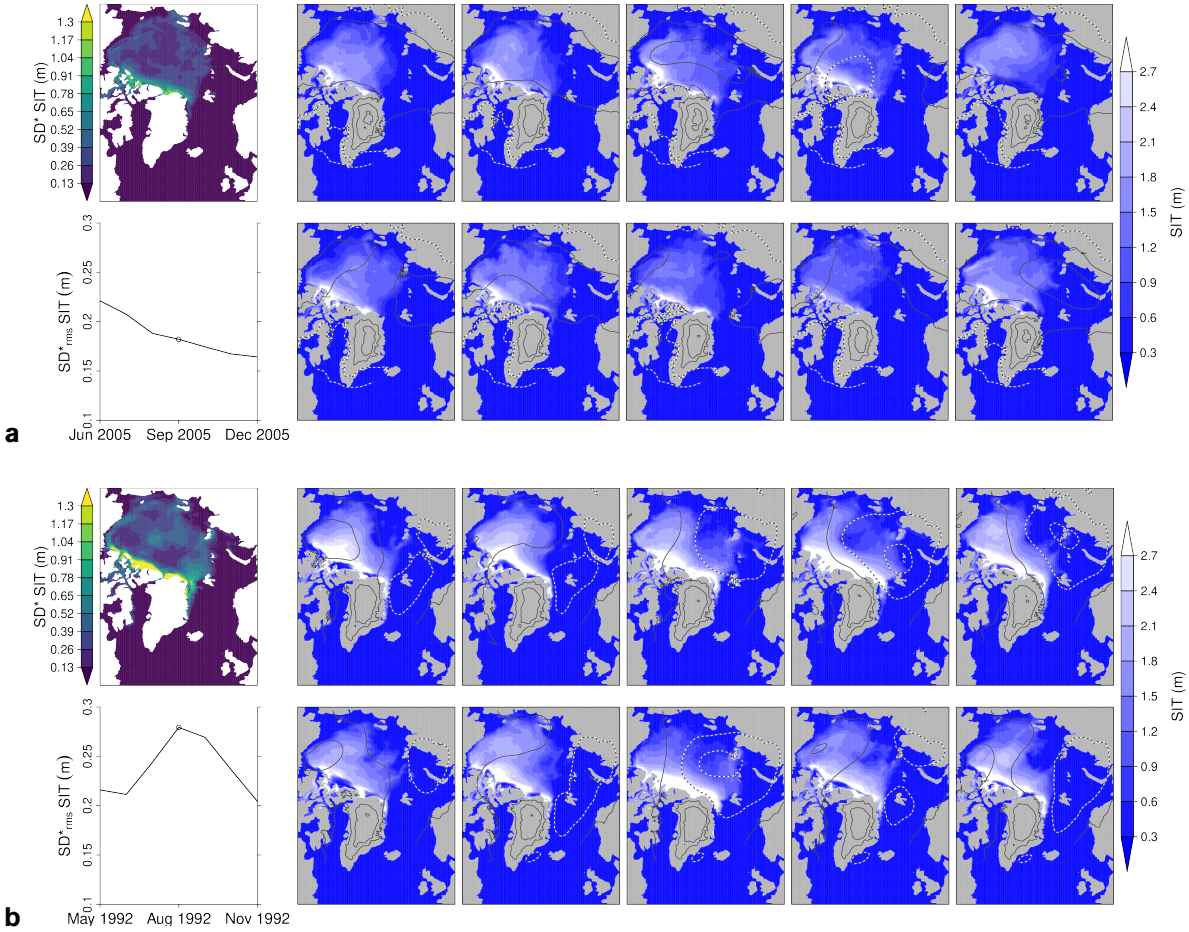

Figure 5.32: As in Figure 5.27 but for the typical maximum-IV cases September 2005 (**a**, low IV) and August 1992 (**b**, high IV) of E3.

Ratios of external and internal variability

As a measure for the dominance of external variability, induced mainly by the boundary forcing, over the IV, we use the standard deviation ratio (SDR) just like in the cases of MSLP (Section 5.1) and, in adapted form, of SIE (Section 5.2). Along with the SIE, Dorn et al. (2012) calculated the monthly SDR of the SIT, averaged over 1948–2008, and found a very weak annual cycle thereof (Figure 4 there). The results herein, obtained for the period 1979–2008 of all ensembles (Figure 5.33, dashed lines), show the same annual cycle with maxima in spring and minima in autumn. Values constantly lie between 1 and 2, which indicates an overall dominance of external variability but allows IV to influence the model behavior considerably. Using the same model version and BCs as in Dorn et al. (2012), E1 shows smaller SDR magnitudes for the 1978–2008 averaging (top

left panel) as compared to the period 1948–2008 (Dorn et al., 2012). This indicates a larger effect of IV in 1979–2008 and corresponds to the fact that the averaging of Dorn et al. (2012) includes the 1954–1972 period of lower IV, which was seen in Figure 5.24 and mentioned in the subsection *Seasonal and interannual structure*. Although having a similar annual cycle in Ensembles 1, 2, and 3, magnitudes of the SDR differ between the ensembles; E2 has the highest, E3 the lowest. This can easily be explained by the large differences in domain-averaged IV magnitudes, as was already discussed in the beginning of this section and can be seen when looking on the lower solid lines in each panel of Figure 5.33. Yet the upper solid lines, denoting the domain-mean mean external variability (MEV), show different annual courses—a rather inexplicit dynamic in E1, a pronounced cycle including a June maximum and a September minimum in E2, and a pronounced maximum in June. Comparing these lines with the intra-annual courses of the mean internal variability (lower solid lines), it is likely that the MEV dynamics are composed of purely BC-driven variability with maxima in June and the IV specific for each ensemble.

With the aid of the mean locking time fraction (MLTF) of the SIT, mapped for the typical minimum- and maximum-IV seasons of each ensemble (Figure 5.34), it is possible

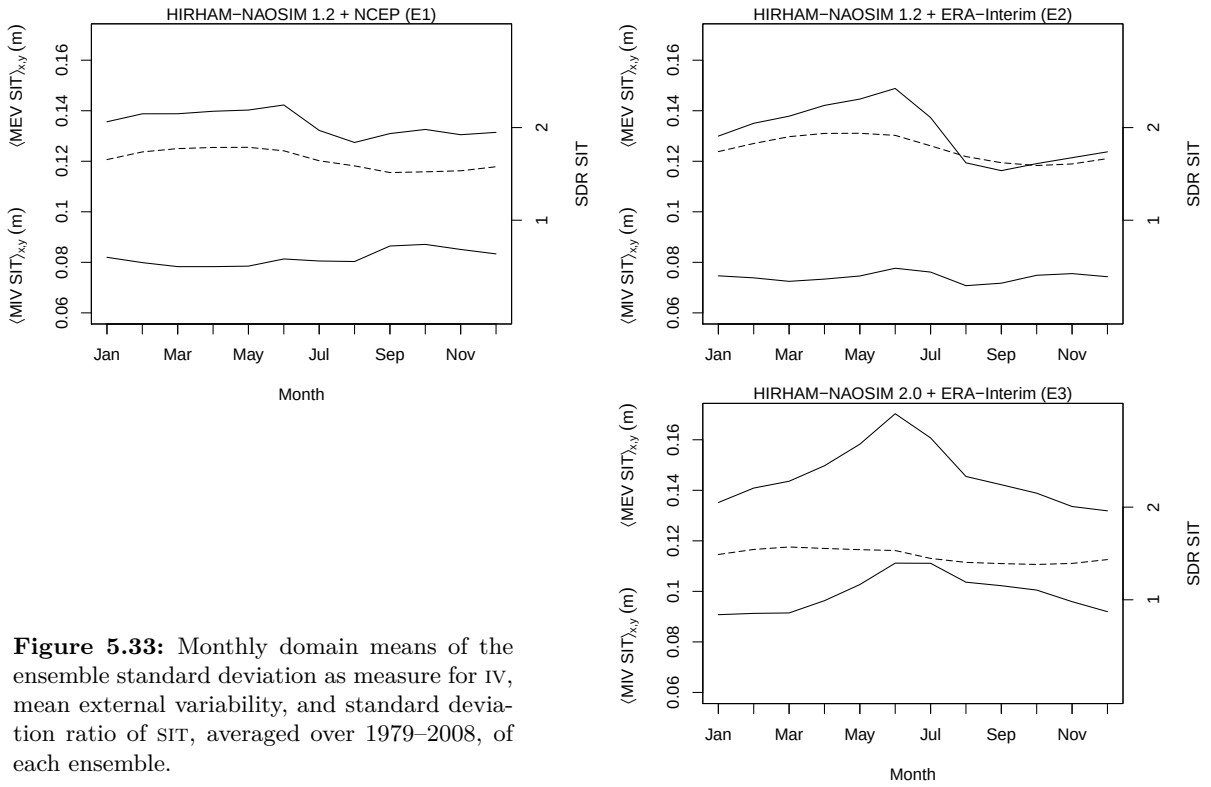

Figure 5.33: Monthly domain means of the ensemble standard deviation as measure for IV, mean external variability, and standard deviation ratio of SIT, averaged over 1979–2008, of each ensemble.

to estimate possibilities for the MEV exceeding the IV at each grid point. In E1, IV dominates in more than 2 out of 10 cases (i. e. MLTFSIT < 0.8) in large parts of the central Arctic Ocean, occasionally along the eastern Greenland coast, and between the islands of the Arctic Archipelago, both in the minimum- and the maximum-IV season. During the maximum-IV season (ASO), the dominance of IV is somewhat larger across the Arctic Ocean than during the minimum-IV season (MAM). In E2 and E3, these areas are more sparsely distributed and roughly span the Laptev, Kara, Barents, and Greenland Seas as well as the Arctic Archipelago in minimum- and maximum-IV seasons. The maximum-IV seasons are generally characterized by a larger dominance of IV along the Arctic coasts. Extremely low values of the MLTF are found in the Arctic Archipelago for the minimum-IV season of E1 (0.21), for the minimum-IV season of E3 (0.12), and for the maximum-IV season of E3 (0.11).

These results indicate a substantial influence of IV on interpreting climate signals in some areas of the modeled SIT fields. Even though the external variability is exceeded only occasionally there, the IV was shown to likely have an impact on the annual cycle of the external variability, measured as the ensemble-mean standard deviation of the member time series.

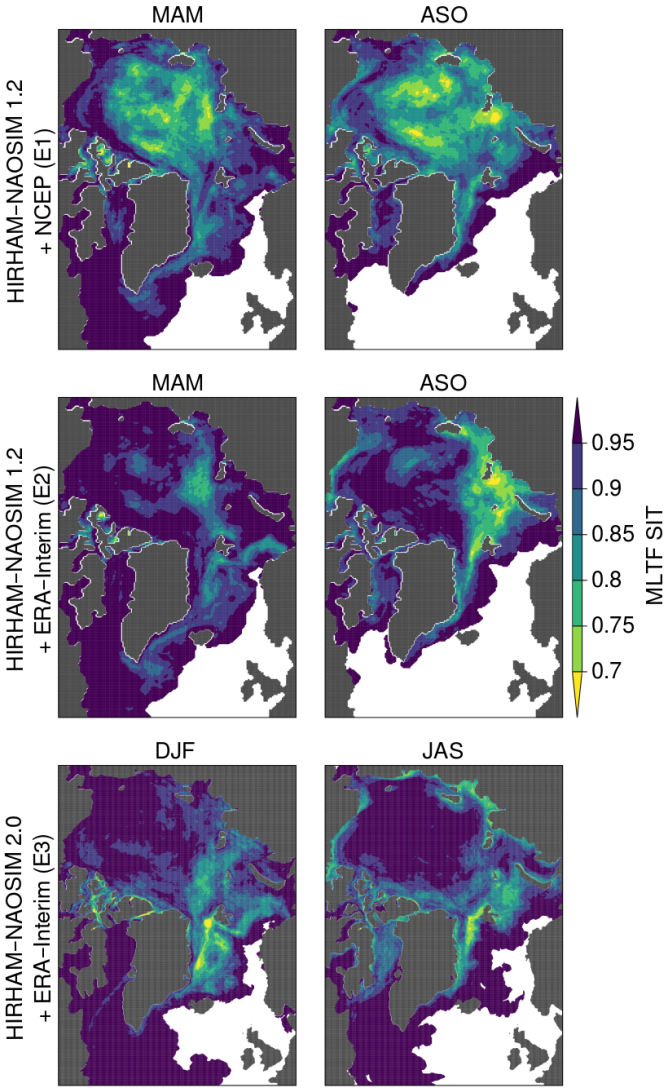

Figure 5.34: Mean locking time fraction with locking defined as the IV being smaller than the MEV ($\epsilon = 1$) of SIT fields of the typical minimum-IV (left) and typical maximum-IV seasons (right), averaged over 1979–2008.

6 SUMMARY AND CONCLUSION

Several aspects of the IV extant in the coupled Arctic regional climate model HIRHAM–NAOSIM were investigated in the preceding chapter. Therefore, we used three ensembles, consisting of an old model version driven at the boundaries by NCEP reanalysis data (E1), the same model version driven by ERA-Interim data (E2), and a newer model version also driven by ERA-Interim data (E3). For the variables mean sea level pressure (MSLP), sea ice extent (SIE), and sea ice thickness (SIT), the estimation by means of the 10-member ensembles E2 and E3 could neither be characterized as robust nor as non-robust. IV estimations using multiple smaller sub-ensembles of E2 and E3 show increasing scattering with descreasing sub-ensemble size and tend to vary more strongly for E3 than E2. These experiments suggest that the sampling effect on six-member ensembles is very low in the case of anomaly correlations of the MSLP fields (variations in the scale of 1 %), quite high for the ensemble standard deviation of SIE ($\sim 20\,\%$), and medium for the rms ensemble standard deviation of SIT ($\sim 10\,\%$).

Although measured differently, the IV exhibits an annual cycle of seasonality with maxima in the summer and early autumn months as well as minima in winter and spring for all variables. Possible reasons for this seasonality are a weaker atmospheric circulation and increased thermal processes and instabilities due to the presence of solar radiation during summer. The timing of this annual cycle differs between the variables and among the different ensembles. MSLP exhibits the earliest maxima, lying in the mid-summer season, and the earliest minima, distributed mainly among the winter months. SIT and SIE follow with maxima of IV located prominently in late summer / early autumn. Minima of the IV of both variables are observed in winter and spring, whereby those for the SIE are distributed very broadly. The delay of the annual IV cycle of the sea ice variables against that of the atmospheric IV can be explained by the accumulation of atmospheric effects on the sea ice movement and melting during summer.

The newer model version in E3 almost exclusively results in earlier maxima and minima of the IV of SIE and SIT as compared to E2. It also features somewhat earlier SIE minima, which might be related to the IV maxima of the SIE. Additionally, the choice of the

model version affects the magnitude and interannual structure of IV of the MSLP fields and the magnitude of IV of the SIT fields. Differences in the boundary forcing, as seen by comparison between E1 and E2, result in different interannual structures and, to a smaller degree than the model choice, the overall magnitude of IV of all variables.

Systematic investigations of the spatial peculiarities in the atmospheric and ice fields associated with especially low- or high-IV conditions in typical minimum- or maximum-IV seasons were meaningful only for the MSLP and the SIT. In the former case, the most prominent feature is a higher-reaching Aleutian Low, extending into Alaska, as well as weaker high-pressure areas over Siberia and Canada when IV is very high in the minimum-IV seasons, i. e. the cold period of the year. This characteristic might be associated with increased frequencies of cyclones over this part of the Arctic, which can increase the monthly IV due to their transient nature. For the SIT, the composite analysis combines cases of similar external and internal variability, thus reducing the clarity of the results. Still, sea ice tends to be thicker in most composites of high IV as compared to the respective low-IV composites.

Multiple example cases were discussed. While the features seen in the composite analyses were present in some cases, the overall picture is rather that of various conditions leading to low or high IV through different processes, often physically justifiable using the few data at hand. The same holds for the effect of preceding three-month averaged MSLP fields on the variability of sea ice variables. E. g. the hypothesis of an increased sea ice import and southerly winds passing through Fram Strait as mechanism for high IV of the summerly SIE (Döscher et al., 2010) could be confirmed only very limitedly for one ensemble.

Assessments of the ratio of external to internal variability yielded the findings that predictability usually decreases during summer or autumn but the variability induced by the forcing generally dominates the domain-wide climatology. Yet, the probability of IV exceeding the external variability can be quite large for MSLP in the central domain during the summer season and for SIT in large parts of the Arctic Ocean and its marginal seas during both minimum- and maximum-IV seasons.

We thereby confirm that internal variability is a factor that needs to be taken into account when evaluating results of regional climate models and claim that it can provide insight into climate-related physical processes and their stability properties.

Appendix

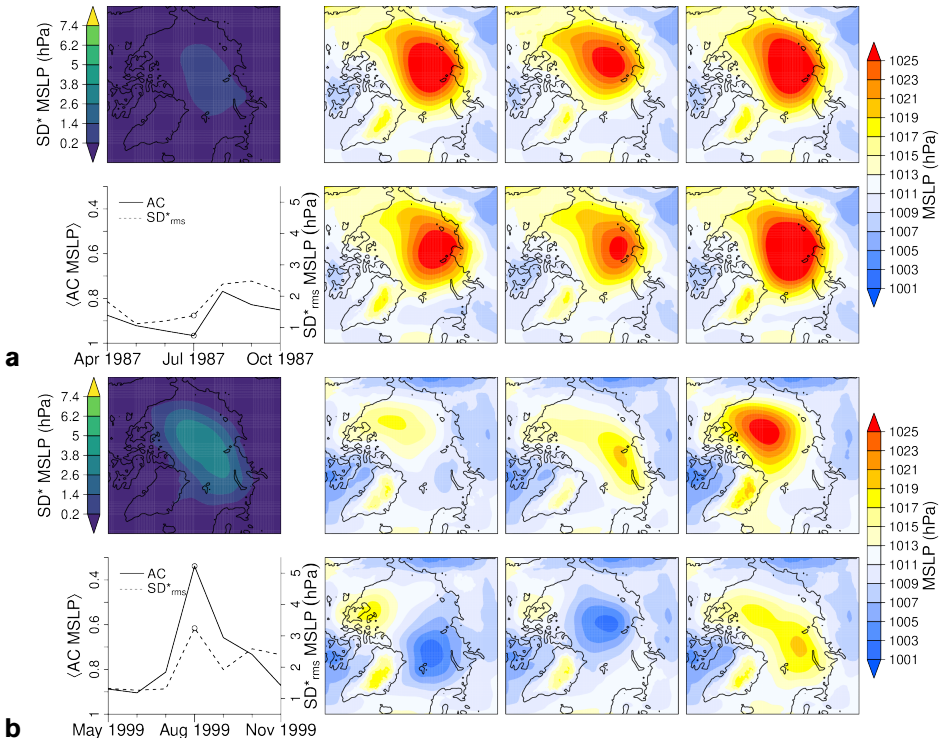

Figure A.1: As in Figure 5.5 but for the typically maximum-IV cases July 1987 (**a**, low IV) and August 1999 (**b**, representing high IV) of E1.

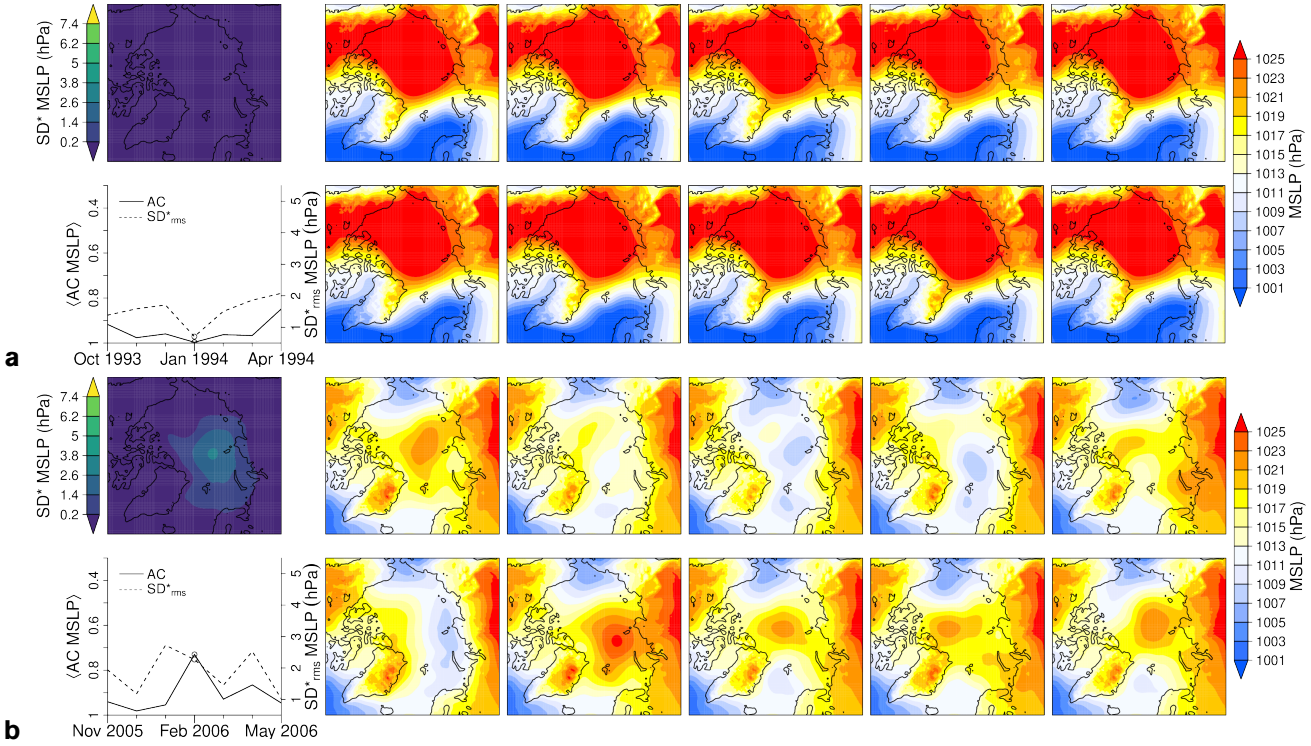

Figure A.2: As in Figure 5.5 but for the typically minimum-IV cases January 1994 (**a**, low IV) and February 2006 (**b**, high IV) of E2.

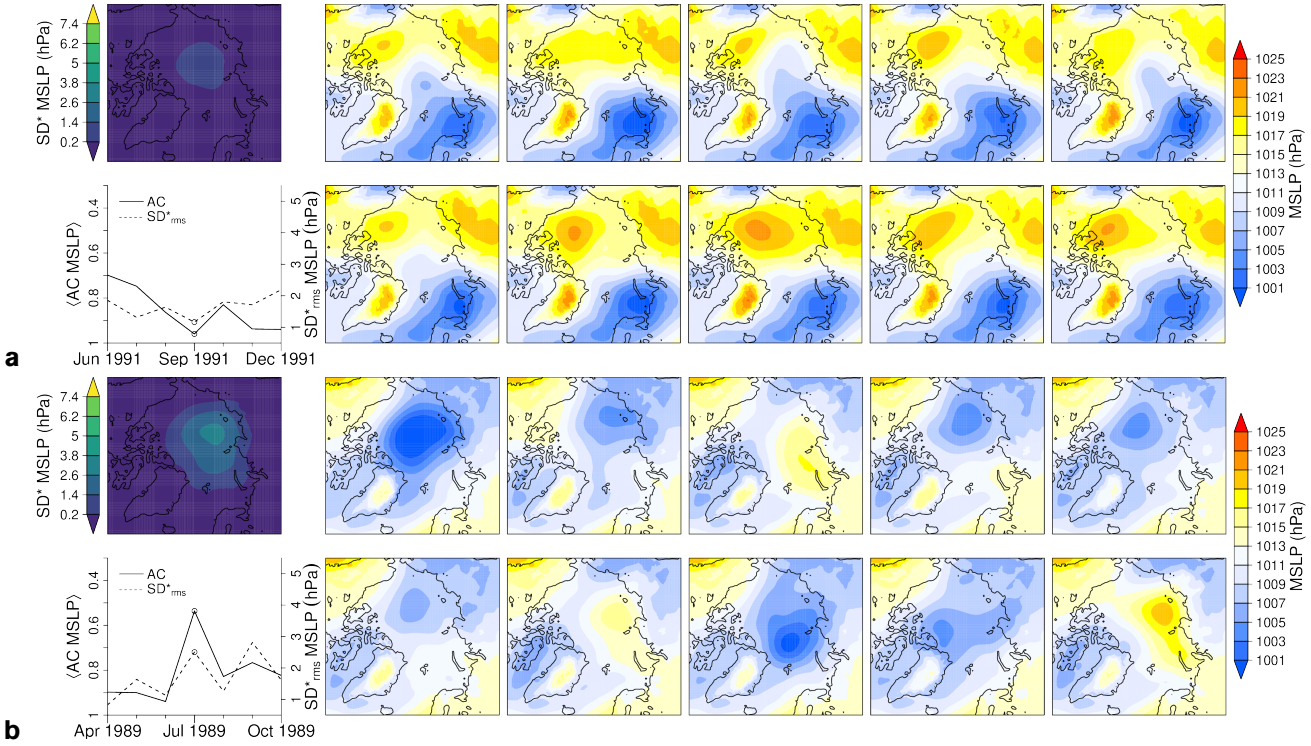

Figure A.3: As in Figure 5.5 but for the typically maximum-IV cases September 1991 (**a**, low IV) and July 1989 (**b**, high IV) of E2.

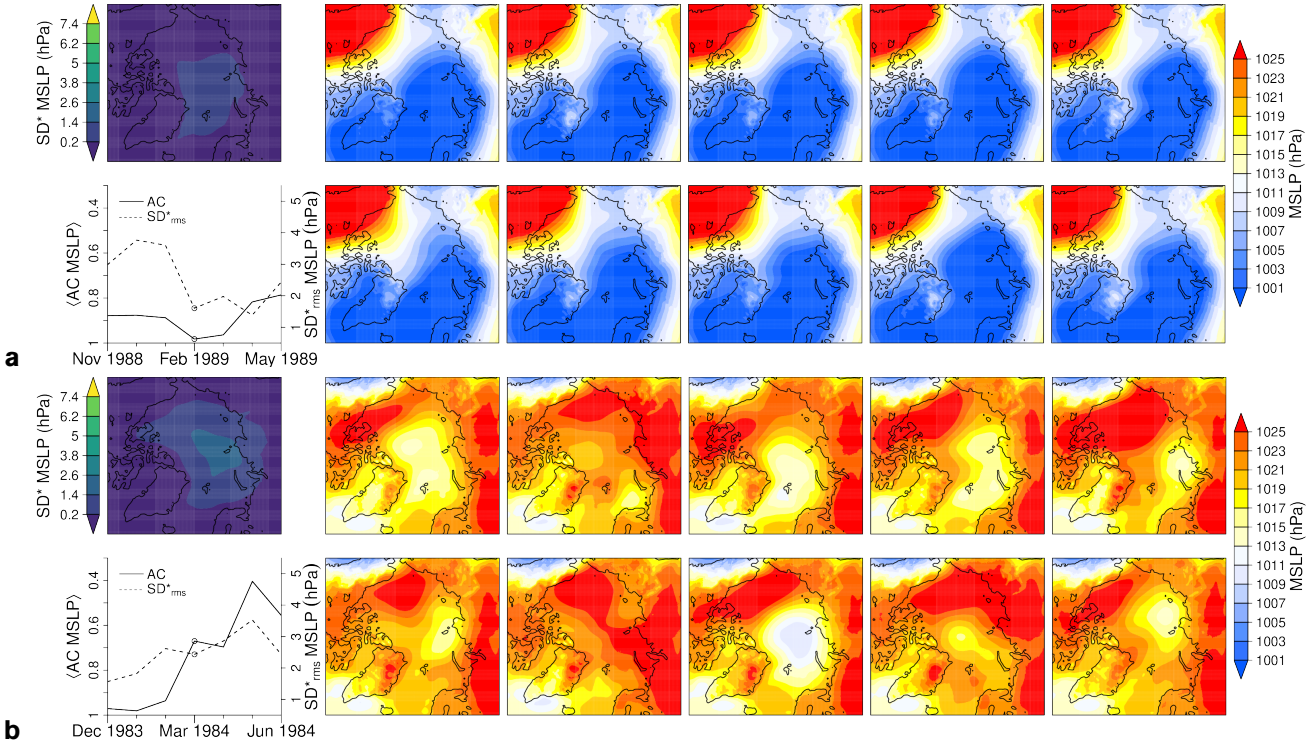

Figure A.4: As in Figure 5.5 but for the typically minimum-IV cases February 1989 (**a**, low IV) and March 1984 (**b**, high IV) of E3.

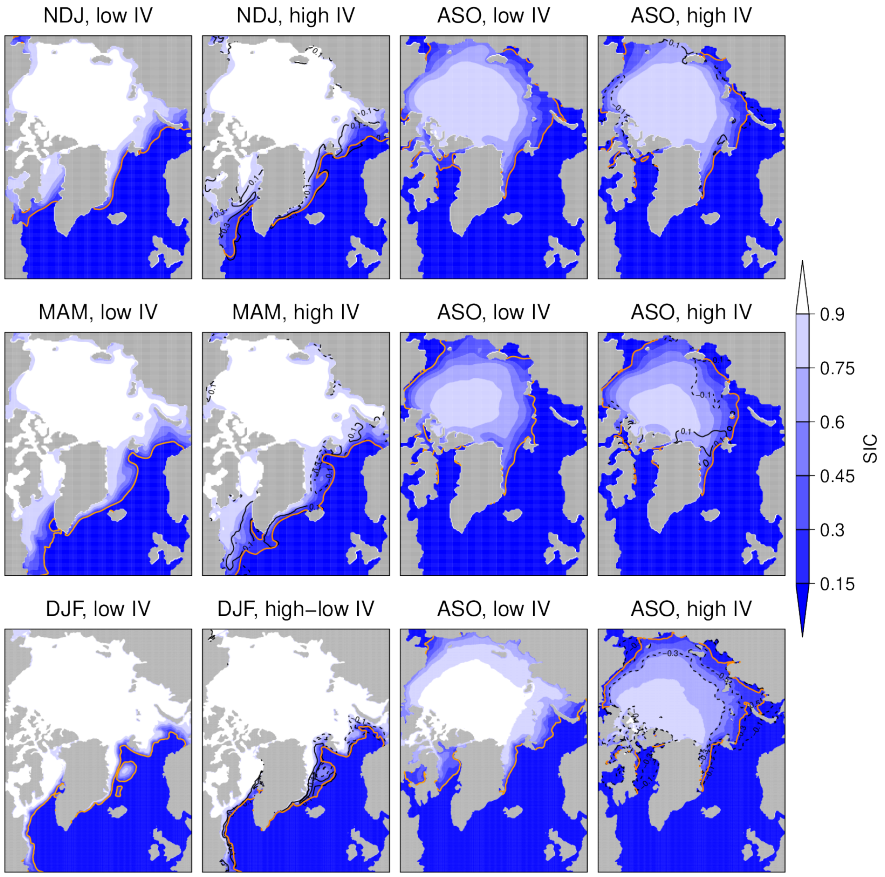

Figure A.5: SIC composites of low or high IV in the respective minimum- (two left columns) and maximum-IV seasons (two right columns) of E1 (top), E2 (middle), and E3 (bottom). Each composite averages all ensemble members of the nine cases which comply the thresholds given in Table 5.2. Black lines denote contours of difference fields, i. e. high- minus low-IV composite, with solid lines for positive and dashed lines for negative differences.

Note of Thanks

I very much thank the people who provided the necessary help—wittingly or unwittingly—for writing this thesis:

The Atmospheric Physics Group at the Alfred Wegener Institute in Potsdam, 4138 km south the North Pole; especially Annette for the tea, topic, literature, data, constant interest, and always motivating discussions; Xiaoyong for good neighborhood, tips, and data; Wolfgang for CDO-related help, discussions, and information regarding the model; Sabine for computer help.

Wera for covered time and distances; Jegor for the pleasant company on long walks for thinking and reading; most importantly, Sophia for time, food, opinions, and sympathy.

Bibliography

Alexandru, A., R. de Elia, and R. Laprise

2007. Internal variability in regional climate downscaling at the seasonal scale. *Monthly Weather Review*, 135:3221–3238.

Anthes, R.

1986. The general question of predictability. In *Mesoscale meteorology and forecasting*, P. Ray, ed., Pp. 636–656. American Meteorological Society, Boston.

Anthes, R., Y.-H. Kuo, D. Baumhefner, R. Errico, and T. Bettge

1985. Predictability of mesoscale atmospheric motions. *Advances in Geophysics*, 28, Part B:159–202.

Caya, D. and S. Biner

2004. Internal variability of RCM simulations over an annual cycle. *Climate Dynamics*, 22:33–46.

Christensen, J. and E. van Meijgaard

1992. On the construction of a regional atmospheric climate model. Technical report, Danmarks Meteorologiske Institut.

Christensen, O., M. Gaertner, J. Prego, and J. Polcher

2001. Internal variability of regional climate models. *Climate Dynamics*, 17:875–887.

Crétat, J. and B. Pohl

2012. How physical parameterizations can modulate internal varibility in a regional climate model. *Journal of the Atmospheric Sciences*, 69:714–724.

Dee, D., S. Uppala, A. Simmons, P. Berrisford, P. Poli, S. Kobayashi, U. Andrae, M. Balmaseda, G. Balsamo, P. Bauer, P. Bechtold, A. Beljaars, L. van de Berg, J. Bidlot, N. Bormann, C. Delsol, R. Dragani, M. Fuentes, A. Geer, L. Haimberger, S. Healy, H. Hersbach, E. Hólm, L. Isaksen, P. Kållberg, M. Köhler, M. Matricardi, A. McNally,

B. Monge-Sanz, J.-J. Morcrette, B.-K. Park, C. Peubey, P. de Rosnay, C. Tavolato, J.-N. Thépaut, and F. Vitart
2011. The ERA–interim reanalysis: configuration and performance of the data assimilation system. *Quarterly Journal of the Royal Meteorological Society*, 137:553–597.

Diaconescu, E., R. Laprise, and A. Zadra
2012. Singular vector decomposition of the internal variability of the Canadian regional climate. *Climate Dynamics*, 38(5–6):1093–1113.

Dorn, W., K. Dethloff, and A. Rinke
2009. Improved simulation of feedbacks between atmosphere and sea ice over the Arctic Ocean in a coupled regional climate model. *Ocean Modelling*, 29:103–114.

Dorn, W., K. Dethloff, and A. Rinke
2012. Limitations of a coupled regional climate model in the reproduction of the observed Arctic sea-ice retreat. *The Cryosphere*, 6:985–998.

Dorn, W., K. Dethloff, A. Rinke, S. Frickenhaus, R. Gerdes, M. Karcher, and F. Kauker
2007. Sensitivities and uncertainties in a coupled regional atmosphere–ocean–ice model with respect to the simulation of Arctic sea ice. *Journal of Geophysical Research*, 112(D10118).

Döscher, R., K. Wyser, H. Meier, M. Qian, and R. Redler
2010. Quantifying Arctic contributions to climate predictability in a regional coupled ocean–ice–atmosphere model. *Climate Dynamics*, 34:1157–1176.

Fieg, K., R. Gerdes, E. Fahrbach, A. Beszczynska-Möller, and U. Schauer
2010. Simulation of oceanic volume transports through Fram Strait 1995–2005. *Ocean Dynamics*, 60(3):491–502.

Foley, A.
2010. Uncertainty in regional climate modelling: a review. *Progress in Physical Geography*, 34(5):647–670.

Giorgi, F. and X. Bi
2000. A study of internal variability of a regional climate model. *Journal of Geophysical Research*, 105(D24):29 503–29 521.

Hanke, M., R. Redler, T. Holfeld, and M. Yastremsky
2016. YAC 1.2.0: new aspects for coupling software in Earth system modelling. *Geoscientific Model Development*, 9:2755–2769.

Holton, J.
2004. *An introduction to dynamic meteorology.* Elsevier.

Kållberg, P.
1990. HIRLAM Forecast Model Level 1 Documentation Manual. Technical report, Sveriges meteorologiska och hydrologiska institut (SMHI). Norrköping, Sweden.

Kalnay, E., M. Kanamitsu, R. Kistler, W. Collins, D. Deaven, L. Gandin, M. Iredell, S. Saha, G. White, J. Woollen, Y. Zhu, M. Chelliah, E. W., W. Higgins, J. Janowiak, K. Mo, C. Ropelewski, J. Wang, A. Leetmaa, R. Reynolds, R. Jenne, and D. Joseph
1996. The NCEP/NCAR 40-year reanalysis project. *Bulletin of the American Meteorological Society*, 77:437–471.

Karcher, M., R. Gerdes, F. Kauker, and C. Köberle
2003. Arctic warming: evolution and spreading of the 1990s warm event in the Nordic seas and the Arctic Ocean. *Journal of Geophysical Research*, 108(C2):3034.

Kauker, F., R. Gerdes, M. Karcher, C. Köberle, and J. Lieser
2003. Variability of Arctic and North Atlantic sea ice: a combined analysis of model results and observations from 1978 to 2001. *Journal of Geophysical Research*, 108(C6):3182.

Knopf, B.
2006. *On intrinsic uncertainties in earth system modelling.* PhD thesis, Universität Potsdam.

Lucas-Picher, P., D. Caya, R. de Elía, and R. Laprise
2008. Investigation of regional climate models' internal variability with a ten member ensemble of 10-year simulations over a large domain. *Climate Dynamics*, 31:927–940.

Mikolajewicz, U., D. Sein, D. Jacob, T. Königk, R. Podzun, and T. Semmler
2005. Simulating Arctic sea ice variability with a coupled regional atmosphere–ocean–sea ice model. *Meteorologische Zeitschrift*, 14(6):793–800.

Nikiéma, O. and R. Laprise
2013. An approximate energy cycle for inter-member variability in ensemble simulations of a regional climate model. *Climate Dynamics*, 41:831–852.

O'Brien, T., L. Sloan, and M. Snyder
2011. Can ensembles of regional climate model simulations improve results from sensitivity studies? *Climate Dynamics*, 37:1111–1118.

Pacanowski, R.

1996. MOM 2 documentation, user's guide and reference manual. Technical report, Geophysical Fluid Dynamics Laboratory.

Rapaić, M., M. Leduc, and R. Laprise

2010. Evaluation of the internal variability and estimation of the downscaling ability of the Canadian regional climate model for different domain sizes over the north Atlantic region using the big-brother experimental approach. *Climate Dynamics*, 36(9–10):1979–2001.

Rinke, A. and K. Dethloff

2000. On the sensitivity of a regional Arctic climate model to initial and boundary conditions. *Climate Research*, 14:101–113.

Rinke, A., P. Marbaix, and K. Dethloff

2004. Internal variability in Arctic regional climate simulations: case study for the SHEBA year. *Climate Research*, 27:197–209.

Roeckner, E., L. Dümenil, E. Kirk, F. Lunkeit, M. Ponater, B. Rockel, R. Sausen, and U. Schlese

1989. The Hamburg version of the ECMWF model (ECHAM). In *Research Activities in Atmospheric and Oceanic Modelling*, G. Boer, ed., Pp. 1–31. CAS/JSC Working Group on Numerical Experimentation, Report No. 13, WMO/TD-No. 332, 7.1–7.4.

Rummukainen, M.

2010. State-of-the-art with regional climate models. *WIREs Climate Change*, 1:82–96.

Serreze, M. and R. Barry

2005. *The Arctic climate system*. Cambridge University Press. New York.

Sommerfeld, A.

2015. *Quantification of internal variability of the Arctic summer atmosphere based on* HIRHAM*5 ensemble simulations*. PhD thesis, Universität Potsdam.

IPCC

2013. *Climate change 2013: the physical science basis. Contribution of Working Group I to the Fifth Assessment Report of the Intergovernmental Panel on Climate Change*. Cambridge / New York: Cambridge University Press.

Wang, J., J. Zhang, E. Watanabe, M. Ikeda, K. Mizobata, J. Walsh, X. Bai, and B. Wu
2009. Is the Dipole Anomaly a major driver to record lows in Arctic summer sea ice extent? *Geophysical Research Letters*, 36(5):L05706.

Woodgate, R.
2013. Arctic ocean circulation: going around at the top of the world. *Nature Education Knowledge*, 4(8):8.

Hiermit versichere ich, die vorliegende Arbeit selbstständig und nur unter Verwendung der angegebenen Quellen und Hilfsmittel verfasst zu haben. Diese Arbeit wurde in gleicher oder ähnlicher Form bisher keiner anderen Prüfungsbehörde vorgelegt und auch nicht veröffentlicht.

Potsdam, den 16.10.2018 Julius Eberhard